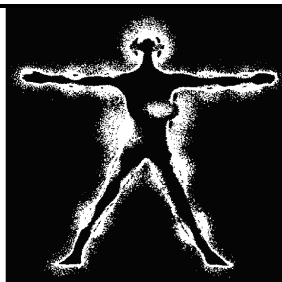


БИОМЕДИЦИНСКАЯ РАДИОЭЛЕКТРОНИКА



7' 2018

Выходит с 1998 г.

Включен в перечень ВАК

Главный редактор: академик РАН Ю.В. ГУЛЯЕВ

Редакционная коллегия: д.ф.-м.н., проф. **О.В. Бецкий** (зам. главного редактора), д.т.н., проф. А.Г. Гудков, к.т.н. С.Г. Гуржин, д.т.н., д.ф.-м.н. М. Жадобов (Франция), д.т.н. проф. В.И. Жулев, д.т.н., проф. К.В. Зайченко, д.м.н., проф. В.Ф. Киричук, к.ф.-м.н. В.В. Колесов, к.б.н. Т.И. Котровская, д.т.н. А.П. Креницкий, д.м.н. А.Ю. Лебедева, д.б.н., проф. Н.Н. Лебедева, д.х.н., проф. А.К. Лященко, д.ф.-м.н., проф. В.Н. Макаров, д.б.н. И.В. Матвейчук, д.т.н., проф. Ю.П. Муха, д.ф.-м.н., проф. Ю.В. Обухов, д.ф.-м.н., проф. Ю.А. Пирогов, д.ф.-м.н., проф. Н.И. Синицын, д.т.н., проф. Л.Т. Сушкова, к.т.н., проф. В.Д. Тупикин, д.т.н. И. Тауфер (Чешская республика), д.ф.-м.н., проф. В.А. Черепенин, к.ф.-м.н. Ю.П. Чукова, д.ф.-м.н., проф. А.Г. Шейн, д.т.н., проф. **С.И. Щукин** (зам. главного редактора), д.т.н., проф. З.М. Юлдашев

Editor-in-Chief Academician RAS Yu.V. GULYAEV

Editorial Board: **Dr.Sc. (Phys.-Math.), Prof. O.V. Betskii (Deputy Editor)**, Dr.Sc. (Phys.-Math.), Prof. V.A. Cherepenin, Dr.Sc. (Eng.), Prof. A.G. Gudkov, Dr.Sc. (Med.), Prof. V.F. Kirichuk, Dr.Sc. (Med.) A.Yu. Lebedeva, Dr.Sc. (Biol.), Prof. N.N. Lebedeva, Dr.Sc. (Chem.), Prof. A.K. Lyashchenko, Dr.Sc. (Phys.-Math.), Prof. V.N. Makarov, Dr.Sc. (Biol.) I.V. Matveichuk, Dr.Sc. (Eng.), Prof. Yu.P. Mukha, Dr.Sc. (Phys.-Math.), Prof. Yu.V. Obukhov, Dr.Sc. (Phys.-Math.), Prof. Yu.A. Pirogov, **Dr.Sc. (Eng.), Prof. S.I. Shchukin (Deputy Editor)**, Dr.Sc. (Phys.-Math.), Prof. A.G. Shein, Dr.Sc. (Phys.-Math.), Prof. N.I. Sinitsyn, Dr.Sc. (Eng.), Prof. L.T. Sushkova, Dr.Sc. (Eng.), Prof. I. Taufer (Czech Republic), Dr.Sc. (Eng.), Prof. Z.M. Yuldashev, Dr.Sc. (Eng.), Prof. K.V. Zaichenko, Dr.Sc. (Phys.-Math.) M. Zhadobov (France), Dr.Sc. (Eng.), Prof. V.I. Zhulev, Ph.D. (Phys.-Math.) Yu.P. Chukova, Ph.D. (Eng.) S.G. Gurzhin, Ph.D. (Phys.-Math.) V.V. Kolesov, Ph.D. (Biol.) T.I. Kotrovskaya, D.Sc. (Eng.) A.P. Krenitskii, Ph.D. (Eng.), Prof. V.D. Tupikin

Editors of issue:

Prof. Sergey I. Shchukin
*Baumann Moscow State Technical University,
Russia*

Prof. Sergey Selishchev
*National Research University of Electronic Technology,
Moscow, Russia*

Редакторы выпуска:

д.т.н., профессор С.И. Щукин
*Московский государственный технический
университет им. Н.Э. Баумана*

д.т.н., профессор С.В. Селищев
*Национальный исследовательский университет
«Московский институт электронной техники»*

Proceedings of the 13th Russian German Conference on Biomedical Engineering 23.05.2018–25.05.2018, Aachen, Germany

Conference Chairs

Chair: Prof. Dr.-Ing. Dr. med. Steffen Leonhardt, Philips Chair for Medical Information Technology (MedIT), RWTH Aachen University, Germany

Co-Chair: Prof. Jaakko Malmivuo, PhD, Chair of Electronics and Medical Signal Processing (EMSP), Technische Universität Berlin, Germany

Scientific Committee

Prof. Hubertus Feußner, Technical University of Munich, Germany; Prof. Birgit Glasmacher, Leibniz Universität Hannover, Germany; Prof. Thomas Gries, RWTH Aachen University, Germany; Prof. Tobias Ortmaier, Leibniz Universität Hannover, Germany; Prof. Sergey Selishchev, National Research University of Electronic Technology, Moscow, Russia; Prof. Sergey I. Shchukin, Baumann Moscow State Technical University, Russia; Prof. Ludmila T. Sushkova, Vladimir State University, Russia; Prof. Zafar Yuldashev, Saint-Petersburg State Electrotechnical University LETI, Russia

The Russian Bavarian Conference on Biomedical Engineering (RBC) was founded 2005 in Munich. Thereafter, the conference established itself as a fruitful information exchange platform for researchers from Russia and Germany. The conference location alternated equally between cities in Russia and the southern part of Germany. After the successful 8th RBC conference in Moscow the steering committee decided to broaden the focus and establish a new conference: the Russian German Conference (RGC) on Biomedical Engineering. The goal is to serve as meeting point for information exchange and as venue for initiating bilateral Russian German research projects within the conference's scope. The first RGC on Biomedical Engineering took place in 2013 Hanover, Germany.

Previous conferences:

2016: 12th Russian-German Conference on Biomedical Engineering, 04–07.07.2016, Vladimir State University, Suzdal, Russia – Link to Proceedings

2015: 11th German-Russian Conference on Biomedical Engineering, 17–19.06.2015, RWTH Aachen University, Germany

2014: 10th German-Russian Conference on Biomedical Engineering, 25–27.06.2014, Saint Petersburg State Electrotechnical University «LETI», St. Petersburg, Russia

2013: 9th Russian-German Conference, 23–26.10.2013, Hanover, Germany

2010: 6th Russian-Bavarian Conference on Biomedical Engineering, 8–12.11.2010, Bauman Moscow State Technical University, Russia

2009: 5th Russian-Bavarian Conference on Biomedical Engineering, 01–04.07.2009, Munich, Germany

2008: 4th Russian Bavarian Conference on Biomedical Engineering, Moscow Institute of Electronic Technology, 07–11.07.2008 – Link to Proceedings

2007: 3rd Russian-Bavarian Conference on Biomedical Engineering, 02–03.07.2007, Friedrich-Alexander-University Erlangen-Nuremberg, Germany

2006: 2nd Russian-Bavarian Conference on Bio-Medical Engineering, 14–15.06.2006, Bauman Moscow State Technical University, Russia

2005: 1st Russian-Bavarian Conference on Bio-Medical Engineering, 13–14.10.2005, Munich, Germany

13-я Российско-Германская конференция по биомедицинской инженерии 23.05.2018-25.05.2018, Аахен, Германия

Организационный комитет

Руководство конференции:

Руководитель: проф. д.т.н, д.м.н., Steffen Leonhardt (С.К. Леонхард), зав. кафедрой информационных технологий в медицине, Рейнско-Вестфальский технический университет Ахена, Германия.

Заместитель: проф., к.т.н., Jaakko Malmivuo (Гакко Малмиво), Берлинский технический университет, кафедра электроники и обработки медицинских сигналов, Германия.

Научный комитет:

Проф. Hubertus Feußner, Мюнхенский технический университет, Германия

Проф. Brigit Glasmacher (Бригит Гласмахер), Ганноверский университет имени Лейбница, Германия

Проф., Thomas Gries (Томас Гриз), Рейнско-Вестфальский технический университет Ахена, Германия

Проф. Tobias Ortmaier (Тобиас Артмаер), Ганноверский университет имени Лейбница, Германия

Проф. Селищев С.В., Национальный исследовательский университет Московский институт электронной техники, Россия

Проф. Щукин С.И., Московский государственный технический университет им. Баумана, Россия

Проф. Сушкова Л.Т., Владимирский государственный университет, России

Проф. Юлдашев З.М., Санкт-Петербургский государственный электротехнический университет ЛЭТИ, Россия

Российско-Баварская конференция по биомедицинской инженерии (РБК) была впервые проведена в 2005 г. в г. Мюнхене. С этого момента, конференция представляет собой продуктивную платформу для обмена информации учеными из России и Германии. Место проведения конференции чередовалось между городами России и южной части Германии. После успешной 8-й конференции РБК в Москве, руководящий комитет решил расширить информационное поле и организовать новую конференцию – Российско-Германскую конференцию. Основной задачей является организация встречи для обмена информацией, а также для инициирования российско-германских исследовательских проектов в рамках проводимой конференции. Первая Российско-Германская конференция впервые была проведена в 2013 г. в Германии в г. Ганновере.

Предыдущие конференции:

2016: 12-я Российско-Германская конференция по биомедицинской инженерии, 04.07. – 07.2016, Владимирский государственный университет, Суздаль, Россия

2015: 11-я Российско-Германская конференция по биомедицинской инженерии, 17.06 – 19.06.2015, Рейнско-Вестфальский технический университет Ахена, Германия

2014: 10-я Российско-Германская конференция по биомедицинской инженерии, Санкт-Петербургский государственный электротехнический университет ЛЭТИ, Санкт-Петербург, Россия

2013: 9-я Российско-Германская конференция, 23.10 – 26.10.2013, Ганновер, Германия

2010: 6-я Российско-Баварская конференция по биомедицинской инженерии, 08.11 – 12.11.2010, Московский государственный технический университет им. Н.Э. Баумана, Москва, Россия

2009: 5-я Российско-Баварская конференция по биомедицинской инженерии, 01.04 – 04.07.2009, Мюнхен, Германия

2008: 4-я Российско-Баварская конференция по биомедицинской инженерии, 07.07 – 11.07.2008, Московский институт электронной техники, Россия

2007: 3-я Российско-Баварская конференция по биомедицинской инженерии, 02.07 – 03.07.2007, Нюрнбергер, Германия

2006: 2-я Российско-Баварская конференция по биомедицинской инженерии, 14.06 – 15.06.2006, Московский государственный технический университет им. Н. Э. Баумана, Москва, Россия

2005: 1-я Российско-Баварская конференция по биомедицинской инженерии, 13.10 – 14.10.2005, Мюнхен, Германия

Contents

Содержание

3

Tissue layers three-dimensional structure formation by nanosecond laser pulses

Pavel N. Vasilevsky, Alexander Yu. Gerasimenko, Mikhail S. Savelev and Sergey A. Tereshchenko 1(115)

Формирование трёхмерной структуры слоёв ткани с помощью наносекундных лазерных импульсов

Василевский П.Н.¹, Герасименко А.Ю.^{1,2}, Савельев М.С.^{1,2}, Терещенко С.А.¹

¹ Национальный исследовательский университет «Московский институт электронной техники» (НИУ «МИЭТ»), Зеленоград, Россия,

² Первый Московский государственный медицинский университет имени И. М. Сеченова.

Получены трехмерные тканеинженерные конструкции на основе белков альбумина и коллагена с внутренним каркасом из углеродных нанотрубок. Определены нелинейные свойства белковых водных дисперсий с углеродными нанотрубками. Увеличение значений нелинейного коэффициента поглощения с добавлением углеродных нанотрубок позволяет предположить, что нанотрубки поглощают большую часть лазерного излучения по мере увеличения его светового потока.

Ключевые слова: нелинейная оптика, углеродные нанотрубки, применение лазера, мощность лазера, поглощение.

Biotechnical system for automatic assessment of facial nerve dysfunction rate

E.A. Lavrova, A.V. Samorodov, A.V. Mordovsky, K.G. Kudrin, A.P. Polyakov 4(118)

Биотехническая система автоматической оценки степени повреждения лицевого нерва

Лаврова Е.А.¹, Самородов А.В.¹, Мордовский А.В.², Кудрин К.Г.², Поляков П.А.²

¹ МГТУ имени Н.Э. Баумана, Москва, Россия

² МНИОИ им. П.А. Герцена

Представлены результаты исследования метода автоматической оценки степени повреждения лицевого нерва, основанного на компьютерном анализе видеоизображения лица. Разработан метод регистрации видеоизображения лица. Приведены индексы асимметрии лица, полученные в результате обработки видеоизображения лица, результаты сравнения индексов асимметрии пациентов и представителей контрольной группы. Определены наиболее информативные индексы асимметрии лица.

Ключевые слова: автоматический анализ изображения лица, контрольные точки лица, повреждение лицевого нерва, асимметрия лица.

Variation in Local Pulse Wave Velocity over the Cardiac Cycle: In-Vivo Validation using Dual-MPG Arterial Compliance Probe

Nabeel P.M., Jayaraj Joseph and Mohanasankar Sivaprakasam 7(121)

Вариация локальной скорости пульсовой волны, определяемой в течение сердечного цикла: валидация *in-vivo* с использованием двухэлементного магнитного плетизмографического артериального зонда

Набель П.М., Джайарай Дж., Моханасанкар С.

Индийский технологический институт Мадраса

Представлен метод и система прямого измерения локальных изменений скорости пульсовой волны, определяемой в течение сердечного цикла. Разработан новый двухэлементный магнитный плетизмографический артериальный зонд. Исследования на 15 здоровых добровольцах показали возможность оценки локальной скорости пульсовой волны. Предлагаемый зонд не требует калибровки и обеспечивает возможность безманжетной оценки параметров артериального давления от поверхностных артерий в каждом кардиоцикле.

Ключевые слова: магнитный плетизмографический зонд, неинвазивные измерения, вариация локальной скорости пульсовой волны, безманжетная оценка параметров артериального давления.

Hemodynamic Interventions for Inducing Blood Pressure Variation in Laboratory Settings

Nabeel P.M., Surya Venkatramanan, Jayaraj Joseph, Mohanasankar Sivaprakasam 11(125)

Гемодинамические пробы для индуцирования изменений артериального давления в лабораторных условиях

Набель П.М., Сурия В., Джайарай Дж., Моханасанкар С.

Индийский технологический институт Мадраса

Рассмотрены пять упражнений, влияющих на гемодинамику и приводящих к безопасному контролируемому изменению артериального давления. Получены данные изменения артериального давления во время каждого упражнения и после его окончания. Результаты могут быть использованы для сбора данных для развития моделей предсказания артериального давления в системах безманжетного мониторинга.

Ключевые слова: гемодинамические пробы, контролируемое изменение артериального давления, время восстановления.

Non-Invasive Assessment of Arterial Incremental Elastic Modulus Variations within a Cardiac Cycle

Raj V., Nabeel P.M., Jayaraj Joseph and Mohanasankar Sivaprakasam 15(129)

Неинвазивная оценка вариаций инкрементного модуля упругости артерии, определяемого в течение сердечного цикла

Рай К., Набель П.М., Джайарай Дж., Моханасанкар С.

Индийский технологический институт Мадраса

Предложен зонд для неинвазивного измерения инкрементного модуля упругости артерии, содержащий один ультразвуковой преобразователь и тонометр для одновременного определения толщины стенки артерии, ее диаметра и пульсовых волн. Экспериментальные исследования на 10 добровольцах показали достоверность выполняемых измерений.

Ключевые слова: инкрементный модуль упругости артерии, ультразвуковой преобразователь, тонометрия, зонд для неинвазивных измерений.

The patterning of biostructures with carbon nanoframe in protein matrix

Natalia Zhurbina, Alexander Gerasimenko, Olga Glukhova, Michail Slepchenkov, Michail Savelyev,

Levan Ichkitidze, Vitalii Podgaetskii, Sergey Selishchev, Evgeniy Kitsyuk and Alexander Pavlov 19(133)

Структурирование биоконструкций с углеродным нанокаркасом в белковой матрице

Герасименко А.Ю.^{1,2}, Глухова О.Е.³, Слпченков М.М.³, Журбина Н.Н.¹, Савельев М.С.^{1,2},

Ичкитидзе Л.П.^{1,2}, Подгаецкий В.М.¹, Селищев С.В.¹, Кицюк Е.П.⁴, Павлов А.А.⁵

¹ Национальный исследовательский университет «Московский институт электронной техники» (НИУ «МИЭТ»), Зеленоград, Россия

² Первый Московский государственный медицинский университет имени И.М. Сеченова

³ Саратовский государственный университет

⁴ Научно-производственный комплекс «Технологический центр»

⁵ Институт нанотехнологий микроэлектроники РАН

Приведены результаты экспериментов по структурированию биоконструкций с углеродным нанокаркасом в белковой матрице. Выявлен механизм связывания одностенных углеродных нанотрубок под действием лазерного излучения. Представлены синтезированные образцы каркасного наноматериала на основе разветвленной структуры углеродных нанотрубок. Экспериментально исследовано и продемонстрировано лазерное формирование древовидной структуры нанокаркаса из углеродных нанотрубок в белковой матрице.

Ключевые слова: структурирование, биоструктуры, биоматериалы, углеродные нанотрубки, белковая матрица, импульсное лазерное излучение.

Mixed Reality applications for the collaborative operating room – a prototypical study

Nils Marahrens, Daniel Ostler, Juliane Weinzierl, Nils Kohn, Thomas Vogel, Dirk Wilhelm,

Sebastian Koller and Hubertus Feußner 22(136)

Приложения смешанной реальности для коллаборативного операционного блока – прототипное исследование

Mararens H., Ostler D., Weinzirl Дж., Кон Н., Фогель Т., Вильгельм Д., Коллер С., Фесснер Х.

Мюнхенский технический университет

Приведено исследование потенциала применения приложений смешанной реальности для эффективного взаимодействия в коллаборативном операционном блоке. Представлено описание примера использования устройства, помогающего операционной сестре в корректном выборе хирургического инструмента, пользовательская оценка алгоритма взаимодействия с устройством смешанной реальности.

Ключевые слова: смешанная реальность, дополненная реальность, коллаборативный операционный блок, хирургические вспомогательные технологии, распознавание объектов.

Longterm high resolution manometry (HRM) challenges and pitfalls of an automated motility analysis

Alissa Jell, Norbert Hüser, Suyu He, Dmitry Telyshev, Sergey Selishev and Hubertus Feußner 25(139)

Длительная манометрия высокого разрешения: сложности и недостатки автоматизированного анализа моторики пищевода

Елл А.¹, Хюссер Н.¹, Хе С.¹, Остлер Д.¹, Тельшев Д.², Селишев С.², Фесснер Х.¹

¹ Мюнхенский технический университет, Германия

² Национальный исследовательский университет «Московский институт электронной техники» (НИУ «МИЭТ»), Зеленоград, Россия

Обоснована актуальность пролонгации эзофагиальной манометрии высокого разрешения (ЭМВР) для учета изменения циркадных ритмов в работе пищевода. Проведены клинические исследования моторики пищевода с помощью длительной ЭМВР. Разработана программа автоматического анализа, основанная на чикагской классификации. В результате были установлены значения нормы и патологии для выявления нарушений работы пищевода при проведении длительной ЭМВР.

Ключевые слова: эзофагоманометрия, манометрия высокого разрешения, пищевод.

Investigation of the spectral properties of media based on chitosan and carbon nanotubes

Yulia O. Fedorova, Alexander A. Polokhin, Denis T. Murashko, Mikhail S. Saveliev,

Natalia O. Agafonova and Alexander Yu. Gerasimenko 29(143)

Исследование спектральных свойств сред на основе хитозана и карбоновых нанотрубок

Федорова Ю.О.¹, Полохин А.А.¹, Мурашко Д.Т.¹, Савельев М.С.¹, Герасименко А.Ю.^{1,2}

¹ Национальный исследовательский университет «Московский институт электронной техники» (НИУ «МИЭТ»), Зеленоград, Россия

² ПМГМУ им. И.М. Сеченова

Представлены результаты исследований спектральных характеристик материалов на основе хитозана с включениями карбоновых нанотрубок, применяемых в кардиоваскулярной хирургии для создания имплантируемых тканей.

Ключевые слова: хитозан, нанотрубки, спектральные характеристики, кардиохирургия, тканевая инженерия.

Piezoelectric properties of PVDF and PVDF-TrFE electrospun materials for nerve regeneration

Fedaa Al Halabi, Oleksandr Gryshkov, Antonia Kuhn, Viktoria Kapralova and Birgit Glasmacher 32(146)

Пьезоэлектрические свойства материалов PVDF и PVDF-TrFE, изготавливаемых электропрядением, для восстановления нервов

Халаби Ф. Аль¹, Гришков О.¹, Кун А.И.¹, Капралова В.М.², Гласмахер Б.¹

¹ Ганноверский университет имени Лейбница, Германия

² Санкт-Петербургский политехнический университет Петра Великого, Российская Федерация

Поливинилидинфторид и трифторэтилен являются перспективными материалами для разработки активных имплантатов для регенерации нервов. Разработан метод измерения параметров материалов для описания их электромеханической связи. Метод заключается в создании механического напряжения волокнистых образцов с последующим измерением индуцированных электрических зарядов.

Ключевые слова: пьезоэффект, восстановление нервов, электромеханическая связь.

Evaluation of the P300 parameters with photic stimulation

Alexander Dmitriev and Sergey Shchukin 36(150)

Оценка параметров P300 при фотостимуляции

Дмитриев А.Н., Щукин С.И.

МГТУ имени Н.Э. Баумана, Москва, Россия

Показано влияние фотостимуляции с частотами 1, 3 и 5 Гц и пространственным интервалом между светодиодами 0.8°, 1.6 и 2.4 на детекцию P300. Продемонстрировано изменение амплитуды и латентности P300 для разных режимов стимуляции. Оценено влияние зрительных вызванных потенциалов на детекцию P300.

Ключевые слова: P300, ИМК, фотостимуляция, ЗВП, пространственный интервал.

Telephone call management in the cognitive operating room

Nils Kohn, Daniel Ostler, Sebastian Koller, Nils Marahrens, Nicole Samm, Michael Kranzfelder,

Thomas Vogel, Dirk Wilhelm and Hubertus Feußner 40(154)

Управление телефонными звонками в когнитивной операционной комнате

Кон Н., Остлер Д., Коллер С., Мараренс Н., Замм Н., Кранцфельдер М., Фогель Т., Вильгельм Д., Фесснер Х.

Мюнхенский Технический Университет

Мобильные телефоны повышают доступность хирургов и регулярно берутся в операционную. Но это увеличивает рабочую нагрузку и может привести к негативному влиянию на результат операции. Предложена система ситуационной осведомленности, основанная на классификации звонков по важности, приведены варианты сценариев реагирования. Результат опроса явно показывает преимущество системы управления звонками.

Ключевые слова: когнитивная операционная комната, управление звонками, классификация важности звонков.

Translation Dynamics in Holistic Analysis of Functional Human-body System

Jochen Mau 43(157)

Трансляционная динамика в комплексном анализе работы организма человека

Mau J.^{1,2}

¹ Дюссельдорфский Университет им. Г.Гейне, Дюссельдорф, Германия

² Частный институт вычислительных методов, Крефельд, Германия

Предложена математическая модель аксиоматической конфигурации динамики, основанная на системном подходе, которая может объяснить динамику работы человеческого организма совместно на различных уровнях. Данный метод позволяет упростить вычислительный процесс, в его основе лежит принцип получения математических выражений высоких уровней из математических выражений более низких уровней.

Ключевые слова: математическое моделирование, системный подход, динамика.

Ready for the Future: 5G Data Transfer in Visceral Surgery

Thomas Vogel, Hubertus Feßner, Daniel Ostler, Sebastian Koller, Nils Marahrens, Michael Kranzfelder,

Walter Weigel and Joseph Eichinger 47(161)

Возможности «Хирургии 4.0»: передача данных 5G при минимально-инвазивной хирургии

Фогель Т.^{1,2}, *Мараренс Н.*¹, *Коллер С.*¹, *Йелл А.*^{1,2}, *Остлер Д.*¹, *Вайгель В.*³,

*Айшингер Дж.*³, *Фесснер Х.*^{1,2}, *Кранцфельдер М.*^{1,2}

¹ Ганноверский университет имени Лейбница, Германия

² Санкт-Петербургский политехнический университет Петра Великого, Санкт-Петербург, Российская Федерация

³ Научный центр Мюнхена Huawei, Германия

Технологии передачи данных в операционной ограничены с точки зрения скорости передачи, латентности и стабильности сигнала. Проведено исследование по методу «Дельфи», в котором дана оценка ожидания и принятия технологии 5G в хирургическом поле в целом. Предварительные результаты исследования по методу «Дельфи» показывают положительную перспективу реализации технологии 5G в клинической среде.

Ключевые слова: минимально-инвазивная хирургия, передача данных, 5G.

IVAP 2025 – Towards the collaborative operating room

Daniel Ostler, Nils Marahrens, Nils Kohn, Sebastian Koller, Michael Kranzfelder, Hubertus Feußner and Dirk Wilhelm 51(165)

IVAP 2025 – По направлению к коллаборативной операционной комнате

Остлер Д., Мараренс Н., Кон Н., Коллер С., Кранцфельдер М., Фесснер Х., Вильгельм Д.

Мюнхенский Технический Университет

Представлены первые результаты построения коллаборативной операционной комнаты, которая активно поддерживает контекстно-зависимое интра- и послеоперационное лечение. Функционирование когнитивной хирургической среды демонстрируется на типичном примере лапароскопической резекции желчного пузыря. Приведено описание концепции коллаборативной операционной комнаты и ее основные компоненты; их реализация показала эффективность предложенного подхода.

Ключевые слова: коллаборативная комната, анализ данных, резекция, желчный пузырь.

Creation of 3D nanocomposite bioconstructions using a layer-by-layer laser prototyping device

Ulyana Kurilova, Natalya Zhurbina, Dmitry Ignatov, Dmitry Ryabkin, Alexander Polokhin,

Evgeniy Pyankov and Alexander Gerasimenko 54(168)

Создание трехмерных нанокompозитных биоконструкций

с использованием послыонного лазерного устройства прототипирования

*Курилова У.Е.*¹, *Журбина Н.Н.*¹, *Игнатов Д.А.*¹, *Рябкин Д.А.*¹, *Полохин А.А.*¹, *Пьянков Е.С.*¹, *Герасименко А.Ю.*^{1,2}

¹ Национальный исследовательский университет «Московский институт электронной техники» (НИУ «МИЭТ»), Зеленоград, Россия

² ПМГМУ им. И.М. Сеченова

Представлен метод получения нанокompозитных биоконструкций из водно-белковой дисперсии углеродных нанотрубок. Приведены результаты исследований структурных и биологических свойств нанокompозитных биологических структур для тканевой инженерии, созданных методом лазерного трехмерного прототипирования. Показано, что разработанный метод может быть применен для восстановления остеохондральных дефектов в суставах.

Ключевые слова: нанокompозиты, трехмерное лазерное прототипирование, тканевая инженерия.

Analysis of physiological data to quantify stress and workload of surgeons with different levels of training during a laparoscopic cholecystectomy

Nicole Samm, Daniel Ostler, Thomas Vogel, Nils Marahrens, Dirk Wilhelm, Hubertus Feussner and Ralf Stauder 58(172)

Анализ физиологических показателей для количественной оценки стресса и нагрузки хирургов с различным уровнем подготовки во время лапароскопической холецистэктомии

Самм Н., Остлер Д., Фогель Т., Мараренс Н., Вильгельм Д., Фесснер Х., Штаудер Р.

Мюнхенский Технический Университет

Повышенный уровень стресса и рабочие нагрузки хирургов во время операций являются серьезной угрозой безопасности пациентов. Показано, что параметры сердечного и дыхательного ритма являются маркерами физического и умственного стресса, который, в свою очередь, будет пропорционален уровню образования и опыту хирурга. Результаты такого анализа могут быть интегрированы в систему распознавания рабочих процессов, в том числе для роботизированных операций.

Ключевые слова: робот-ассистивные технологии, показатели уровня стресса, лапароскопическая хирургия, сердечный и дыхательный ритм, машинное обучение.

New Geometric Method of Heart Rate Variability Estimation based on the Multiscale Correlation Analysis Representation

Viacheslav Antsiperov 61(175)

Новый, основанный на представлениях многомасштабного корреляционного анализа, метод оценивания вариабельности сердечного ритма

Анциперов В.Е.

Институт радиотехники и электроники им. В.А. Котельникова Российской академии наук (ИРЭ РАН)

Представлены последние результаты работы автора в области разработки эффективных алгоритмов оценивания параметров вариабельности сердечного ритма. Показано, что в рамках методологии многомасштабного корреляционного анализа, на основе вычисления по масштабно-временным представлениям ряда геометрических характеристик, можно достаточно надежно оценивать параметры сердечного ритма и осуществлять последующий анализ их динамики. На примере длительных (Холтеровского типа) ЭКГ записей обсуждаются скоростные, робастные и др. характеристики предложенного метода.

Ключевые слова: анализ биомедицинских сигналов, обработка длительных записей ЭКГ, многомасштабный корреляционный анализ, вариабельность сердечного ритма, корреляционная ритмография, геометрические методы анализа ВСР, оценивание параметров медленных волн ВСР.

Tactile information analysis for forearm prosthesis feedback implementation

Vladislav Bukin and Andrey Briko 66(180)

Анализ тактильной информации для реализации обратной связи в протезах предплечья

Букин В.Ю., Брико А.Н.

МГТУ имени Н.Э. Баумана, Москва, Россия

Рассмотрены аспекты решения проблемы восполнения обратной связи в биоэлектрических протезах предплечья. Описана связь между кинематической и математической моделями протеза предплечья для расчета параметров для реализации обратной связи. Для получения входных данных модели, произведена серия экспериментов по раздавливанию хрупких объектов протезом.

Ключевые слова: обратная связь, биоэлектрический протез предплечья, тактильная информация.

Intraoperative Sterile Molding of Patient Specific Templates for Minimally Invasive Cochlear Implant Surgery

Samuel Müller, Clarence Janka, Lüder Alexander Kahrs and Tobias Ortmaier 70(184)

Интраоперационное стерильное формование индивидуальных слепков пациента для минимально инвазивной кохлеарной имплантации

Мюллер С., Янка С., Карс Л.А., Ортмэйер Т.

Ганноверский университет имени Лейбница

Использование минимально инвазивных технологий при кохлеарной имплантации сдерживается повышением требований к точности сверления улитки внутреннего уха. Одним из способов достижения требуемой точности является использование индивидуального слепка улитки пациента внутреннего уха в качестве проводника для сверла. Показана возможность применения для этого гранулированных термопластов низкого давления.

Ключевые слова: гранулированные термопласты низкого давления, минимально инвазивная хирургия, кохлеарная имплантация.

- Development of Software System for Restoration of Mimic Activity of Patients with Aphasia**
Anastasia Polishchuk and Irina Apollonova 1
- Программный комплекс для восстановления мимической активности при афазии**
Полищук А.А., Аполлонова И.А.
 МГТУ имени Н.Э. Баумана, Москва, Россия
 Программный комплекс предназначен для восстановления речи и мимической активности у пациентов, перенесших заболевания, способствующие развитию афазии. Представлены требования к максимальной допустимой погрешности при автоматической расстановке контрольных точек, оценке правильности и работоспособности выбранной методики лечения.
Ключевые слова: инсульт, реабилитация, контрольные точки, афазия.
-
- Development of algorithm for HR determination for athletes**
Irina A. Kussyakina 4
- Алгоритм определения ЧСС для спортсменов**
Кузякина И.А.
 МГТУ имени Н.Э. Баумана, Москва, Россия
 Представленный алгоритм определения ЧСС предназначен для определения основного параметра оценки функциональной подготовленности спортсменов в режиме реального времени в условиях спортивной арены. Оценка параметра происходит методом электроимпедансной реографии. Эффективность и точность алгоритма подтверждается на реальных сигналах.
Ключевые слова: функциональная подготовленность, реография, ЧСС, алгоритм.
-
- Clinical signs of different types of pigmented skin lesions for early diagnostics for the purpose of early detection of precancerous skin changes**
Elena Rimsкая, Irina Apollonova, Aleksandr Nikolaev, Konstantin Kudrin, Igor Reshetov, Nikita Chernomyrdin and Kirill Zaytsev 6
- Клинические признаки различных типов пигментных новообразований кожи в ранней диагностике с целью выявления предраковых изменений кожи**
Римская Е.Н.¹, Аполлонова И.А.¹, Николаев А.П.¹, Кудрин К.Г.², Черномырдин Н.В.¹, Решетов И.В.², Зайцев К.И.³
¹ МГТУ имени Н.Э. Баумана, Москва, Россия
² НОКЦ пластической хирургии ГБОУ ВПО Первый московский государственный медицинский университет им. И.М. Сеченова
³ ИОФ РАН им. А.М. Прохорова
 Среди всех новообразований кожи особое внимание уделяется меланоме из-за ее крайней агрессивности. Поскольку эффективность лечения меланомы сильно зависит от ее ранней диагностики, разработка новых высокоэффективных методов раннего выявления диспластических невусов и меланомы кожи *in situ* остается крайне актуальной проблемой современной медицины, прикладной физики и инженерных наук. Перспективным путем повышения эффективности ранней неинвазивной диагностики меланомы является использование автоматизированных комплексов, что позволяет определять клинические признаки пигментных новообразований кожи, основываясь на анализе данных клинической диагностики.
Ключевые слова: пигментные новообразований кожи, клинические признаки, меланома, диспластический невус.
-
- Effect of temperature on electrical cell conductivity of human erythrocytes**
Chadapust Sudsiri and Raymond Jame Ritchie 8
- Влияние температуры на электрическую проводимость эритроцитов человека**
Судсири Ч.Дж., Ритчи З.Дж.
 Университет Принца Сонгкла, Тайланд
 Проведено исследование цитоплазматической электрической проводимости эритроцитов человека при разной температуре. Дана экспериментальная оценка объема клетки и содержания клеточной воды в зависимости от температуры, по которым был выполнен расчет цитоплазматической электрической проводимости. Показано, что цитоплазматическая электрическая проводимость эритроцитов может быть оценена независимо от исследования диэлектрических свойств клеток.
Ключевые слова: цитоплазматическая электропроводность, температурная зависимость, эритроциты, объем клетки.
-
- Development of the infrared images processing algorithm for the automatic detection of the early stage of periodontal disease**
Leonid Akulenko and Alexander Kolpakov 12
- Разработка алгоритма автоматического обнаружения ранней стадии воспаления мягких тканей пародонта на инфракрасных изображениях**
Акуленко Л.О., Колпаков А.В.
 МГТУ имени Н.Э. Баумана, Москва, Россия

Представлены результаты исследования эффективности методов сегментации очагов воспаления, а также результаты оценки качества алгоритма автоматического обнаружения очагов воспаления мягких тканей пародонта на инфракрасных изображениях.

Ключевые слова: воспаление пародонта, ранняя стадия, инфракрасные изображения, автоматическое обнаружение.

Algorithm for one-axis receiver of magnetic positioning system

Elena Gerken and Valery Grechikhin 14

Алгоритм определения и ориентации одноосного приемника системы магнитного позиционирования

Геркен Е.А., Гречихин В.В.

Южно-Российский государственный политехнический университет (НПИ) имени М.И. Платова

Системы магнитного позиционирования включают подвижный приемник, осуществляющий измерение ортогональных компонент магнитного поля в исследуемой области. В работе реализован алгоритм определения положения и ориентации одноосного приемника в трехмерном пространстве в реальном времени. Показано, что габаритные размеры приемника могут быть минимизированы без потери точности измерения.

Ключевые слова: системы магнитного позиционирования, одноосный приемник, магнитный поток.

Computational modelling of electroaerosol flows during external therapy

Valeriy Karpukhin, Kristina Mustafina and Georgy Klimiashvili 19

Математическое моделирование потоков электроаэрозолей при лечении ожогов

Карпухин В.А., Мустафина К.С., Климиашвили Г.С.

МГТУ имени Н.Э. Баумана, Москва, Россия

Обоснована актуальность разработки аппарата местной электроаэрозольной терапии ожогов, обеспечивающего направленный поток электроаэрозоля на ожог и позволяющего регулировать его скорость. Исследовано влияние параметров рабочей камеры на поток с целью повышения эффективности терапии. Разработаны геометрическая и математическая модели рабочей камеры. В результате вычислительного эксперимента определены параметры рабочей камеры, при которых достигается максимальный поток.

Ключевые слова: аэрозоль, электроаэрозоль, ожоги, моделирование.

Experimental study of the mechanical properties of materials for physical modelling of biological tissues

Irina Khaydukova, Arina Rezvanova, Nikita Belikov and Gennadiy Savrasov 22

Экспериментальное исследование механических свойств материалов для физического моделирования тканей

Хайдукова И.В., Беликов Н.В., Резванова А.М., Саврасов Г.В.

МГТУ имени Н.Э. Баумана, Москва, Россия

Метод физического моделирования позволяет более точно оценить влияние хирургического лечения на ткани по сравнению с аналитическим и конечным элементным моделированием. Наиболее точное моделирование механических свойств биологической ткани возможно путем выбора наиболее подходящего материала определенной концентрации. Исследована зависимость модуля Юнга от концентрации для желатина и силикона. Данные для всех концентраций были аппроксимированы. Результаты позволяют более точно выбирать необходимую концентрацию для моделирования конкретной ткани.

Ключевые слова: физическая модель, механические свойства, фантом, одноосное растяжение, силикон, желатин.

An approach for patient-specific hemodynamics modeling taking into account biomechanical properties of the cerebral artery

Sergey Frolov, Sergey Sindeev, Anton Potlov and Dieter Liepsch 26

Подход к индивидуальному моделированию гемодинамики у пациента с учетом биомеханических свойств церебральной артерии

Фролов С.В.¹, Синдеев С.В.¹, Потлов А.Ю.¹, Липпи Д.²

¹ Тамбовский государственный технический университет

² Университет прикладных наук Мюнхена

Представлен новый подход к пациент-зависимому математическому моделированию гемодинамики с учетом индивидуальных биомеханических свойств стенки церебральной артерии, получаемых *in vivo* с использованием оптической когерентной эластографии. Развитие подхода позволит использовать его для повышения качества исследования аневризм церебральной артерии.

Ключевые слова: индивидуальное моделирование гемодинамики, церебральная артерия, эластография.

Neural network approach to cell segmentation in immunocytochemical study

Dmitry Parpulov, Andrey Samorodov and Vladimir Iglovikov 30

Нейросетевой подход к сегментации клеток на изображениях иммуноцитохимических препаратов

Парпулов Д.А.¹, Самородов А.В.¹, Игловиков В.И.²

¹ МГТУ имени Н.Э. Баумана, Москва, Россия

² Lyft Inc., San Francisco, CA 94107, USA

Предложен алгоритм к сегментации клеток на изображениях иммуноцитохимических препаратов, основанный на сверточных нейронных сетях, представляющий собой сверточную сеть архитектуры U-net с предобученным энкодером. Показано, что его применение позволяет улучшить метрики сегментации (в частности, коэффициент Dice

и частоту ложного обнаружения клеток) по сравнению с классическим базовым алгоритмом сегментации. Внедрение предложенного алгоритма позволяет упростить работу патолога по определению HER2/neu статуса опухоли.

Ключевые слова: сегментация клеток, глубокие сверточные нейронные сети, анализ изображений.

Display Interfaces for the Control Unit of an Implantable Cardiac Pump

Цыа N. Rodionov, Igor V. Nesterenko, Dmitriy V. Telyshev, Ivan A. Sapozhkov 33

Интерфейсы дисплея блока управления имплантируемого кардиомонитора

Родионов И.Н., Нестеренко И.В., Тельшев Д.В., Сапожков И.А.

Национальный исследовательский университет «Московский институт электронной техники» (НИУ «МИЭТ»), Зеленоград, Россия

В процессе разработки кардиомонитора накладываются различные ограничения и требования на такие параметры, как потребление энергии, объем выводимой информации и т.д. В соответствии с поставленными задачами разработчику необходимо принять оптимально решение при выборе аппаратных компонентов. При работе с графическим дисплеем определяется интерфейс, который будет использоваться для передачи данных. В работе проводится анализ наиболее часто используемых интерфейсов для графических дисплеев, на основе которого можно принять решение, какой протокол выбрать, при тех или иных поставленных требованиях.

Ключевые слова: графический дисплей, шина данных, кардиомонитор, параллельные и последовательные интерфейсы, RGB интерфейс, передача данных.

Closed-loop system for blood glucose level control

Evgeniia Litinskaiia, Kirill Pozhar, Nikolai Bazaev, Pavel Rudenko, Viktor Grinvald and Andrey Chekasin 36

Система с обратной связью для контроля уровня концентрации глюкозы в крови

Литинская Е.И., Пожар К.В., Базеев Н.А., Руденко П.А., Гринвальд В.М., Чекасин А.И.

Национальный исследовательский университет «Московский институт электронной техники» (НИУ «МИЭТ»), Зеленоград, Россия

Представлена замкнутая система с обратной связью, позволяющая автоматически поддерживать КГК в пределах физиологической нормы с минимальным участием пациента. Система основана на помповой инсулинотерапии и неинвазивном мониторинге КГК спектроскопическим методом на мочке уха. Обратная связь по КГК осуществляется с помощью краткосрочного прогнозирования, задачей которого является обнаружение и коррекция ошибок в работе насоса инсулина или глюкометра, а также расчёт рекомендуемой дозы вводимого инсулина.

Ключевые слова: сахарный диабет, замкнутая система с обратной связью, контроль уровня глюкозы в крови, инсулинотерапия, неинвазивный глюкометр, краткосрочное прогнозирование.

Effect of thrombus formation on heat emission in Sputnik RBP

Andrey Porfiriyev, Dmitry Telyshev, Aleksandr Pugovkin and Sergey Selishchev 40

Влияние тромбообразования на теплогенерацию роторного насоса крови «Спутник»

Порфирьев А.О., Тельшев Д.В., Пуговкин А.А., Селищев С.В.

Национальный исследовательский университет «Московский институт электронной техники» (НИУ «МИЭТ»), Зеленоград, Россия

Показано определение характера тепловыделения при тромбозе аппарата вспомогательного кровообращения. Моделирование различных состояний системы осуществлялось путем варьирования частоты вращения насоса, изменения рабочей жидкости и местоположения тромбообразований. Результаты колебания температуры, полученные с поверхности насоса, позволяют определить наличие и расположение тромбообразования.

Ключевые слова: теплогенерация, роторный, тромбообразование насоса.

Surgery in the year 2030: Surgery 4.0?

Hubertus Feussner and Dirk Wilhelm 44

Хирургия в 2030 году: Хирургия 4.0

Фесснер Г., Вильгельм Д.

Технический университет Мюнхена

Рассмотрены современные направления развития хирургических вмешательств. Показано, что искусственный интеллект, робототехника, моделирование хирургических операций и многие другие принципы Хирургии 4.0 помогут сделать операцию более безопасной для пациента. Тем не менее, в обществах с высокоразвитой системой здравоохранения, не произойдет полной автономизации выполнения хирургических операций роботами.

Ключевые слова: хирургия, медицинская робототехника, интеллектуализация хирургии.

Intraoral Microfocus X-ray radiography in veterinary medicine

Yuriy Potrakhov and Nikolay Potrakhov 47

«Внутриротовая» микрофокусная рентгенография в ветеринарии

Потрахов Н.Н., Потрахов Ю.Н.

Санкт-Петербургский государственный электротехнический университет «ЛЭТИ» им. В.И. Ульянова (Ленина) СПбГЭТУ «ЛЭТИ»

Рассмотрены известные способы дентальной съемки в ветеринарии. Проанализированы их недостатки. Предложена оригинальная методика «внутриротовой» дентальной съемки. Описаны преимущества предложенной методики и представлены предварительные результаты исследования.

Ключевые слова: микрофокусная рентгенография, ветеринария, стоматология, панорамная рентгеновская трубка.

Specialized x-ray machine for neonatology

Vladimir Klonov, Ivan Larionov and Nikolay Potrahov 50

Специализированный рентгеновский аппарат для неонатологии

Клонов В.В., Ларионов И.А., Потрахов Н.Н.

Санкт-Петербургский государственный электротехнический университет «ЛЭТИ» им. В.И. Ульянова (Ленина)
СПбГЭТУ «ЛЭТИ»

Рассмотрен альтернативный подход к режиму рентгеновской диагностики новорожденных, позволяющий получать высокое качество снимков. Требования по выходным электрическим характеристикам при этом значительно снижаются, это даёт возможность реализовывать достаточно компактные и легкие устройства для портативного применения. Также представлена структура рентгеновского аппарата для неонатологии, а также особенности его конструкции, которые дают возможность реализовать максимально компактное и надежное в эксплуатации решение.

Ключевые слова: рентгеновское излучение, неонатология, диагностика, конструкция аппарата.

Computer program for setting up a medical X-ray apparatus

Ivan Larionov, Vladimir Klonov and Victor Bessonov 53

Компьютерная программа для настройки медицинского рентгеновского аппарата

Ларионов И.А., Клонов В.В., Бессонов В.Б.

Санкт-Петербургский государственный электротехнический университет «ЛЭТИ» им. В.И. Ульянова (Ленина)
СПбГЭТУ «ЛЭТИ»

Представлена программа по настройке и контролю рентгеновского медицинского устройства для неонатологии. Рассмотрены основные особенности схемы резонансного управления источником рентгеновского излучения. Описаны требования к программному обеспечению, налагаемые схемой и рабочими параметрами. Предложен вариант калибровки для рабочих параметров рентгеновского аппарата для медицинского применения.

Ключевые слова: рентгеновское излучение, программное обеспечение, неонатология, резонансная схема.

Digital X-ray image processing with using adaptive histogram equalization and adaptive background correction

Nikolai Staroverov, Artem Gryaznov and Kholopova Ekaterina 56

Цифровая обработка рентгеновских изображений с использованием адаптивной эквализации гистограммы и адаптивной коррекции фона

Староверов Н.Е., Грязнов А.Ю., Холопова Е.Д.

Санкт-Петербургский государственный электротехнический университет «ЛЭТИ» им. В.И. Ульянова (Ленина)
СПбГЭТУ «ЛЭТИ»

Рассмотрены два метода цифровой обработки микрофокусных рентгеновских изображений: алгоритм коррекции неравномерного фона изображения на основе вычитания искажающей функции и алгоритм локально-адаптивной эквализации гистограммы. Проведены исследования разработанных алгоритмов на выборках микрофокусных рентгеновских изображений. Оба метода показали удовлетворительные результаты.

Ключевые слова: микрофокусная рентгенография, эквализация гистограммы, цифровая обработка изображений.

2

«Biomedicine Radioengineering», 2018, № 6
(«Биомедицинская радиоэлектроника», 2018 г., №6)

Methods of investigation parameters of plasma of glow discharge lasers

Aleksandr Kiselev and Evgenij Smirnov 1(59)

Методика исследования параметров плазмы лазеров тлеющего разряда

Киселев А.С., Смирнов Е.А.

Санкт-Петербургский государственный электротехнический университет «ЛЭТИ» им. В.И. Ульянова (Ленина)
СПбГЭТУ «ЛЭТИ»

Произведен ряд экспериментальных и теоретических исследований параметров плазмы лазеров тлеющего разряда. Полученные результаты могут быть использованы при подборе оптимального газового наполнения, а также при разработке систем стабилизации мощности газоразрядных лазеров, используемых в медицинской технике.

Ключевые слова: лазеры тлеющего разряда, плазма, электронная температура, импеданс плазмы.

Study of the influence of the installation angle of the pedicular screw on its resistance to axial traction

Savrasov G.V., Sayfutdinova M.S., Makirov S.K., Makirov T.R. 5(63)

Исследование влияния угла установки винта в модуль биомодели на его сопротивление осевому вытяжению

Саврасов Г.В.¹, Сайфутдинова М.С.¹, Макиров С.К.², Макиров Т.Р.²

¹ МГТУ имени Н.Э. Баумана, Москва, Россия

² Центральная клиническая больница Российской академии наук, Москва, Россия

Проведено экспериментальное исследование влияния угла установки транспедикулярного винта на его сопротивление осевому вытяжению. Винт вводили в модель биообъекта (тело позвонка барана) под углом по отношению к оси вытягивания. Исследование подтверждает, что увеличение угла приводит к ухудшению фиксации винта в позвонке: при наклоне $5\pm 0,5^\circ$ сила сопротивления составила 1208 ± 6 Н; при наклоне $14\pm 0,5^\circ$ – 965 ± 5 Н; при наклоне $28\pm 0,5^\circ$ – 303 ± 2 Н.

Ключевые слова: винт транспедикулярный, фиксация позвоночника, сопротивление осевому вытягиванию, биомеханические исследования.

The study of biomechanical characteristics of the venous wall after ultrasound exposure

Anna Borde, Savrasov Gennady, Alexander Gavrilenko and Alexandera Ivanova 7(65)

Изучение влияния ультразвука на биомеханические характеристики венозной стенки

Борде А.С.¹, Саврасов Г.В.¹, Гавриленко А.В.², Иванова А.Г.²

¹ МГТУ имени Н.Э. Баумана, Москва, Россия

² РНЦХ им. Б.В. Петровского

В процессе отработки технологических параметров ультразвуковой абляции вен нижних конечностей необходимым этапом является исследование структуры патологической венозной стенки после ультразвукового воздействия. Об изменениях в структуре биоткани можно судить посредством косвенных показателей, таких как биомеханические характеристики. В работе приведены результаты экспериментальных исследований по изучению изменений биомеханических характеристик венозной стенки после ультразвуковой абляции.

Ключевые слова: варикозная болезнь вен нижних конечностей, ультразвуковая хирургия, биомеханические испытания.

Solid Angle Fraction in Single-Photon Emission Computed Tomography

Alexander Lysenko and Sergey Tereshchenko 9(67)

Геометрическое ослабление в однофотонной эмиссионной томографии

Лысенко А.Ю., Терещенко С.А.

Национальный исследовательский университет «Московский институт электронной техники» (НИУ «МИЭТ»), Зеленоград, Россия

В однофотонной эмиссионной томографии существует малоисследованный искажающий фактор, называемый геометрическим ослаблением. В работе исследуется влияние геометрического ослабления на качество реконструкции, в зависимости от размеров объекта и радиуса вращения системы. Для коррекции искажений, вызванных фактором геометрического ослабления, разработан новый итерационный метод.

Ключевые слова: эмиссионная томография, реконструкция, интегрально-итерационный алгоритм, геометрическое ослабление.

Animal Trials of Wearable Apparatus for Peritoneal Dialysis

Nikolay Bazaev, Natalia Dorofeeva, Victor Grinvald', Boris Putrya and Nikita Zhilo 12(70)

Испытания носимого аппарата перитонеального диализа на животных

Базаев Н.А., Дорофеева Н.И., Гринвальд В.М., Путря Б.М., Жило Н.М.

Национальный исследовательский университет «Московский институт электронной техники» (НИУ «МИЭТ»), Зеленоград, Россия

Приведены результаты медико-биологических испытаний носимого аппарата внепочечного очищения крови на базе перитонеального диализа с регенерацией. Основная идея метода регенерации заключалась в прямом анодном окислении мочевины с последующей сорбцией продуктов электролиза активированным углём. Представлены данные по изменению концентрации азотсодержащих соединений в диализате в ходе испытаний аппарата на животных.

Ключевые слова: регенерация диализата, носимый аппарат искусственного очищения крови, перитонеальный диализ, медико-биологические испытания.

The control method of peripheral venous catheters automatic insertion using force measurement

Ivan Kudashov and Sergey Igorevich Shchukin 15(73)

Контроль установки периферических венозных катетеров с помощью измерения силы, действующей на иглу

Кудашов И.А., Щукин С.И.

МГТУ имени Н.Э. Баумана, Москва, Россия

Представлено устройство обратной связи на основе тензорезистивного датчика силы, интегрированного в автоматическую систему контроля и проведения пункции венозных сосудов. На основе полученных данных предложен алгоритм идентификации прокола стенки вены.

Ключевые слова: венеопункция, датчик силы, катетер, автоматизированная система.

Diamond and Platinum Electrodes For Urea Electrochemical Oxidation

Bazaev Nikolay, Boris Putrya and Evgeniy Streltsov 18(76)

Алмазные и платиновые электроды для электрохимического окисления мочевины

Базаев Н.А.¹, Путря Б.М.¹, Стрельцов Е.В.¹

Национальный исследовательский университет «Московский институт электронной техники» (НИУ «МИЭТ»), Зеленоград, Россия

Различные методы регенерации отработанного диализата могут быть использованы при миниатюризации аппаратов внепочечного очищения. Исследован метод электрохимического окисления мочевины. В качестве объекта исследования были выбраны платиновые и алмазные электроды. Приведено теоретическое обоснование метода, а также экспериментальные результаты по скорости элиминации мочевины на выбранных электродных образцах.

Ключевые слова: регенерация диализата, электролиз, носимый аппарат искусственного очищения крови.

The influence assessment of reversible chess pattern size and biological object parameters on visual evoked potential detection

Irina Kuvshinova and Alexander Dmitriev 22(80)

Оценка влияния размера реверсивного шахматного паттерна и параметров биологического объекта на выделение зрительных вызванных потенциалов

Кувшинова И.С.¹, Дмитриев А.Н.¹

МГТУ имени Н.Э. Баумана, Москва, Россия

Рассмотрена методика зрительной стимуляции с использованием различных размеров фотостимуляционной матрицы, позволяющая увеличить точность локализации нарушений функциональной активности зрительной коры. Цель работы – оценка параметров стимуляции на реверсивный шахматный паттерн и электрофизических параметров на амплитуду зрительных вызванных потенциалов.

Ключевые слова: зрительные вызванные потенциалы (ЗВП), реверсивный шахматный паттерн (РШП), режим стимуляции, светодиодная матрица, амплитуда диполя, толщина черепа.

Algorithm of physical activity detection according to the accelerometer data of implantable pacemaker with rate-adaptive pacing

Anna Krechetova, Lidia Komleva and Alexey Tikhomirov 25(83)

Алгоритм выбора физической активности по данным акселерометра имплантируемого кардиостимулятора с функцией частотной адаптации

Кречетова А.В.¹, Комлева Л.С.¹, Тихомиров А.Н.¹

МГТУ имени Н.Э. Баумана, Москва, Россия

Функция частотной адаптации улучшает качество жизни пациентов с имплантируемыми кардиостимуляторами. Однако, точность современных алгоритмов не является достаточной для полноценной жизни пациентов. Показан новый алгоритм для выбора физической активности по данным акселерометра.

Ключевые слова: частотная адаптация, кардиостимулятор, акселерометр.

Multidiagnostics study of postoperative cognitive disorders

Tatiana Istomina, Aleksey Safronov, Leonid Krivonogov, Sofia Karpitskaja, Mihail Kramm,

Nikita Kosenok and Elena Shachneva 28(86)

Мультидиагностическое исследование послеоперационных когнитивных расстройств

Истомина Т.В.¹, Сафронов А.И.², Кривоногов Л.Ю.³, Карпицкая С.А.², Крамм М.Н.⁴,

Косенок Н.Ю.¹, Шачнева Е.А.³

¹ Пензенский государственный технологический университет

² Пензенский институт повышения квалификации Министерства здравоохранения Российской Федерации

³ Пензенский государственный университет

⁴ Московский энергетический институт

Проведено исследование информативности компьютерной стабиллографии совместно с электрокардиографией для изучения проявлений послеоперационной когнитивной дисфункции и поиска адекватной анестезии. Результаты исследований подтвердили возможность использования стабиллографии в качестве источника количественных данных о когнитивной дисфункции и инструмента для оптимизации анестезии при лапароскопической холецистэктомии.

Ключевые слова: стабиллография, электрокардиография, послеоперационная когнитивная дисфункция.

Evaluation of the electrode system pressure force influence on neuro muscular activity signals

Andrey Briko, Chvanova Julia, Alexander Kobelev and Sergey Shchukin 32(90)

Оценка влияния силы прижатия электродной системы на сигналы нейромышечной активности

Брико А.Н., Чванова Ю.А., Кобелев А.В., Шукин С.И.

МГТУ имени Н.Э. Баумана, Москва, Россия

Представлено сравнение трех основных методов регистрации нейромышечной активности посредством регистрации электромиограммы, сигнала биоимпеданса и миотонического сигнала. Оценено влияния силы прижатия электродной системы на сигналы нейромышечной активности. Измерения проводились при изометрическом схватке на специальном стенде, конструкция которого описана в работе.

Ключевые слова: сигналы нейромышечной активности, электромиография, биоимпеданс, миотонический метод, сила прижатия электродов, изометрический схват, стенд схвата.

A Database with face video images of patients with schizophrenic disorders and control healthy group

E.Yu. Lатыsheva, M.N. Pilipenko, A.A. Boiko, A.V. Samorodov, M.A., Omelchenko,

A.O. Rummyantsev, A.M. Ivanova and D.D. Volovik 36(94)

База видеоизображений лиц пациентов с расстройствами шизофренического спектра и контрольной группы

Латышева Е.Ю.¹, Пилипенко М.Н.¹, Бойко А.А.¹, Самородов А.В.¹, Омельченко М.А.²,

Румянцев А.О.², Иванова А.М.², Воловик Д.Д.²

¹ МГТУ имени Н.Э. Баумана, Москва, Россия

² НИЦПЗ

Разработана база видеоизображений лиц пациентов, больных расстройствами шизофренического спектра, а также группы нормы. Данные заболевания характеризуются негативными симптомами в поведении, а именно в лицевой экспрессии. Описана процедура регистрации видеоизображений, указаны критерии отбора участников исследования, представлена оценка качества ручной аннотации базы.

Ключевые слова: изображение, лицо, база данных, шизофрения.

Artificial Muscles with the Possibility of Application in Medical Practice
Levan Ichkitidze, Sergei Selilshchev, Alexander Gerasimenko and Natali Demidenko 38(96)

Искусственные мышцы с возможностью применения в медицинской практике

Ичкитидзе Л.П., Селищев С.В., Герасименко А.Ю., Демиденко Н.А.

Национальный исследовательский университет «Московский институт электронной техники» (НИУ «МИЭТ»), Зеленоград, Россия

Проанализированы научные источники относительно искусственных мышц и приводов на основе многочисленных материалов и наноматериалов с возможностью применения в медицинской практике. Отмечено, что искусственные мышцы из углеродных нанотрубок и наноматериалов на их основе показывают приемлемые физико-механические параметры, но требуют устранения недостатков: высокая стоимость, низкая надежность, низкая степень биосовместимости.

Ключевые слова: приводы, искусственные мышцы, удельная мощность, наноматериалы, углеродные нанотрубки, биосовместимость.

Optimization of the prophylaxis of critical ischemia of lower extremities on the basis of fuzzy models for assessing the dynamics of the disease

Aleksandr Bykov, Nikolay Korenevskiy, Sergey Parkhomenko and Irina Khripina 42(100)

Оптимизация профилактики критической ишемии нижних конечностей на основе нечетких моделей оценки динамики заболевания

Быков А.В.¹, Корневский Н.А.², Пархоменко С.А.³, Хрипина И.И.²

¹ Консультативная клиника БМУ «Курская областная клиническая больница» комитета здравоохранения Курской области, Курск, Россия

² ФГБОУ ВО «Юго-Западный государственный университет», Курск, Россия

³ ФГБУ «3 Центральный Военный Клинический Госпиталь им. А.А. Вишневецкого», Москва, Россия

Получены математические модели для прогноза динамики развития критической ишемии нижних конечностей. Разработан алгоритм выбора оптимальных превентивных мер. Показана возможность уменьшения количества ампутаций нижних конечностей у пациентов, коррекции гемореологии и уменьшения тяжести состояния.

Ключевые слова: гибридные нечеткие модели, модель принятия решения, критическая ишемия нижних конечностей.

Arrhythmia Analysis in a Non-contact cECG Chair using Convolutional Neural Network

Anake Pomprapa, Waqar Ahmed, André Stollenwerk, Stefan Kowalewski and Steffen Leonhardt 45(103)

Исследование аритмии на ЭКГ, зарегистрированной бесконтактными емкостными электродами, с использованием сверточных нейронных сетей

Помпрапа А., Ахмед В., Штолленверк А., Ковалевски С., Леонард С.

Рейнско-Вестфальский технический университет Аахена

Для классификации аритмических состояний на четыре основные категории применена шестислойная сверточная нейронная сеть глубинного обучения. Продемонстрирована возможность отслеживания и классификации аритмического состояния емкостными бесконтактными электродами в реальном масштабе времени с использованием архитектуры последовательного анализа, основанной на банке биортогональных вейвлетов.

Ключевые слова: анализ электрокардиограммы, бесконтактная электрокардиография, емкостные электроды, сверточная нейронная сеть, сердечная аритмия.

Apnea Detection in a Contactless Multisensor System using Deep Learning Algorithm

Anake Pomprapa, Mohammad Salman Sayani, Toni Anwar, André Stollenwerk, Stefan Kowalewski and Steffen Leonhardt 49(107)

Обнаружение апноэ бесконтактной мультисенсорной системой

с использованием алгоритмов глубинного обучения

Помпрапа А.¹, Саянти М.С.¹, Анвар Т.², Штолленверк А.³, Ковалевски С.³, Леонард С.¹

¹ Рейнско-Вестфальский технический университет Аахена, Германия

² Технологический университет Петронас, Перак, Малайзия

³ Рейнско-Вестфальский технический университет Аахена, Германия

Для обнаружения апноэ на данных, полученных у пяти здоровых добровольцев, применена гибридная модель глубинного обучения, основанная на сверточной и рекуррентной нейронных сетях. Продемонстрирована возможность обнаружения апноэ предложенной бесконтактной мультисенсорной системой с потоковой и пакетной обработкой данных в реальном масштабе времени с использованием лямбда-архитектуры. Система может быть использована для обнаружения экстренных состояний или для долгосрочной диагностики.

Ключевые слова: сверточная нейронная сеть, рекуррентная нейронная сеть, лямбда-архитектура, синдром обструктивного апноэ во сне, индекс апноэ-гипопноэ, индекс дыхательной недостаточности.

A Noninvasive Glucose Estimation based on Near Infrared Spectroscopy and Pulse-Echo Ultrasound

Souransu Nandi, Ye Zhan, Jun Xia, Tarunraj Singh and Lucy Mastrandrea 53(111)

Неинвазивная оценка уровня глюкозы, основанная на спектроскопии

в ближней инфракрасной области и эхо-импульсном ультразвуке

Нанди С., Жан И.,ZIA Дж., Синг Т., Мاستрандреа Л.

Университет Баффало, Баффало, США

Предложен метод неинвазивной оценки уровня глюкозы, основанный на двух способах измерения для увеличения точности. В ходе экспериментальных исследований *in-vitro* показано, что предложенный метод потенциально обладает наилучшими характеристиками среди аналогов. Для оценки уровня глюкозы использованы модели линейной регрессии и гауссова процесса, с последующим объединением результатов. Работа является основой для дальнейшего проведения экспериментов *in-vivo*.

Ключевые слова: оценка уровня глюкозы, спектроскопия в ближней инфракрасной области, эхо-импульсный ультразвук, линейная регрессия, гауссов процесс.

“Biomeditsinskaya radioelektronika” (Biomedicine Radioengineering) is a scientific and technical journal devoted to biomedicine technologies and electromagnetic oscillations influence on biological objects. Established in 1998.

Полный список опубликованных в журналах статей, а также аннотации к ним Вы найдете на нашем сайте <http://www.radiotec.ru>



Учредитель ООО «Издательство «Радиотехника». Свидетельство о регистрации № 016200 от 10 июня 1997 г.
Сдано в набор 16.04.2017. Подписано в печать 10.05.2018. Печ. л. 11. Тираж 500. Изд. № 77.

107031, Москва, К-31, Кузнецкий мост, д. 20/6. Тел./факс +7(495)621-4837
info@radiotec.ru

Дизайн и допечатная подготовка ООО «САЙНС-ПРЕСС».

Отпечатано с предоставленных готовых файлов в полиграфическом центре ФГУП «Издательство «Известия». 127254, ул. Добролюбова, д. 6.
Контактный телефон: (495)650-38-80. Заказ №

ISSN 1560-4136

© ООО «Издательство «Радиотехника», 2018

Незаконное тиражирование и перевод статей, включенных в журнал, в электронном и любом другом виде запрещено и карается административной и уголовной ответственностью по закону РФ «Об авторском праве и смежных правах»

Tissue layers three-dimensional structure formation by nanosecond la-ser pulses

P.N. Vasilevsky¹, A.Yu. Gerasimenko^{1,2}, M.S. Savelyev^{1,2}, S.A. Tereschenko¹

¹National Research University of Electronic Technology, Zelenograd, Russia

²I.M. Sechenov First Moscow State Medical University, Moscow, Russia

Contact: savelyev@bms.zone

Introduction

Carbon nanotubes (CNTs) attract the attention of researchers due to their electronic, optical, thermal and mechanical properties [1]. Thus, there is a tendency to increase the applicability of CNTs for the nanomaterials creation for various purposes, including medical ones.

This work is devoted to the creation of three-dimensional tissue-engineered structures based on albumin and collagen proteins with an inner scaffold made of CNTs. Such structures are well suited as implants for the cardiovascular system due to their high biocompatibility, ability to biodegradation [2] and ensuring the germination of blood vessels net.

Therefore, it is obvious that it is necessary to obtain detailed information on the structural changes that occur during laser radiation influence. Under the influence of this kind of high-intensity radiation on the local area of protein dispersion with CNTs, phase transformations with the formation of a three-dimensional tissue-engineered structure take place. And in the case of using laser beams of nanosecond duration, nonlinear effects arise. That is why it is necessary to conduct Z-scan and fixed sample location experiments to determine the dependence of the total absorption coefficient on the intensity, which is important to consider during the formation of the tissue-engineered structure [3].

As a result of this work, nonlinear properties of protein aqueous dispersions with CNTs were determined using a method based on the radiation transfer equation [4]. The beam radius values were measured depending on the location of sample relative to the focus of the lens and a comparison of these data with the theoretical ones was made. In this way, the values of the input light fluence which fell on the local region of the sample during the formation of the tissue-engineered structure were determined.

Materials and Methods

Aqueous dispersions of bovine serum albumin (BSA) with a concentration of 25% and bovine collagen (BC) with a concentration of 2% and similar dispersions with single-walled carbon nanotubes (SWCNTs) were investigated in the study.

To prepare the dispersion with CNTs, they were premixed in a homogenizer with water with a mass concentration of 0.03% until a homogeneous solution was obtained. This solution was then mixed with the protein water dispersion and processed in an ultrasonic bath for 40 minutes.

Results

As shown in fig. 1, as the input energy density increases, the BSA dispersion with CNTs exhibits strong nonlinear effects (fig. 1b). This is reflected in the sharp weakening of the normalized transmission and, correspondingly, in the increase of the laser radiation absorption. An absorptivity increase is also observed for the dispersion without CNTs, but it is insignificant (fig. 1a). The theoretical curves were plotted from the results of optical parameters calculations.

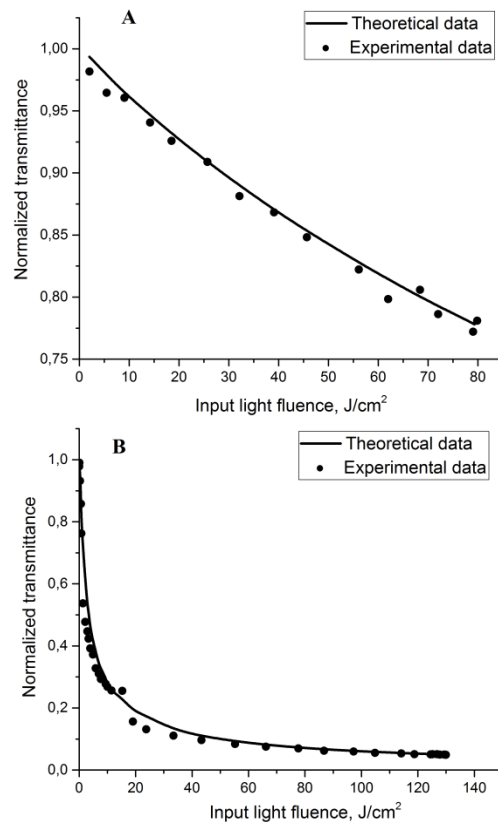


Figure 1: Normalized transmittance dependence on input light fluence for: A – BSA, B – BSA+SWCNT

Fig. 2 shows the normalized transmittance for collagen dispersions without nanotubes (fig. 2a) and with nanotubes (fig. 2b). To better trace the behavior of the sample at low values of the input light fluence, the dependence data are presented on a logarithmic scale. Collagen dispersion also shows an increase of the laser radiation absorption when CNTs were added, but it is weaker than for BSA dispersions. The nonlinear properties of protein dis-

persions with single-walled carbon nanotubes are also confirmed by the calculated calculations.

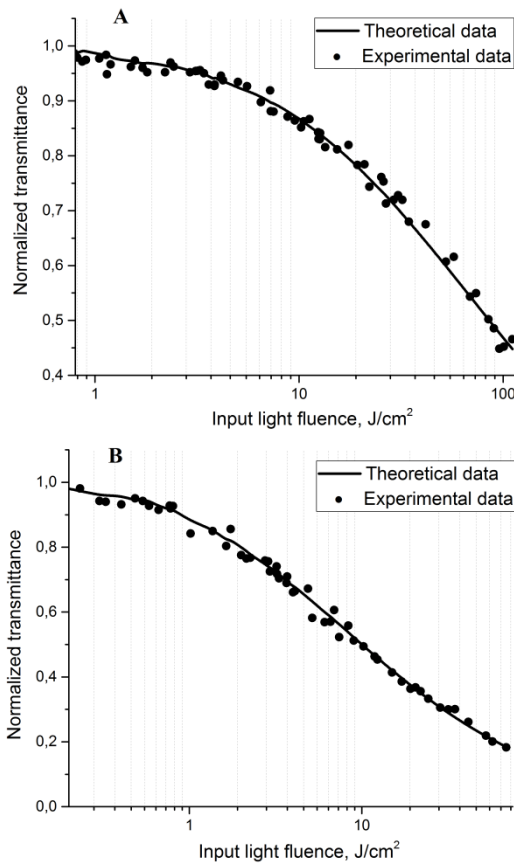


Figure 2: Normalized transmittance dependence on input light fluence for: A – BC, B – BC+SWCNT

Calculations were made using a method based on the radiation transfer equation. When carbon nanotubes were added, the value of the linear absorption coefficient increased however, this growth was insignificant. Albumin and collagen water dispersions without CNTs showed values of the linear absorption coefficient $\alpha = 1.92 \text{ cm}^{-1}$ and $\alpha = 2.16 \text{ cm}^{-1}$ respectively, and the same dispersions with carbon nanotubes showed $\alpha = 2.7 \text{ cm}^{-1}$ and $\alpha = 2.94 \text{ cm}^{-1}$.

Unlike linear absorption, the value of the nonlinear absorption coefficient increased significantly with the addition of carbon nanotubes. For dispersions without CNTs, the nonlinear absorption coefficient β was 4 cm/GW and 5.9 cm/GW for albumin and collagen respectively, and for similar dispersions with CNTs $\beta = 345 \text{ cm/GW}$ and $\beta = 66.9 \text{ cm/GW}$.

Also, for the suspensions studied, the threshold light fluence values, at which nonlinear effects begin to occur were calculated for studied dispersions. For pure aqueous dispersions of albumin and collagen, this values were 6 mJ/cm^2 and 8.5 mJ/cm^2 respectively, and for dispersions with nanotubes they were 51 mJ/cm^2 and 25.5 mJ/cm^2 .

The calculated values of the waist radius for all the experiments were $23 \pm 3 \text{ }\mu\text{m}$. Knowing the value of the radius of

the beam in the neck, the beam radius values at any point can be calculated as:

$$\omega(z) = \omega_0 \sqrt{1 + \left(\frac{\lambda z}{\pi \omega_0^2}\right)^2} \quad (1)$$

where ω_0 – laser beam waist, $\omega(z)$ – laser beam radius at any point of the optical axis Z.

To verify the correspondence of the used laser beam to the Gaussian beam, the beam radius depended on the distance from the focus of the lens was studied. To do this, the CCD camera was placed on a mechanized ruler and similarly to the Z-scan experiment was moved relatively to the focus of the lens. As a result, experimental values of the beam radius at different points were obtained, which correlate well with the theoretical values (fig. 3).

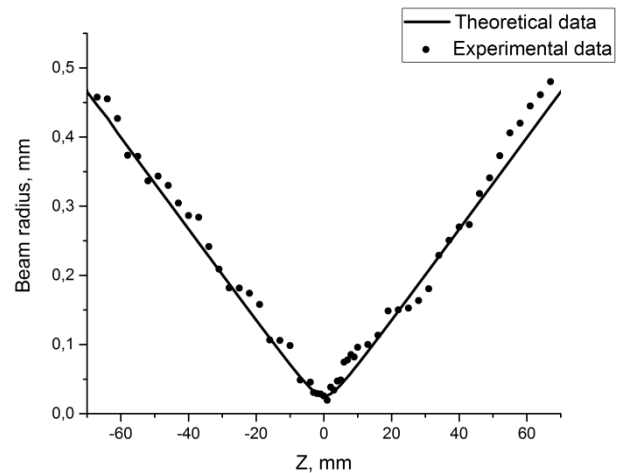


Figure 3: Beam radius dependence on optical axis Z displacement

Conclusions

An increase of the nonlinear absorption coefficient with the addition of CNTs suggests that it is the nanotubes that absorb most of the laser radiation as its light fluence increases, and thus reduce the effect of the laser on the proteins. Absorbing laser radiation, nanotubes heat up and transfer heat to the medium, which leads to the creation of a solid composite. Thus, proteins are less damaged in the formation of three-dimensional structures by laser printing methods.

References

- [1] S. Iijima. Helical microtubules of graphitic carbon, *Nature* 354: 56–58, 1997.
- [2] A. Parag, J.B. Hall, C.B. McLeland, M.A. Dobrovolskaia, S.E. McNeil. Nanoparticle interaction with plasma proteins as it relates to particle biodistribution, biocompatibility and therapeutic efficacy, *Advanced drug delivery reviews* 61: 428–437, 2009.
- [3] Balu M. White-light continuum Z-scan technique for nonlinear materials characterization, *Optics Express* 12(16): 3820–3826, 2004.
- [4] Tereshchenko S.A., Podgaetsky V.M. Determining the parameters of the laser radiation intensity limiter based on a time-dependent equation of radiative transfer in a nonlinear medium, *Quantum electron.* 41(1): 26–29, 2011.



Acknowledgements

This work was provided by the Ministry of Education and Science of the Russian Federation (Agreement 14.578.21.0234 RFMEFI57817X0234).

Biotechnical system for automatic assessment of facial nerve dysfunction rate

E.A. Lavrova¹, A.V. Samorodov¹, A.V. Mordovsky², K.G. Kudrin², A.P. Polyakov²

¹Bauman Moscow State University, Moscow, 2nd Baumanskaya Street, 5, Russia

²Hertsen Moscow Oncology Research Center, Moscow, 2nd Botkinsky Passage, 3, Russia

Contact: lavrovaliz@gmail.com

Introduction

Recently in the field of maxillofacial surgery there is a growing number of patients with facial palsy. Assessment of the facial nerve dysfunction rate is needed for planning of treatment, for monitoring of rehabilitation efficiency and for prediction of patient's state [1]. In clinical experience and research studies to estimate facial nerve dysfunction rate scaling systems are implemented (House-Brackmann, Sunnybrook, Yanagihara, Nottingham, eFACE [2]). As follows from the analysis of the existing methods, all of them have two crucial disadvantages: biased approach and nonuniversality [1].

It is determined that facial nerve dysfunction severity is related to facial muscles dysfunction, which means that it is related to facial lateral asymmetry level. Consequently, it is possible to estimate facial nerve dysfunction rate by applying biometric facial video analysis, based on the measuring of anthropometric features of the facial region. Therefore, development of the biotechnical system for automatic assessment of facial nerve dysfunction rate based on biometric facial video analysis is relevant.

Materials and Methods

In the framework of the present research biotechnical system for automatic assessment of facial nerve dysfunction rate based on biometric facial video analysis is proposed. Figure 1 shows the structure of the system.

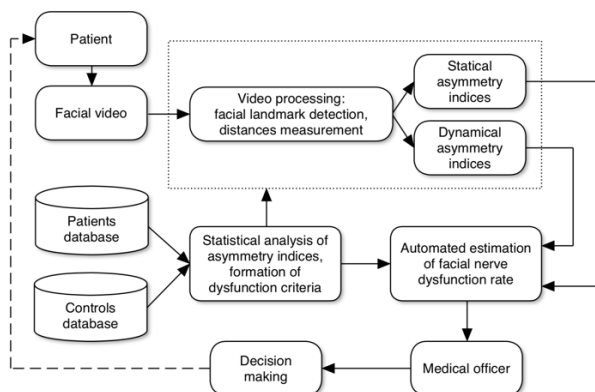


Figure 1: Structure of biotechnical system for automatic assessment of facial nerve dysfunction rate

In the framework of the proposed method, video, containing patient's facial movements, is to be captured, facial video processing (including 2 stages: facial landmark de-

tection and distances measurement) is to be performed, static and dynamical asymmetry indices, based on relative shift of facial landmarks, are to be estimated. Based on databases of patients and control set, statistical analysis of asymmetry indices is to be held, resulting in formation of dysfunction criteria. Therefore, based on asymmetry indices, automated estimation of facial nerve dysfunction rate is to be performed.

Within this research data recording technique is developed. In its framework, the experimental subject is positioned at a distance of 1 meter to camera (Logitech HD, 1920×1080, 15 fps) against the homogenous background. The face position is frontal. The experimental subject is asked to perform the following movements: demonstration the face at rest, eye squeeze, raising the eyebrows, smiling, forcefully smiling, combining lips a tubule, cheeks puffing, articulating, forced articulating (with overacting amplitude of lips movements).

Facial landmarks detection is implemented with dlib library [3] with 42 enabled facial landmark points of the 68 points MultiPIE/IBUG face model [4] (is shown on Figure 2).

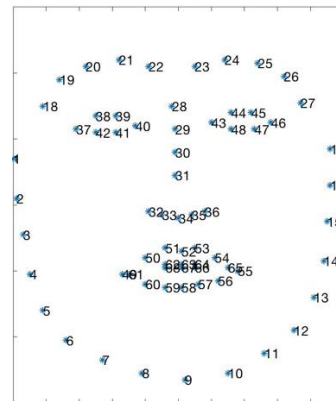


Figure 2: Facial landmarks configuration of the MultiPIE/IBUG face model

Facial asymmetry rate estimations are based on evaluation of relative shift of groups of landmarks. Preliminary facial asymmetry rate estimation (point and integral) is performed for 15 patients and 17 representatives from control set at the premises of Hertsen Moscow Oncology Research Center and Bauman Moscow State University. Point asymmetry rate estimations include asymmetry indices of forehead and mouth regions [5] ("0" corresponds

to totally asymmetrical movement, “1” corresponds to totally symmetrical movement).

Forehead asymmetry rate is based on estimation of the rate of relative shift of eye and eyebrow points from left and right forehead regions (points P_{18} - P_{22} respective to points P_{37} - P_{42} and points P_{23} - P_{27} respective to points P_{43} - P_{48}). The basic principles are described below:

a) estimation of mean eyebrow points LEB and REB :

$$LEB = \frac{1}{5} \sum_{i=18}^{22} P_i, REB = \frac{1}{5} \sum_{i=23}^{27} P_i,$$

b) estimation of mean eye points LEC и REC :

$$LEC = \frac{1}{6} \sum_{i=37}^{42} P_i, REC = \frac{1}{6} \sum_{i=43}^{48} P_i,$$

c) estimation of distances D_{REB} and D_{LEB} between mean eye and eyebrow points on the left and on the right sides:

$$D_{LEB} = d(LEB, LEC), D_{REB} = d(REB, REC),$$

where d – distance measure,

d) estimation of relative shifts Δ_L^f and Δ_R^f of the forehead region points on the left and on the right sides:

$$\Delta_L^f = \left| \max_i(D_{LEB_i}^{test}) - \bar{D}_{LEB}^{rest} \right|,$$

$$\Delta_R^f = \left| \max_i(D_{REB_i}^{test}) - \bar{D}_{REB}^{rest} \right|,$$

where D_{LEB}^{rest} and D_{REB}^{rest} – distances between mean eye and eyebrow points on the left and on the right sides at rest, D_{LEB}^{test} and D_{REB}^{test} – distances between mean eye and eyebrow points on the left and on the right sides during the facial movements, i – number of videoframe,

e) estimation of indice r_f , which reflects the shift between left and right parts of forehead region:

$$r_f = \begin{cases} \frac{\Delta_R^f}{\Delta_L^f} & \text{if } \Delta_L^f > \Delta_R^f \\ \frac{\Delta_L^f}{\Delta_R^f} & \text{otherwise.} \end{cases}$$

Mouth asymmetry rate is based on estimation of the rate of relative shift of mouth corners points from left and right sides and mouth center points (points P_{49} and P_{55} respective to points P_{52} , P_{63} , P_{67} , P_{58}). The basic principles are described below:

a) estimation of mean distances D_{LM} and D_{RM} between mouth corners points P_{49} and P_{55} and mouth center points P_{52} , P_{63} , P_{67} , P_{58} :

$$D_{LM} = \frac{1}{4} (d(P_{49}, P_{52}) + d(P_{49}, P_{63}) + d(P_{49}, P_{67}) + d(P_{49}, P_{58})),$$

$$D_{RM} = \frac{1}{4} (d(P_{55}, P_{52}) + d(P_{55}, P_{63}) + d(P_{55}, P_{67}) + d(P_{55}, P_{58})),$$

b) estimation of shifts Δ_L^m and Δ_R^m from the left and from the right sides:

$$\Delta_L^m = \left| \max_i(D_{LM_i}^{test}) - \bar{D}_{LM}^{rest} \right|,$$

$$\Delta_R^m = \left| \max_i(D_{RM_i}^{test}) - \bar{D}_{RM}^{rest} \right|,$$

where \bar{D}_{LM}^{rest} and \bar{D}_{RM}^{rest} – mean distances between mouth corners points and mouth center points at rest, $D_{LM_i}^{test}$ and $D_{RM_i}^{test}$ – distances between mouth corners points and mouth center points during the facial movements, i – number of videoframe,

c) estimation of indice r_m , which reflects the shift between left and right parts of mouth region:

$$r_m = \begin{cases} \frac{\Delta_R^m}{\Delta_L^m} & \text{if } \Delta_L^m > \Delta_R^m \\ \frac{\Delta_L^m}{\Delta_R^m} & \text{otherwise.} \end{cases}$$

Integral asymmetry rate estimations include distances between relative shift curves (“0” corresponds to totally symmetrical movement), normalized by number of frames and by image scale (defined as average number of pixels between eyes).

Results

Table 1 shows the results of experimental evaluation of asymmetry indices of forehead region during eye squeeze, raising the eyebrows, smiling, forcefully smiling, combining lips a tubule, cheeks puffing, articulating, forced articulating. The median and also lower and upper quartiles are presented. The presented asymmetry indices correspond to point asymmetry rate estimation.

Table 1: Asymmetry indices of forehead region

Movement	Control set			Patients		
	Q_2	Q_1, Q_3	Q_2	Q_1, Q_3	Q_2	Q_1, Q_3
Eye squeeze	0,85	0,73 0,88	0,58	0,43 0,78		
Raising the eyebrows	0,96	0,94 0,98	0,63	0,41 0,71		
Smiling	0,82	0,70 0,94	0,45	0,26 0,54		
Forcefully smiling	0,83	0,74 0,93	0,76	0,65 0,77		
Combining lips a tubule	0,83	0,63 0,88	0,67	0,46 0,74		
Cheeks puffing	0,87	0,74 0,94	0,44	0,22 0,63		
Articulating	0,75	0,67 0,91	0,76	0,51 0,93		
Forced articulating	0,82	0,68 0,89	0,59	0,37 0,72		

Table 2 shows the results of experimental evaluation of normalized areas between relative shift curves of forehead regions during eye squeeze, raising the eyebrows, smiling, forcefully smiling, combining lips a tubule, cheeks puffing, articulating, forced articulating. The presented values of areas correspond to integral asymmetry rate estimation.

Table 2: Normalized areas between relative shift curves of forehead regions

Movement	Control set			Patients		
	Q_2	Q_1, Q_3	Q_2	Q_1, Q_3	Q_2	Q_1, Q_3
Eye squeeze	0,08	0,06 0,11	0,46	0,36 0,62		
Raising the eyebrows	0,09	0,07 0,14	0,42	0,30 0,60		
Smiling	0,06	0,04 0,07	0,70	0,37 0,80		
Forcefully smiling	0,06	0,05 0,10	0,56	0,35 0,81		
Combining lips a tubule	0,06	0,05 0,07	0,57	0,36 0,77		
Cheeks puffing	0,05	0,05 0,06	0,57	0,29 0,68		
Articulating	0,05	0,05 0,07	0,76	0,36 0,84		
Forced articulating	0,06	0,05 0,07	0,65	0,42 0,81		

Discussion

Point and integral asymmetry rate estimation is performed. According to Wilcoxon signed-rank test, it is possible to assume with confidence level of 0,1, that the estimated asymmetry rates in groups of patients and controls have statistically meaningful differences.

Performed point asymmetry rate estimations are based on peak amplitudes acquired from series of videoframes. Therefore, in general, peak amplitudes from different videoframes can be used for single asymmetry rate estimation. This results in upward bias of asymmetry rate estimation and downward bias of test-sensitivity in case of facial nerve dysfunction. Consequently, it is reasonable to use integral asymmetry rate estimations based on dynamical features acquired from each frame.

Conclusions

According to results of preliminary facial asymmetry rate estimation, it's reasonable to develop integral facial asymmetry rate based on dynamic features. At this moment set of these features is under exploration.

References

- [1] T. Hadlock, L. Urban. Toward a universal, automated facial measurement tool in facial reanimation. *Arch Facial Plast Surg*, Vol. 14(4), 277-282, 2012.
- [2] A.Y. Fattah et al. Facial nerve grading instruments: systematic review of the literature and suggestion for uniformity. *Plastic and Reconstructive Surgery*, Vol. 135(2), 569-579, 2015.
- [3] D.E. King. Dlib-ml: A machine learning toolkit. *Journal of machine learning research*, Vol. 10, 1755-1758, 2009.
- [4] C. Sagonas. et al. Incremental face alignment in the wild. 300 faces In-the-wild challenge: Database and results, 2016.
- [5] H.S. Kim et al. A smartphone-based automatic diagnosis system for facial nerve palsy. *Sensors*, Vol. 15, 26756-26768, 2015.

Variation in Local Pulse Wave Velocity over the Cardiac Cycle: *In-Vivo* Validation using Dual-MPG Arterial Compliance Probe

Nabeel P M¹, Jayaraj Joseph², Mohanasankar Sivaprakasam^{1,2}

¹Department of Electrical Engineering, Indian Institute of Technology Madras, Chennai, India

²Healthcare Technology Innovation Centre, Indian Institute of Technology Madras, Chennai, India
Contact: nabeelnpm@gmail.com

Introduction

The biomechanical characteristics of arterial vessels assessed from a short segment (local estimates) are key cardiovascular clinical markers [1]. Local measurement of artery condition has the potential to quantify the prognostic value for the prediction of cardiovascular morbidity and mortality. The elastic properties of large arteries affect locally during the pathophysiological process of various vascular disease such as atherosclerosis [2]. Pulse wave velocity assessed from a short vessel segment (local PWV) has been considered as an indicator of arterial stiffness. Local PWV is shown to correlate well with the mechanical characteristics of an artery over a wide physiological range [1, 3]. Researchers have demonstrated the potential of local PWV to evaluate blood pressure (BP) parameters locally from an artery without using the conventional bladder-type pressure cuff (cuffless technique) [4 – 6]. Simultaneously measured local PWV, arterial dimensions and local BP parameters are essential to accurately characterize and quantify the elastic behavior of central and peripheral arteries [1].

A standard approach for local PWV measurement relies on simultaneous acquisition of the propagating blood pulse waves from two distinct locations at a known separation distance (ΔX) within a small arterial segment. Time taken for the blood pulse wave to travel ΔX distance (pulse transit time [ΔT]), is obtained as the time delay between an identifiable point (fiducial point) on the proximal and distal pulse cycle pair. Following the fundamental distance-time equation, local PWV is then calculated as; Local PWV = $\Delta X/\Delta T$. Typically, only one measure of local PWV per cardiac cycle obtained from the reflection-free period is used for the quantitative characterization of an artery. However, local PWV is not a constant within a cardiac cycle, which otherwise varies proportionally to the instantaneous change in arterial pressure. Recently, we have proposed a calibration-free technique for cuffless BP measurement by tracking the variation in local PWV over the cardiac cycle [7]. This approach requires simultaneously measured local PWV and arterial dimensions from multiple points over the cardiac cycle. Such a methodology has the potential to revolutionize the conventional subject- and/or population-specific calibration-based cuffless BP evaluation techniques.

In this work, a method and system for direct measurement of local PWV variation over the cardiac cycle have been

presented. A novel dual-element magnetic plethysmograph (MPG) arterial compliance probe was developed. An application-specific dual channel blood pulse signal acquisition electronics hardware and fully automated pulse wave analysis algorithms were used for accurate measurement. An *in-vivo* validation study was conducted on 15 healthy volunteers to demonstrate the feasibility of local PWV evaluation from multiple fiducial points. Measurements were performed from the carotid artery using the dual-MPG probe in a beat-by-beat manner. Design of the arterial compliance probe, hardware implementation, and measurement algorithms are discussed in detail. *In-vivo* validation study results and observations are also summarized in the following sections, along with the limitations of the current study and recommended future research direction.

Pressure Dependency of Local PWV

The pulse wave initiated by blood ejection from the heart represents a propagating wave (in a fluid) through an elastic vessel. The velocity of traveling waves through an arterial segment (local PWV; henceforth denoted as ‘C’ in the equations/expressions) depends on physical characteristics of the vessel and blood density (ρ). A theoretical model describing the propagation of blood pulse wave in a cylindrical elastic vessel with an incremental modulus of elasticity E, inner radius R and wall thickness h was introduced by Moens and Korteweg [8], which can be expressed as in (1).

$$C = \sqrt{\frac{Eh}{2\rho R}} \quad (1)$$

The product of E and h is proportional to the ratio of tension acting on the vessel’s wall to the fractional amount of circumferential stretching, caused by the transmural pressure (P). Therefore, an increment in the lumen radius (dR) due to a small rise in pressure (dP) is given by the following expressions [9],

$$dR = dP \frac{R^2}{Eh} \\ \Rightarrow \frac{Eh}{2R} = A \frac{dP}{dA} \quad (2)$$

where dA is the instantaneous change in arterial cross-sectional area A. Substitution of (2) into (1) yields the well-known Bramwell-Hill equation of the form:

$$C = \sqrt{\frac{A}{\rho} \frac{dP}{dA}} \quad (3)$$

Further, an empirical relationship for incremental modulus of elasticity E developed by Hughes et al. through heuristic modeling is given by [10]:

$$E = E_0 e^{\alpha P}, \quad (4)$$

where E_0 is the theoretical zero-pressure modulus, and α is an arbitrary constant that depends on the vessel property (typically $0.016 \text{ mmHg}^{-1} \leq \alpha \leq 0.018 \text{ mmHg}^{-1}$). Thus, (1) and (4) can be combined to derive an empirical relationship between local PWV and arterial pressure as described in the following expression. Here, $\eta = \sqrt{E_0/\rho}$ is a constant that depends on the particular artery.

$$C = \eta \sqrt{\frac{h}{2R}} e^{\frac{\alpha}{2} P} \quad (5)$$

Both the equations (3) and (5) illustrate that the local PWV is a function of arterial dimensions and instantaneous pressure level. Equation (5) suggests that the local PWV increases exponentially over a cardiac cycle with respect to BP variation during the systolic phase.

Measurement System

Design of Dual-MPG Arterial Compliance Probe

A dual-MPG arterial compliance probe (fig. 1) was designed and developed for blood pulse detection from superficial arteries. The probe holder was machined with custom parts (face diameter = 30 mm) to fit two identical Hall-effect permanent magnet-based MPG transducers [5]. As shown in fig. 1, two disc-shaped permanent magnets (D032A – Amazing Magnets LLC, CA, USA; diameter = 3.175 mm) were fixed on the probe face with a center-to-center distance of 25 mm. When the probe is placed on the skin surface above an artery, the magnetic lines of force encompasses two distinct arterial sites within a small section. Fluctuations in this field caused by blood pulse waves propagating through the artery were detected using highly-sensitive Hall-effect ICs (SS49E T3 – SEC Electronics Inc., NY, USA). The Hall-effect ICs were fixed at a distance of 3.6 mm away from the center of respective magnets. Their output voltage was proportional to blood pulse signals at the measurement sites. The sensor separation distance and design features were optimized based on our initial experiments, such that the MPG probe could acquire dual pulse waveforms without any cross-coupling. Pulse propagation distance ΔX was taken as the center-to-center distance between proximal and distal MPG modules ($\Delta X = 25 \text{ mm}$).

Hardware and Software Architecture

Shielded three-core cables with a wire gauge of 28 AWG were used to interface the MPG transducers with the electronics hardware. A dedicated dual-channel analog front-end (AFE) was developed for the precise acquisition of proximal and distal blood pulse cycles. The inherent inter-channel delay between the AFE channels was minimized ($< 0.1 \text{ ms}$) using a custom electronic circuit design by avoiding capacitors in the principal signal path. Subtractor

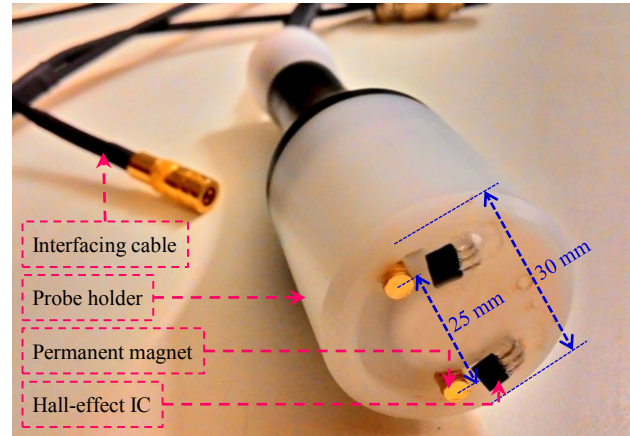


Figure 1: Dual-MPG arterial compliance probe

circuit with an instantaneous feedback of subtrahend [5] was used to remove static components from the acquired MPG signals (voltage $\approx 2.8 \text{ V}$, frequency $< 0.05 \text{ Hz}$). The extracted pulsatile components (in the order of millivolts) were amplified with an approximate gain of 40 dB, using a dual channel instrumentation amplifier (INA2126P – Texas Instruments Inc.). A commercially available simultaneously sampling data acquisition card (PXIe-6368 – National Instruments, TX, USA) was used to digitize the amplified MPG signals (sampling rate = 100 kS/s/ch).

Dual-channel MPG signal acquisition, post-processing, and pulse wave analysis were performed via a custom computer program developed using LabVIEW (Version 2014, National Instruments, TX, USA). MPG signals from both the channels were processed instantaneously in the digital domain. Initially, a 2nd order Butterworth low-pass digital filter with a cutoff frequency of 10 Hz was applied to smoothen the waveforms. Zero phase-shift filters were preferred to overcome phase difference between the unfiltered and the filtered signals. Any baseline drift caused by respiration or other artifacts were removed using a baseline wander elimination technique. Processed MPG pulse cycles were segregated with the same time interval from the pulse wave train using a cycle-cutting algorithm. Each proximal-distal cycle pairs were normalized between 0 and 1 to overcome any amplitude difference occurred during real-time acquisition.

Pulse Wave Analysis

Identification of multiple fiducial points within a pulse cycle is essential to assess local PWV variation over the cardiac cycle. Two characteristic identification points were defined near the foot and peak of the measured blood pulse cycles. These fiducial points were derived by applying a second-order differentiator to each pulse cycles. Fig. 2 exhibits an example blood pulse cycle and its second-derivative waveform (normalized to equal amplitude), illustrating the relative position of two critical points in the blood pulse cycle. The fiducial point near the waveform foot (Ψ_{Foot} ; resembles the systolic rising point) and the one near the systolic peak (Ψ_{Peak}) represent the

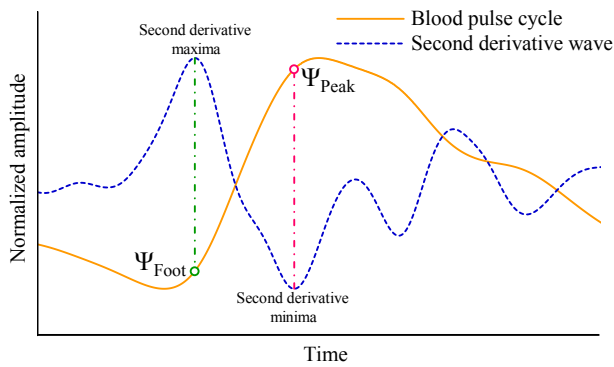


Figure 2: Fiducial points Ψ_{Foot} and Ψ_{Peak} defined in a blood pulse cycle from the second derivative wave

locations in pulse cycle corresponding to the maxima and minima of the second derivative waveform respectively. The time delay between Ψ_{Foot} of the proximal and distal pulse cycles was taken as the pulse transit time at diastolic BP level (ΔT_D), and a similar measure from Ψ_{Peak} represented pulse transit time at systolic BP level (ΔT_S). Local PWV was then evaluated from the systolic rising point and neighborhood of systolic peak using ΔX and corresponding transit time estimates, denoted as C_D and C_S respectively.

Validation Materials and Methods

An *in-vivo* study was conducted on 15 volunteers (age = 27 ± 4 years) to investigate the feasibility of the proposed method and system. The study objective and measurement protocol were explained to each volunteer, and written informed consent was obtained. They were requested to relax in sitting posture for 3 – 5 minutes before starting the measurement in order to stabilize BP and heartrate.

Once the anthropometric parameters were recorded, BP was measured from the left brachial artery with a clinical grade automatic BP monitor (SunTech 247 – SunTech Medical Inc. NC, USA). Local PWV values were then measured from the left carotid artery by placing the arterial compliance probe over the neck. The carotid artery was preferred since it is close to the skin surface, easily accessible and provides a straight vessel segment of sufficient length before the bifurcation. The operator adjusted the probe placement and orientation after locating the carotid pulse by palpation to acquire quality signals from both the proximal and distal MPG transducers. Signal acquisition and real-time local PWV evaluation were continued for 20 – 25 cardiac cycles from each volunteer.

Results and Discussion

Reliability of Carotid MPG Signal Acquisition

The developed prototype device was capable of detecting high-fidelity blood pulse signals from the carotid artery. Fig. 3 depicts a sample of simultaneously acquired proximal and distal MPG signals (after post-processing) from 25 mm distance apart. The peak-to-peak amplitude of the

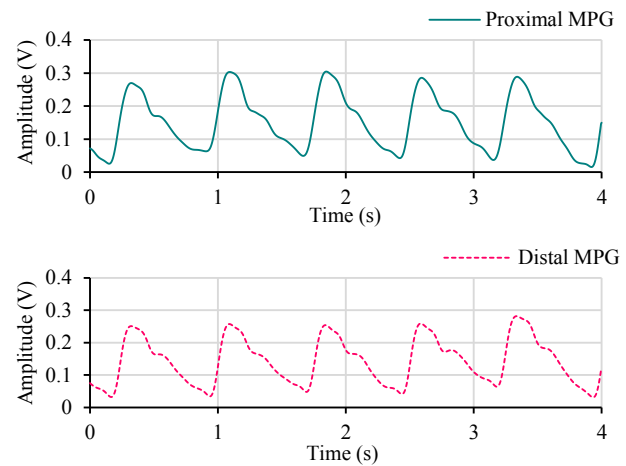


Figure 3: Simultaneously acquired proximal and distal MPG waveforms using arterial compliance probe

MPG signals was subjective, the typical range was between 1.5 mV_{PP} and 3.5 mV_{PP}. Spectral analysis of the acquired MPG signals revealed an approximate signal-to-noise ratio of 29 dB. It was sufficient for resolving pulse transit time estimates ΔT_D and ΔT_S (on the order of milliseconds) using the developed algorithms. However, degraded signal quality and/or an intense baseline drift caused by body movement yielded an error in critical point identification. Measurements obtained from such non-ideal cases were manually eliminated. In future, real-time signal quality indicators will be implemented in the measurement software to quantify the quality of acquired MPG signals. Such an automated instant feedback system could potentially guide the operators to archive more accurate and reliable measurements.

Variation in Local PWV Over the Cardiac Cycle

Carotid local PWV values were evaluated from both systolic rising point and neighborhood of systolic peak in a beat-by-beat manner. Fig. 4 presents continuously measured C_D and C_S from the left carotid artery of a particular volunteer (age = 28 years). Consistent with the theory, measured C_S values were higher than the corresponding C_D values, that was observed in continuous cardiac cycles from all recruited volunteers (tab. 1). The coefficient of variation (CoV) of C_S to C_D ratio evaluated from continuous cardiac cycles was less than 7%, indicating the reliability of measurement. Beat-to-beat variation in C_D and C_S measurement was between 4% to 7% and 6% to 9.5% respectively. Relatively high beat-to-beat variation observed in C_S measurement could be due to the wave reflection and confounding factors that influence Ψ_{Peak} locus and/or MPG waves from a small arterial segment. Further works are in progress to develop improved pulse wave analysis algorithm, and to optimize the probe design and sensing modality for accurate evaluation of C_D and C_S from various arterial sites.

Consistent with previous studies [4, 5], the absolute values of C_D were lower than the conventional carotid-femoral regional PWV estimates. Pearson's correlation

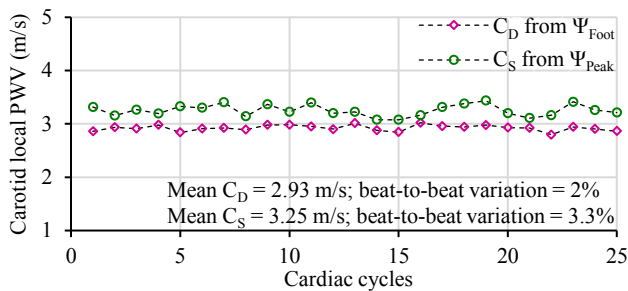


Figure 4: Carotid local PWV obtained from two distinct fiducial points within a cardiac cycle (C_D and C_S), illustrating measurement reliability and beat-to-beat variation

Table 1: Measurements Recorded from Volunteers

Volunt eer ID	Brachial BP (mmHg)		Local PWV (m/s)		Cs/Cp CoV
	Systolic	Diastolic	C_D	C_S	
22y/F	115	70	2.98	3.12	4.2%
25y/M	121	69	2.79	2.94	5.1%
28y/M	110	73	2.93	3.25	3.2%
26y/F	106	76	2.89	3.11	5.5%
27y/M	100	78	3.03	3.21	2.8%
29y/M	130	89	4.2	4.46	6.3%
33y/M	104	70	3.41	3.71	2.9%
30y/M	120	75	3.4	3.63	5.0%
25y/M	117	60	2.78	2.96	4.3%
28y/F	110	79	3.24	3.46	3.8%
31y/F	112	84	3.28	3.61	4.1%
27y/F	103	71	2.72	2.83	6.6%
36y/M	138	77	3.81	4.08	3.3%
25y/F	98	72	2.4	2.61	6.7%
21y/M	101	66	2.04	2.24	3.6%

coefficients (r) obtained from the regression analysis of BP parameters versus mean C_D and C_S pooled over all the volunteers were statistically significant ($p < 0.0001$). The r -value was 0.71 and 0.68 for diastolic BP versus C_D , and systolic BP versus C_S respectively. Results of this *in-vivo* study demonstrated the feasibility of dual-MPG arterial compliance probe to acquire local PWV variation over the cardiac cycle. This probe can be potentially used in cuffless BP monitoring techniques that utilize variations in local PWV to realize a calibration-free approach [7].

Study Limitations and Future Research Direction

A major limitation of the present *in-vivo* study concerns the small sample size of young, healthy volunteers. However, the current study was conducted to demonstrate the practical feasibility of a novel technique. An extensive validation study in a large population with pathophysiological sub-populations is needed to confirm the validity of proposed method and system over a wide physiological range. Variation in local PWV obtained by the proposed technique did not compare with that obtained by a reference method since commercial devices which can measure carotid local PWV from multiple points over the cardiac cycle are not available at present. Further research is underway to assess the variation in local PWV over the cardiac cycle via single-site measurement techniques.

Simultaneously acquired arterial dimensions and pressure wave can be utilized to realize such systems with the help of Bramwell-Hill equation.

Conclusions

The proposed arterial compliance probe and associated measurement system was experimentally validated on 15 human volunteers and demonstrated the expected functionality. Blood pulse signals were continuously acquired from the carotid artery using dual MPG transducers positioned 25 mm apart. Carotid local PWV was evaluated using the proximal and distal cycles, from two distinct fiducial points within a cardiac cycle in a beat-by-beat manner. Consistent with the theoretical models, local PWV obtained from the neighborhood of the systolic peak was higher than that obtained from the systolic rising point; illustrating the variation in local PWV over the cardiac cycle. This was consistently observed in all recruited volunteers with high reproducibility. An extensive clinical study in a large population is required to further validate the proposed approach. The potential application of accurate measurement of variation in local PWV over the cardiac cycle has been established in calibration-free BP evaluation techniques. Hence, the proposed arterial compliance probe could provide an opportunity for cuffless, calibration-free evaluation of BP parameters from superficial arteries in a beat-by-beat manner.

References

- [1] G. G. Raymond and M. B. Marc. Terminology for describing the elastic behavior of arteries. *Hypertension*, 41(6):1180–1182, 2003.
- [2] R. S. Reneman et al. Non-invasive ultrasound in arterial wall dynamics in humans: what have we learned and what remains to be solved. *Eur Heart J*, 26(10):960–966, 2005.
- [3] T. Pereira et al. Novel methods for pulse wave velocity measurement. *J Med Biol Eng*, 35(5):555–565, 2015.
- [4] P. M. Nabeel et al. Single-source PPG-based local pulse wave velocity measurement: a potential cuffless blood pressure estimation technique. *Physiol Meas*, 38(12):2122–2140, 2017.
- [5] P. M. Nabeel et al. A magnetic plethysmograph probe for local pulse wave velocity measurement. *IEEE Trans Biomed Circuits Syst*, 11(5):1065–1076, 2017.
- [6] J. Vappou et al. Non-invasive measurement of local pulse pressure by pulse wave-based ultrasound manometry (PWUM). *Physiol Meas*, 32(10):1653–1662, 2011.
- [7] J. Joseph et al. Method and system for cuff-less blood pressure (BP) measurement of a subject. US Patent US20170156706 A1, 2017.
- [8] W. W. Nichols and M. F. O'Rourke. *McDonald's Blood flow in arteries: theoretical, experimental, and clinical principles*. 4th ed., Hodder Arnold Publication, 1998.
- [9] J. C. Bramwell and A. V. Hill. The velocity of the pulse wave in man. *Proc. Roy. Soc. Lond. Ser. B*, 93(652):298–306, 1922.
- [10] D. J. Hughes et al. Measurements of Young's modulus of elasticity of the canine aorta with ultrasound. *Ultrason Imag*, 1(4):356–367, 1979.

Hemodynamic Interventions for Inducing Blood Pressure Variation in Laboratory Settings

Nabeel P M¹, Surya Venkatramanan², Jayaraj Joseph², Mohanasankar Sivaprakasam^{1,2}

¹Department of Electrical Engineering, Indian Institute of Technology Madras, Chennai, India

²Healthcare Technology Innovation Centre, Indian Institute of Technology Madras, Chennai, India

Contact: nabeelnpm@gmail.com

Introduction

Arterial blood pressure (BP) parameters are key hemodynamic indices often used for screening and diagnosis of various pathophysiological conditions. Brachial artery BP measurement using a bladder-type pressure cuff and sphygmomanometer (auscultatory or oscillometric technique) is a routine part of clinical assessments. Over the past few years, the interest in methods that allow non-invasive, cuffless evaluation of BP parameters has increased to overcome the fundamental limitations of cuff-based techniques [1]. Cuffless techniques rely on exploring the relationship between BP and BP-dependent non-invasively measurable physiological parameters. Such theoretical or heuristic mathematical models generally require subject- and/or population-specific calibration procedure to quantitatively convert the acquired physiological parameters into pressure. Pulse transit time estimates, arterial vessel characteristics, and various hemodynamic indices are typically utilized to implement cuffless BP evaluation techniques [2]; these parameters are subject specific. Hence, a calibration curve and/or BP prediction model that is tailored to each subject would be optimal for accurate measurement [3]. Further, these calibration curves/models would have to be updated at regular intervals for accurate and reliable BP evaluation [2].

In order to develop subject-specific calibration curves or data-driven prediction models, the desired input physiological parameters should be recorded over a wide range of BP values from the subject. For this, resting BP level should alter via suitable BP perturbing interventions. Calibration curves or prediction models obtained through data recorded from a single intervention may not be effective for accurate BP evaluation [2]. Subject-specific data obtained from multiple interventions that perturb BP through different physiologic mechanisms could potentially provide reliable prediction models. Hemodynamic interventions such as drug-induced methods, anesthesia induction, and intensive care unit (ICU) therapies are typically followed to produce major BP changes over a wide physiological range [4]. However, these approaches are technically demanding, highly invasive, require well-trained physicians with clinical and/or research experience, and limited to hospitalized subjects. Therefore, subject-specific calibration curve/model construction and recalibration via invasive interventions cannot be adopted to realize cuffless BP techniques for wearable devices and routine screening applications. Practically feasible non-

invasive interventions are needed to perturb BP parameters during the design, validation and recalibration phases of cuffless BP devices.

In this work, we evaluated the variation in brachial BP parameters during multiple hemodynamic interventions that change the BP level through different physiological mechanisms. Five non-invasive interventions namely; (i) cold pressor test, (ii) treadmill-running exercise, (iii) mental arithmetic, (iv) leg-raise test, and (v) sustained hand-grip test were preferred for the validation study. These BP perturbing interventions could be safely performed in laboratory/non-specialist settings without the assistance from a physician or a trained investigator. Further, they could mimic various daily life activities such as experiencing cold weather conditions, brisk walk or performing strenuous exercise, stressful situations et cetera. An *in-vivo* study was conducted on randomly recruited normotensive subjects in order to characterize the BP altering strategies of aforesaid interventions. Measurement protocol of the performed study, BP perturbing procedure, recommended experimental conditions, *in-vivo* study results and observations are discussed in the following sections.

Materials and Methods






Subject Selection

Fifteen normotensive subjects ranged in age from 22 to 34 years comprising of males and females (body mass index = 22 – 29 kg/m²) were recruited for the present *in-vivo* study. The study objectives and measurement protocol were explained to each participant and their written informed consent was obtained. This study conforms to the principles outlined in the Declaration of Helsinki. Before data collection, participants were requested to relax for 5 – 10 min to reduce their anxiety and to bring the BP parameters and heartrate to the normal level.

Study Protocol

The *in-vivo* validation study was designed by including five hemodynamic interventions listed in tab .1. Systolic BP (SBP), diastolic BP (DBP), mean arterial pressure (MAP) and heartrate were repeatedly measured from the brachial artery under (i) physically relaxed condition, (ii) during an intervention, and (iii) post-intervention recovery period. Measurements were performed using a clinical grade automatic BP monitor (SunTech[®] 247TM – SunTech Medical Inc. NC, USA; resolution = 1 mmHg) with a bladder-type pressure cuff. During the study, resting BP

Table 1: Hemodynamic Interventions for Altering BP Parameters

Intervention	Protocol	Observations and comments
<p>Cold pressor test</p> 	<p>Immerse both the hands into an ice water container for 2 – 4 min. Maintain the ice water temperature between 3 – 5°C.</p>	<ul style="list-style-type: none"> • Minimum 2 min intervention required for moderate perturbation in BP • Trivial body movement/motion artifacts • Sensitive towards individual pain threshold and pain tolerance
<p>Treadmill-running exercise</p> 	<p>Run on a treadmill for 7 – 10 min. Start with a low speed of 3 km/h, and increase the speed at a steady rate (maximum up to 10 km/h).</p>	<ul style="list-style-type: none"> • Significant variation in SBP and heartrate • Maintain heartrate < 85% of (220 – Age) • Prone to body movement/motion artifacts during the intervention period • High breathing artifacts during post-intervention recovery period
<p>Mental arithmetic</p> 	<p>Perform serial subtraction of a two-digit number from a four-digit number quickly and repetitively for 4 – 5 min.</p>	<ul style="list-style-type: none"> • Recreation of real-life stressful situation • Trivial body movement/motion artifacts • Variations in BP may not be observed when the participant is an experienced public speaker or intellectually sound in mathematics
<p>Leg-raise test</p> 	<p>By adopting the supine posture, raise and hold one leg without any support, for 2 – 3 min.</p>	<ul style="list-style-type: none"> • Moderate variation in BP parameters and heartrate • Post-test BP recovery time < 1 min • Minimal body movement/motion artifacts • Not recommend in patients with sciatica
<p>Sustained handgrip test</p> 	<p>Hold and clench handles of the spring-type handgrip in both the hands by putting in maximum effort for a sustained time until fatigued.</p>	<ul style="list-style-type: none"> • Substantial variation in BP parameters and heartrate • Minimal body movement/motion artifacts • Strength deficit of the muscles associated with variation BP level

and heartrate (baseline values) of each subject were measured for 2 – 3 min. After the baseline measurement, the participants underwent a BP perturbing intervention task (protocols are summarized in the tab. 1), followed by a recovery phase, in which they rested until BP and heartrate returned to the baseline value or remained in steady level. It was preferred to conduct only one intervention task per day for an individual subject. This helped to investigate the physiological response and cardiovascular reactivity of each intervention independently.

Results and Discussion

Intervention Characteristic Curve for BP Variation

For each subject, the recorded brachial SBP, DBP, MAP, and heartrate were analyzed and compared in order to characterize the BP altering strategies of preferred interventions. The average time interval between two consecutive BP measurement was approximately 42 s, which is the time taken by the BP monitor to inflate, deflate, and report the measured values. The obtained discrete readings of each BP parameter was interpolated onto their successive readings to produce continuous curves showing the locus of instantaneous variation in BP parameters.

This interpolation allowed characterization of BP variation due to an external intervention.

Fig. 1 depicts typical intervention characteristic curve illustrating variation in BP level during the course of study, under increasing BP conditions. This projected curve was obtained by generalizing data recorded during the present study over all the subjects. However, an intervention characteristic curve for each BP parameter is subject-specific. As shown in fig. 1, the fiducial parameters of BP intervention characteristic curve were defined with re-

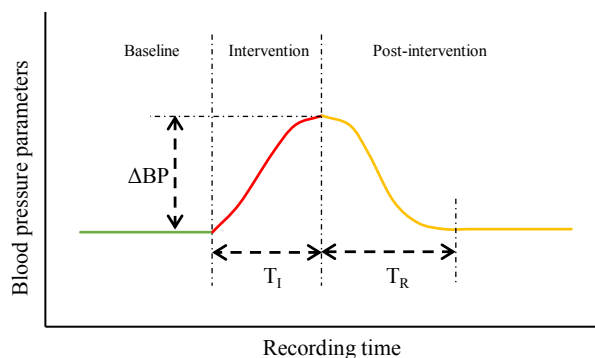


Figure 1: Typical BP intervention characteristic curve

spect to initial baseline and post-intervention measurements. The total time taken to perform an intervention task as per the protocol (tab. 1) is denoted as the intervention period (T_I). The post-intervention recovery period (T_R) is defined as the time taken to regain initial baseline values or a steady BP level after finishing an intervention task. The maximum increment yielded in the BP level from its baseline value is expressed as an absolute change (ΔBP), this quantitative metric for SBP, DBP and MAP are ΔP_S , ΔP_D , and ΔP_M respectively. Similarly, the maximum variation in heartrate (with respect to baseline heartrate) during the intervention task is denoted as ΔHR .

The proposed fiducial parameters were evaluated separately for all five interventions to investigate their individual effect. Representative characteristic curves (obtained from a subject with age = 17 years and body mass index = 24 kg/m²) demonstrating the variations in BP parameters and heartrate during all five interventions has been presented in fig. 2. It may be noted that the treadmill-running exercise is subject to significant body movement and motion artifacts. As a consequence, measurements recorded while performing the treadmill-running task were not reliable, and hence those data points were removed from its characteristic curves.

Hemodynamic Variation due to External Intervention

All five interventions included in this study are known to increase BP parameters, however, the induced variations and post-intervention recovery are caused by the different physiological phenomenon. The proposed fiducial parameters defining hemodynamic variations due to external interventions have been summarized in fig. 3 using box-and-whisker diagrams pooled over all the subjects. The absolute values of T_I were limited by pre-defined study protocol as per the nature of interventions, however, the

absolute T_R values depended on physiological response and cardiovascular reactivity to an intervention task. Absolute T_R for each BP parameter was comparable (< 5% variation), and hence an average T_R has been depicted in fig. 3. Due to elaborated T_I and severity of the treadmill-running task, its mean T_R was higher (4.2 min) than the corresponding metrics offered by other intervention tasks. Both the leg-raise and sustained handgrip tests (means of $T_R = 0.6$ min and 0.9 min respectively) yielded rapid post-intervention recovery from the elevated BP level.

It may be observed from the box-and-whisker diagrams that the cold pressor test yielded a moderate increment in all BP parameters (mean values of $\Delta P_S = 22.5$ mmHg, $\Delta P_D = 16.7$ mmHg and $\Delta P_M = 18$ mmHg). These BP variations are mediated by a sudden increase in the peripheral vascular resistance due to vasoconstriction, the underlying mechanism being the autonomic neural pathways acting via sympathetic nervous system [5]. Cardiac output and heartrate typically increase during aerobic exercise like running on a treadmill, which leads to a significant increment in SBP (mean values of $\Delta P_S = 37.6$ mmHg and $\Delta HR = 67.2$ bpm) with a moderate variation in DBP level (mean $\Delta P_D = 14.4$ mmHg) during the post-exercise recovery period. However, in physical tasks such as sustained handgrip test, the static contraction of muscles against fixed mechanical spring load causes a marked increase in all the BP parameters with a relatively small heartrate variability [6]. The presented study also demonstrated substantial variation in the BP parameters (means values of $\Delta P_S = 28.5$ mmHg, $\Delta P_D = 26.7$ mmHg and $\Delta P_M = 26.5$ mmHg) with a mean heartrate increment of 17.6 bpm during the sustained handgrip test.

Consistent with the physiological theory, a moderate increment in SBP, DBP, and MAP was observed during the

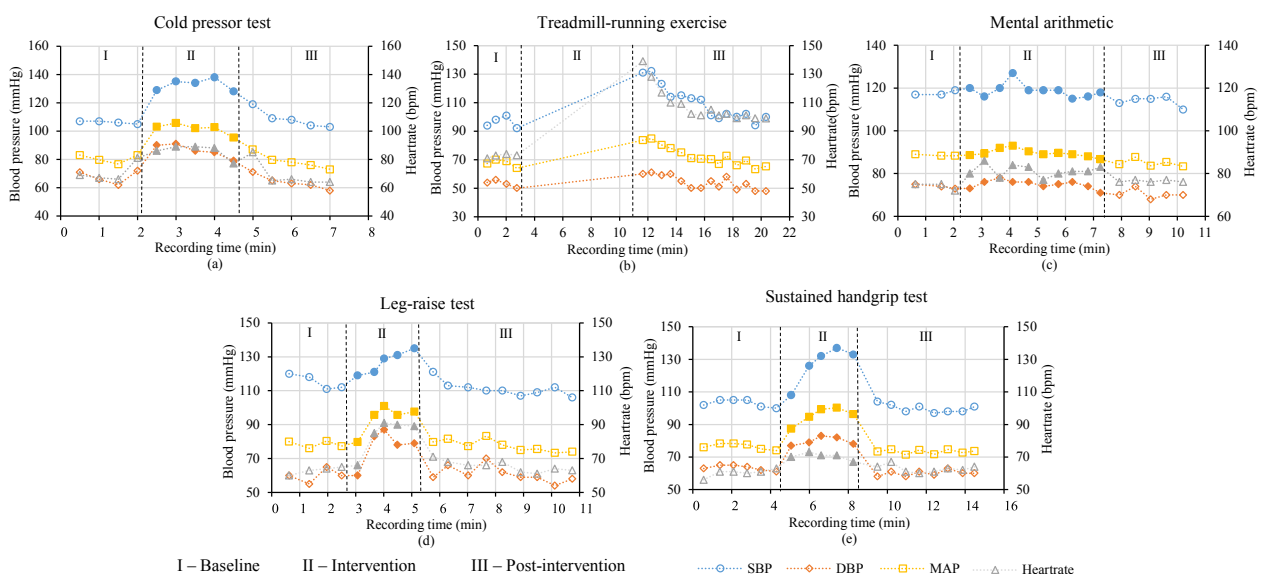


Figure 2: Subject-specific intervention characteristic curves obtained from a particular subject, illustrating the variation in SBP, DBP, MAP and heartrate during (a) cold pressor test, (b) treadmill-running exercise, (c) mental arithmetic, (d) leg-raise test, and (e) sustained handgrip test

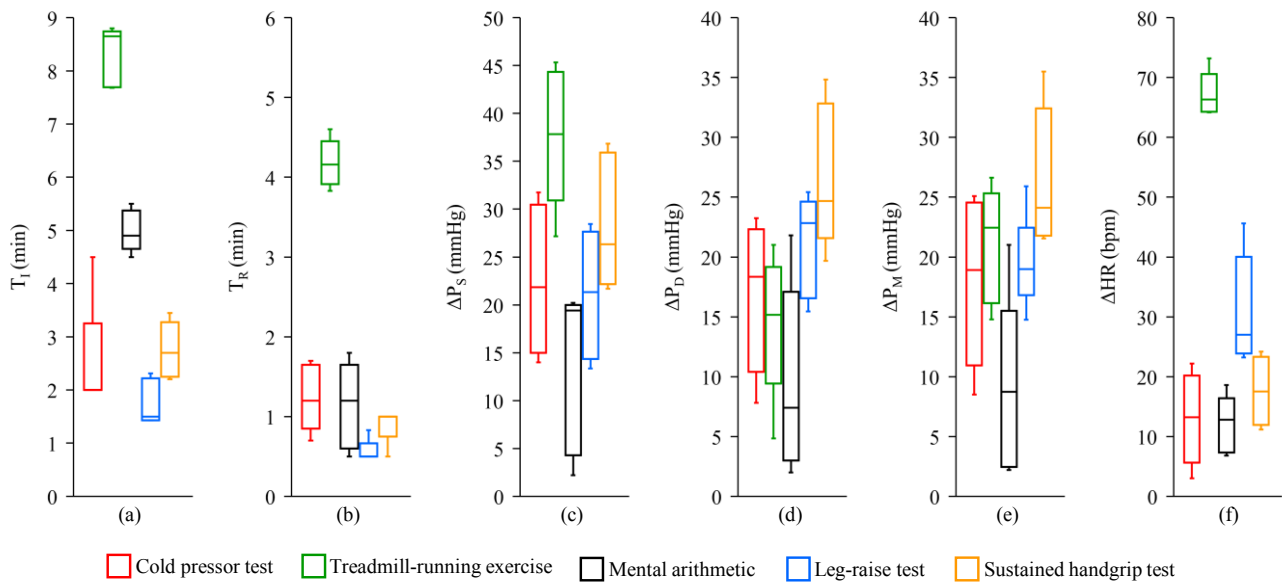


Figure 3: Box-and-whisker plots illustrating the measured fiducial parameters (a) T_I , (b) T_R , (c) ΔP_S , (d) ΔP_D , (e) ΔP_M , and (f) ΔHR pooled over all the subjects

active leg-raise test (mean values of $\Delta P_S = 21.1$ mmHg, $\Delta P_D = 21$ mmHg and $\Delta P_M = 19.5$ mmHg). These variations are induced when a subject is performing a voluntary leg-raise the lowered perfusion pressure to the sustained contracting leg muscles is being compensated with an increase in cardiac output and BP, acting via the central pressor response [7]. Hemodynamic variations observed during the mental arithmetic test were idiosyncratic and prone to psychological reactions. Short-term changes in BP parameters were observed for the recruited subjects during the mental arithmetic test due to increase in sympathetic activity and dumping of baroreflex. Mean values of ΔP_S , ΔP_D , and ΔP_M obtained from the mental arithmetic test were 13.6 mmHg, 9.5 mmHg and 8.9 mmHg respectively. Heart rate variations were also not prominent (mean $\Delta HR = 12$ bpm) during the mental arithmetic test in the recruited normotensive subjects.

Conclusions

This study demonstrated five hemodynamic interventions that perturb resting BP level in a safe and controlled manner. During the study, the BP parameters were found to vary at different levels in accordance with the physiological response, which mimics daily life activities of an individual. For each subject, brachial SBP, DBP, MAP, and heart rate were measured from three phases: baseline, during the intervention and post-intervention recovery period. BP altering strategies of the preferred interventions were evaluated using the proposed BP intervention characteristic curve and fiducial parameters. The treadmill-running exercise found to induce significant variations in SBP and heart rate. However, the measurements were susceptible to motion and breathing artifacts. A moderate variation in all BP parameters was observed during the cold pressor test, where no physical movements were in-

involved. Therefore, the cold pressor test may be a recommendable method for acquiring physiological signals under varying BP conditions with minimum error due to motion and breathing artifacts. Further validation study in a large population is in progress, in which BP and BP-dependent physiological parameters are recorded in a beat-by-beat manner during multiple interventions. Data recorded from such extensive studies can be used for developing BP prediction models through data-driven methods such as machine learning. Such models can be potentially used in wearable devices and cuffless 24-hour ambulatory BP monitors.

References

- [1] X. -R. Ding et al. Continuous blood pressure measurement from invasive to unobtrusive: celebration of 200th birth anniversary of Carl Ludwig. *IEEE J Biomed Health Inform*, 20(6):1455–465, 2016.
- [2] R. Mukkamala et al. Toward ubiquitous blood pressure monitoring via pulse transit time: theory and practice. *IEEE Trans Biomed Eng*, 62(8):1879–1901, 2015.
- [3] P. M. Nabeel et al. Single-source PPG-based local pulse wave velocity measurement: a potential cuffless blood pressure estimation technique. *Physiol Meas*, 38(12):2122–2140, 2017.
- [4] C. C. Young et al. Clinical evaluation of continuous noninvasive blood pressure monitoring: accuracy and tracking capabilities. *J Clin Monit*, 11(4):245–252, 1995.
- [5] M. J. Joyner et al. Sympathetic nervous system and blood pressure in humans: individualized patterns of regulation and their implications. *Hypertension*, 56(1):10–16, 2010.
- [6] R. Garg et al. The isometric handgrip exercise as a test for unmasking hypertension in the offsprings of hypertensive parents. *J Clin Diagn Res*, 7(6):996–999, 2013.
- [7] B. L. Luu et al. Blood pressure and the contractility of a human leg muscle. *J Physiol*, 591(21):5401–5412, 2013.

Non-Invasive Assessment of Arterial Incremental Elastic Modulus Variations within a Cardiac Cycle

Raj Kiran V¹, Nabeel P M¹, Jayaraj Joseph², Mohanasankar Sivaprakasam^{1,2}

¹Department of Electrical Engineering, Indian Institute of Technology Madras, Chennai, India

²Healthcare Technology Innovation Centre, Indian Institute of Technology Madras, Chennai, India

Contact: ee15d020@ee.iitm.ac.in

Introduction

Non-invasive assessment of arterial elastic properties is of high interest in cardiovascular research and screening of the vascular health. Over the last decades, a great emphasis has been placed on quantifying arterial stiffness, and its pathological significance is asserted in various epidemiological studies [1]. Typically used arterial elastic indices such as distensibility coefficient (DC), compliance coefficient (CC), and Peterson modulus (E_p) provide the measure of the functional stiffness of the artery. On the other hand incremental Young's elastic modulus (E_{inc}) quantifies material or intrinsic stiffness and hence properly characterizes the non-linear elastic behavior of the artery [2]. It has been recently demonstrated that the standard deviation in E_{inc} is an independent biomarker of coronary heart diseases [3]. The absolute value of E_{inc} varies within a cardiac cycle during diastolic to systolic phase. Accurate evaluation of these variations can be potentially used to quantify the degree of non-linearity in the elastic properties of an arterial section. Further, these variations can form a basis for tracking the variation in pulse wave velocity over the cardiac cycle [4], and cuffless evaluation of arterial blood pressure (BP) parameters without any calibration procedure [5].

Accurate evaluation of E_{inc} of a particular artery requires a local evaluation of arterial dimensions (diameter, wall thickness, distension) and transmural pressure simultaneously. High fidelity pressure and diameter waveforms are a mandate to efficiently track the variation of the E_{inc} over a cardiac cycle. State of the art techniques use B-mode or M-mode ultrasound modalities for estimation of arterial wall thickness and diameter waveforms [6, 7]. Local pressure waveforms required for the evaluation of E_{inc} are typically obtained using applanation tonometric transducers. However, for simultaneous acquisition of diameter and pressure waveforms using such modalities are prone to practical limitations due to the design form factor of the probes [8]. Further, the waveforms can be subject to inherent phase delays due to (i) the acquisition of the desired waveforms from two distinct arterial sites separated by a significant distance, and (ii) the lack of time synchronization between the acquisition modules of pressure and diameter waveforms. The devices realized using the aforementioned technique have not gained widespread applicability for large population screening due to the necessity of skilled operator and portability issues.

In this work, we propose a non-invasive measurement system for the evaluation of E_{inc} and its variation over a cardiac cycle in a beat-by-beat manner. The system uses a novel custom-designed probe which includes a single element ultrasound transducer and a tonometer for simultaneous measurement of arterial wall thickness, diameter, and pressure waveforms. The probe design was optimized to ensure that the measurements were localized over a small arterial segment, resembling single-site measurement. Online evaluation of the desired arterial dimensions without an ultrasound image was performed using our clinically validated ARTSENS[®] technology [9, 10]. The developed prototype system was experimentally validated by an *in-vivo* study of 10 subjects. The systolic and diastolic E_{inc} were evaluated from the left common carotid artery (LCCA). The proposed measurement system architecture, validation study protocol, results, and observations are discussed in the following sections.

Principle of E_{inc} Evaluation

The circumferential stress (σ) of an elastic artery with wall thickness (h) is developed due to the tension (T) acting on the arterial walls against the internal distending pressure (P), is given as in (1).

$$\sigma = \frac{T}{h} \quad (1)$$

Where, T is related to end-diastolic diameter (D_d) according to the Laplace law by considering thin wall assumption ($D_d \gg h$), which can be expressed as in (2).

$$T = \frac{P D_d}{2} \quad (2)$$

Using (1) and (2) the incremental stress ($d\sigma$) along the circumference due to a small increment in pressure (dP) can be obtained as follows;

$$d\sigma = \frac{dP D_d}{2h} \quad (3)$$

The resultant incremental circumferential strain ($d\epsilon$) due to the stress on the arterial walls can be expressed in terms of change in luminal diameter (dD) and D_d as in (4).

$$d\epsilon = \frac{dD}{D_d} \quad (4)$$

Further, E_{inc} can be evaluated as the ratio of $d\sigma$ and $d\epsilon$ and can be obtained by dividing (3) and (4), which can be expressed as is given in (5).

$$E_{inc} = \frac{D_d^2 dP}{2h dD} \quad (5)$$

Measurement System

Ultrasound-Pressure Probe Design

An application specific probe was designed and developed to facilitate simultaneous measurement of arterial dimensions and pressure from a small arterial section. The probe incorporates a single element ultrasound transducer (diameter = 5 mm, center-frequency 5 MHz, spatial half angle $< 1.3^\circ$) for tracking the dynamics of arterial dimensions, and a commercially available tonometer (SPT-301 – Millar Instrument) for capturing arterial pressure waveforms. A custom probe enclosure (probe holder) was 3D printed to integrate the ultrasound and tonometer transducers. Design schematic and assembly of the proposed ultrasound-pressure probe has been depicted in fig. 1. The separation between the transducers was kept minimal (2 mm) to perform a reliable single-site measurement.

Data Acquisition Hardware

The design architecture of the signal acquisition hardware is illustrated in fig. 2. The ultrasound transducer was interfaced to a dedicated analog front end (AFE) of the ARTSENS[®] device. The AFE consists of high-voltage pulse generation circuitry and a pulser-receiver module for operating the ultrasound transducer in pulse-echo mode. A high-speed digital input-output card (NI PXIe 6556 – National Instruments) was employed for controlling the pulser-receiver module. The ultrasound transducer was insonated to obtain an A-scan of 40 mm depth. The received A-scan radio-frequency (RF) frames were pre-conditioned using a 40 dB dual stage amplifier, and then digitized using a high-speed digitizer (NI PXI 5154 – National Instruments, sampling rate = 50 MHz). The hardware was configured to achieve a high frame rate of 1 kHz. The tonometer used for acquiring pressure signal was interfaced to ADInstruments' PowerLab and BridgeAmp, controlled using LabChart software. The pre-processed pressure waveform from the BridgeAmp was

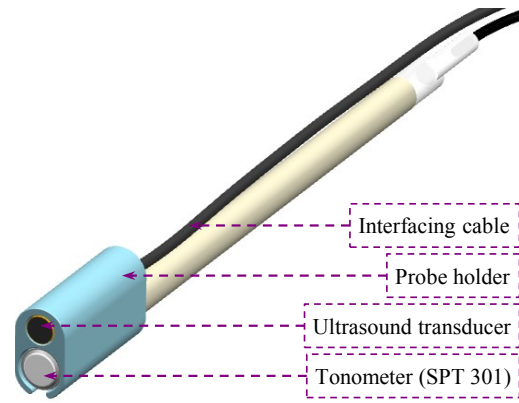


Figure 1: Proposed ultrasound-tonometer probe assembly digitized using a data acquisition card (DAQ; NI PXIe 6368 – National Instruments) at a sampling rate of 1 kHz. A digital trigger pulse (1 kHz pulse repetition rate) generated by NI PXIe 6556 was used for the synchronized acquisition of RF frames and pressure waveform from the independent hardware modules.

Signal Processing and Measurement Software

Simultaneously acquired pressure signal and RF echo frames were processed in the digital domain using dedicated semi-automated software developed on National Instruments' LabVIEW platform. The measurement software architecture has been depicted in fig. 2. The acquired RF frames were processed using intelligent algorithms of the ARTSENS[®] technology. The arterial proximal and distal walls were automatically identified and the wall motion was tracked using a correlation based technique [9]. High fidelity diameter waveform was captured using the software, and the end-diastolic diameter (D_d) and distension (ΔD) were obtained over continuous cardiac cycles. For reliable evaluation of h , distal wall echo was chosen and the measurement was done between the leading edges of the intima and adventitia. The discontinuities in the linearity of the unwrapped phase of the dis-

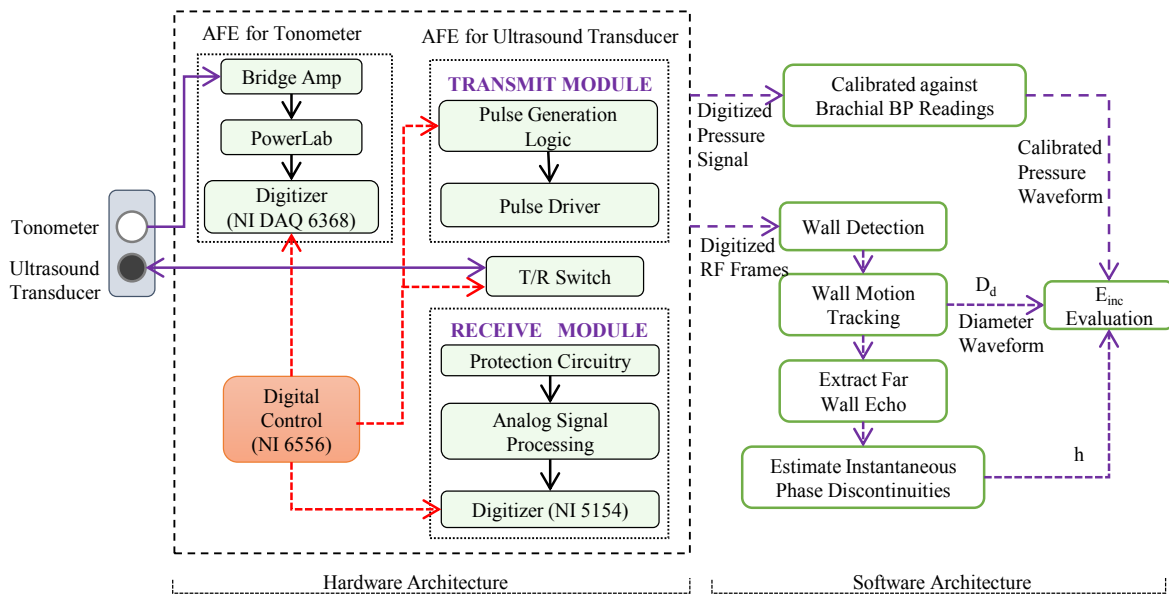


Figure 2: Schematic diagram illustrating the hardware and software architecture of the proposed measurement system

tal wall echo were used to find the leading edges of the intima and adventitia complex and estimate h [11]. The acquired raw tonometer pressure signal was filtered with a low-pass filter of 15 Hz cutoff frequency to remove high-frequency noise. The processed pressure signal was then calibrated against the measured brachial BP, considering end diastolic and mean arterial pressure to be approximately constant throughout the arterial tree when the subject is in supine posture.

For each cardiac cycle, the pressure-diameter loop (PD loop) was obtained by plotting diameter cycle along the abscissa and pressure cycle along the ordinate. For the investigation of variation in E_{inc} two fiducial points were defined; (i) second derivative maxima of the pressure cycle, a point (Ψ_d) at the neighborhood of end-diastolic point, and (ii) second derivative minima of the pressure cycle, a point (Ψ_s) at the neighborhood of systolic peak. Slope of the PD loop at these two points ($(dP/dD)|_{\Psi_d}$ and $(dP/dD)|_{\Psi_s}$ along with D_d and h were used for the estimation of E_{inc} at the Ψ_d and Ψ_s (E_{Ψ_d} , E_{Ψ_s} respectively) with the help of (5).

In-vivo Validation Study

Subject Selection for In-Vivo Validation

An *in-vivo* study was conducted on 10 healthy subjects to validate the functionality of the proposed ultrasound-pressure probe and the associated measurement system. The subjects recruited for the study were within 20 to 30 years of age (mean age = 25.6 ± 2.6 years).

Study Protocol

A written informed consent was obtained from the recruited subjects after briefing them the study objectives and the measurement protocol. Anthropometric measurements were performed and the subject was asked to relax for 5 minutes. The measurement of brachial BP and E_{inc} from the LCCA were performed by a single operator with subjects in supine posture. Clinical grade automatic BP monitor (SunTech® 247™ – SunTech Medical) was used to record the brachial BP parameters. The ultrasound-pressure probe was then placed on the left side of the neck, 2 cm below the carotid bulb to target the carotid artery. The probe was oriented to achieve good quality RF frames (with two strong echoes from the proximal and distal wall) and high fidelity pressure waveform. The probe was held steady and the signals were recorded continuously for a sufficient number of cardiac cycles.

Results and Discussion

Reliability of Continuous Signal Acquisition

The ultrasound-pressure probe and the prototype system developed for the evaluation of E_{inc} variation over the cardiac cycle demonstrated the expected functionality. The system could efficiently capture diameter and pressure variations over continuous cardiac cycles. A cycle of

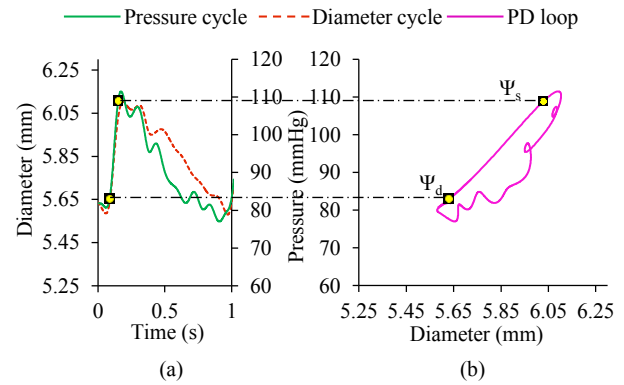


Figure 3: (a) A sample of simultaneously acquired pressure and diameter cycle from the LCCA, (b) Illustrating the construction of PD loop, the defined fiducial points are marked on the loop

Table 1: D_d , h , E_{Ψ_s} , and E_{Ψ_d} measured from the subjects

Subject ID	Age	D_d (mm)	h (mm)	E_{Ψ_s} (kPa)	E_{Ψ_d} (kPa)
P01	27	5.29 ± 0.08	0.72 ± 0.01	297.56 ± 5.17	167.58 ± 2.98
P02	24	5.76 ± 0.15	0.59 ± 0.03	372.50 ± 15.01	266.76 ± 11.80
P03	22	5.60 ± 0.09	0.53 ± 0.03	260.06 ± 13.9	179.80 ± 9.90
P04	27	6.07 ± 0.17	0.65 ± 0.02	255.43 ± 8.76	202.07 ± 7.60
P05	26	5.08 ± 0.16	0.55 ± 0.02	185.59 ± 7.12	133.62 ± 3.52
P06	28	5.49 ± 0.05	0.61 ± 0.03	158.45 ± 8.55	123.39 ± 6.43
P07	29	4.29 ± 0.08	0.37 ± 0.02	188.52 ± 6.24	143.79 ± 7.85
P08	22	6.01 ± 0.19	0.70 ± 0.01	440.92 ± 20.34	373.67 ± 16.33
P09	23	5.44 ± 0.17	0.46 ± 0.02	174.54 ± 11.51	156.29 ± 9.06
P10	28	5.52 ± 0.08	0.62 ± 0.04	150.76 ± 9.38	119.23 ± 6.76

both the diameter and pressure waveform obtained from a particular subject have been shown in fig. 3(a). It may be noted that the pressure and diameter waveforms follow a similar trend and are clearly correlated. Similar quality signals were captured from all other subjects. The temporal resolution of the pressure and diameter variations was 1 ms, enabling construction of high-resolution cycle-to-cycle PD loops. A PD loop obtained from the diameter and pressure cycle shown in fig. 3(a), is illustrated in fig. 3(b), and the fiducial points Ψ_s and Ψ_d are marked on it. It was observed that the slope of all the PD loops at Ψ_s is steeper than the slope at the Ψ_d , and increases nonlinearly from fiducial point Ψ_d to fiducial point Ψ_s exhibiting a non-linear stress strain relationship. The quality of the acquired signals and the PD loops were sufficient for reliable calculation of E_{Ψ_s} , and E_{Ψ_d} .

Variation of E_{inc} over a Cardiac Cycle

The measurements of D_d , h , E_{Ψ_s} , and E_{Ψ_d} were obtained from the subjects in a beat-by-beat manner. The beat-to-beat estimates of these parameters for a particular subject have been shown in fig. 4 (a) – (c). The measurement repeatability was evaluated by calculating the beat-to-beat variation – standard deviation (SD) to mean ratio of a finite number of cycles, expressed in percentage. Beat-to-beat variation observed for D_d , h , E_{Ψ_s} , and E_{Ψ_d} were less than 4%, 7.5%, 7%, and 7% respectively, indicating the reliability of measurements. E_{Ψ_s} , and E_{Ψ_d} obtained from

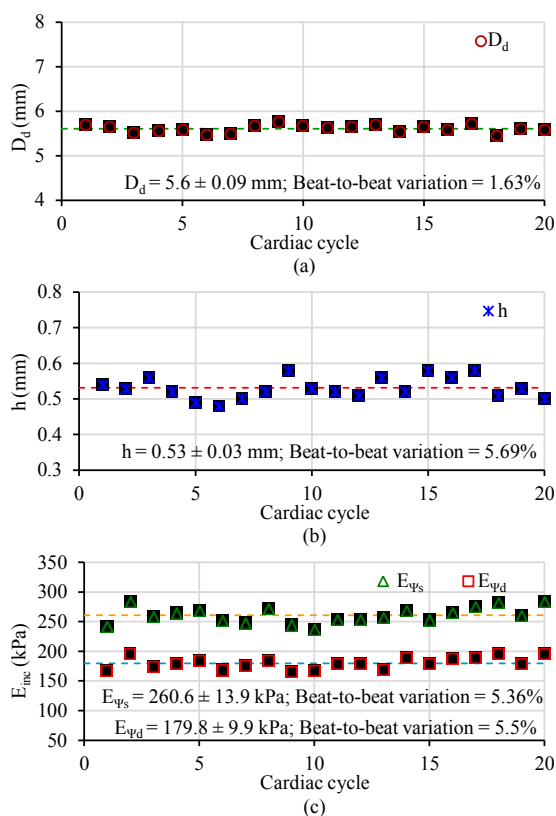


Figure 4: Beat-by-beat variations of (a) D_d (b) h (c) E_{inc} obtained from the LCCA for a particular subject

the recruited subjects are summarized in tab. 1, (values expressed as mean \pm SD). The obtained values of E_{inc} concur with studies reported earlier [12]. A statistically significant ($p < 0.001$) variation between E_{ψ_s} and E_{ψ_d} was observed in all subjects over continuous cardiac cycles. Consistent with theory, the absolute values of E_{ψ_s} was greater than E_{ψ_d} . This indicates that the elastic characteristics of an arterial segment are not constant, which otherwise vary over the cardiac cycle as a function of distending arterial pressure.

Limitations of the Present Study

The validation study was conducted only on a small group of normotensive subjects. An extensive clinical study on a large population including hypo and hypertensive subjects is required to further validate the proposed technique. Simultaneous evaluation of beat-by-beat E_{ψ_s} and E_{ψ_d} using ultrasound-pressure probe of the proposed system and a reference ultrasound imaging system was not practically viable.

Conclusions

A non-invasive measurement system for the evaluation of E_{inc} and its variation over the cardiac cycle in a beat-by-beat manner was presented. A novel ultrasound-pressure probe was designed and developed for the simultaneous capturing of high fidelity diameter and pressure waveforms from the carotid artery. PD loops obtained from these waveforms exhibited a non-linear pressure-diameter

relationship. Beat-by-beat evaluation of arterial dimensions was performed using application-specific measurement software. E_{inc} at two distinct fiducial points in the neighborhood of systolic peak and end-diastolic region (E_{ψ_s} and E_{ψ_d}) were obtained from the recorded h , D_d measurements and PD loop. The functionality of the developed prototype system was validated by conducting an *in-vivo* study on 10 subjects. Observed beat-to-beat variation in D_d ($< 4\%$), h ($< 7.5\%$), E_{ψ_s} ($< 7\%$) and E_{ψ_d} ($< 7\%$) were in the acceptable range, indicating the reliability of the measurements. The absolute values of E_{ψ_s} were greater than E_{ψ_d} in all recruited subjects and showed a significant variation ($p < 0.001$), which was consistent with the theory. The present study results have demonstrated that the proposed system can reliably assess E_{inc} and its variation within a cardiac cycle in a non-invasive manner, which can be potentially used for the screening of various cardiovascular events. Further efforts are needed to translate the prototype system to a portable hand-held device with integrated ultrasound-pressure transducer in-order to make it to clinical practice for cardiovascular screening.

References

- [1] S. Laurent et al. Expert consensus document on arterial stiffness: methodological issues and clinical applications. *Eur Heart J*, 27(21):2588–2605, 2006.
- [2] R. E. Shadwick. Mechanical design in arteries. *J Exp Biol*. 202(23):3305–3313, 1999.
- [3] L. Niu et al. Standard deviation of carotid young’s modulus and presence or absence of plaque improves prediction of coronary heart disease risk. *Clin Physiol Funct Imaging*, 37(6):682–687, 2017.
- [4] A. Avolio. Arterial Stiffness. *Pulse*, 1(1):14–28, 2013.
- [5] J. Joseph et al. Method and system for cuff-less blood pressure (BP) measurement of a subject. US Patent US20170156706 A1, 2017.
- [6] A. P. Hoeks et al. Assessment of the distensibility of superficial arteries. *Ultrasound Med Biol*, 16(2):121–128, 1990.
- [7] F. Molinari et al. A state of the art review on intima-media thickness (IMT) measurement and wall segmentation techniques for carotid ultrasound. *Comput Methods Programs Biomed*, 100(3):201–221, 2010.
- [8] A. P. Hoeks et al. Effects of assessment and processing techniques on the shape of arterial pressure-distension loops. *J Vasc Res*, 37(6):494–500, 2000.
- [9] A. K. Sahani et al. Automatic measurement of end-diastolic arterial lumen diameter in ARTSENS. *J. Med. Devices*, 9(4):1-11, 2015
- [10] J. Joseph, et al. Technical Validation of ARTSENS—An Image Free Device for Evaluation of Vascular Stiffness. *IEEE J Transl Eng Health Med*, 3:1–13, 2015.
- [11] V. K. Raj et al. An image-free ultrasound method to estimate artery wall thickness surrogate for screening. In *MeMeA 2017*, pages 326–33. IEEE Rochester, May 2017.
- [12] E. Urbina et al. Correlates of carotid artery stiffness in young adults: The Bogalusa Heart Study. *Atherosclerosis*, 176(1):157–164, 2004.

The patterning of biostructures with carbon nanoframe in protein matrix

A.Yu. Gerasimenko^{1,2}, O.E. Glukhova³, M.M. Slepchenkov³, N.N. Zhurbina¹, M.S. Savelyev^{1,2}, L.P. Ichkitidze^{1,2}, V.M. Podgaetskii¹, S.V. Selishchev¹, E.P. Kitsyuk⁴, A.A. Pavlov⁵

¹ Institute of Biomedical Systems, National Research University of Electronic Technology, Zelenograd, Russia

² Institute for Bionic Technologies and Engineering, I.M. Sechenov First Moscow State Medical University, Moscow, Russia

³ Saratov State University, Saratov, Russia

⁴ Scientific-Manufacturing Complex "Technological Center", Zelenograd, Russia

⁵ Institute of Nanotechnology of Microelectronics of the RAS, Moscow, Russia

Contact: Natalia93Zhurbina@gmail.com

Introduction

The creation of three-dimensional frame materials is an urgent task for various fields, from biomedicine to emissive electronics. Creation of carbon nanotubes (CNTs) frame with strong heating by laser irradiation has been described [1]. The heating provides the connection of single-walled nanotubes to each other in defective areas of the carbon's structure. The purpose of this paper is to describe the mechanism of carbon nanotubes patterning under laser irradiation in a protein matrix to create a nanomaterial for tissue-engineering. To understand the nature of the nanotubes patterning in the frame, we considered the features of the interaction of defective regions and open ends of CNTs with laser radiation in the UV-visible-IR range. Defective areas inefficiently divert heat, so with a general heating of the nanostructure, these areas overheat more noticeably and can eventually collapse [2, 3]. Patterning of biostructures with a carbon nanoframe in protein matrix under the influence of pulsed laser radiation was studied. It was also experimentally confirmed that laser pulse of nanosecond duration has a structuring effect on an array of CNTs. These biostructures with a carbon nanoframe in protein matrix can be used as bulk biomaterials for restoration of defects in damaged tissues, due to their ability to enhance cell proliferation and tissue regeneration [4 - 6].

Materials and Methods

If we consider the energy absorption in the case of a normal incidence of a plane electromagnetic wave, then it is possible to calculate the absorption coefficient. Maxwell's theory and the quantum-mechanical approach are used in this case. The nanotube array acts as the interface between the two media. Both media are vacuum. We consider the process of interaction of a network of nanotubes with an incident wave that passes from vacuum through a network of nanotubes to vacuum again. We considered waves with a vector E directed along the nanotube axis and perpendicular to it. The absorption coefficient was determined by the formula:

$$A = 1 - |R|^2 - |T|^2, \quad (1)$$

where $|R|^2$ and $|T|^2$ are the squares of the modules of complex reflection and transmission coefficients. We have

taken the most frequently synthesized single-walled carbon nanotubes such as armchair and zigzag. Their diameter was 0.7 - 3 nm. We investigated nanotubes with defects of 1V type (one vacancy of the carbon atom), 2V (two vacancies of carbon atoms), SW (defect of the connection rotation) and mixed type 1V + SW. Nanotubes with open ends were also investigated. Laser radiation was considered in the wavelength range of 0.01-2 μm . Carbon nanotubes absorb energy depending on the chirality and polarization of the wave.

Based on the results of the study of the absorption of laser beam energy by defective parts of CNTs, we carried out a series of numerical experiments of the binding of nanotubes in an aqueous solution. In an aqueous solution, nanotubes can move relatively freely. The process of binding of two nanotubes with defects of 2V, 1V, SW and SW + 1V types was simulated. These defects, as it was shown above, allow the defective sections to absorb energy by $\sim 50\%$ more at a certain wavelength. Numerical experiments were carried out by the method of molecular dynamics using adaptive intermolecular reactive empirical bond order potential to describe the behavior of defect-free nanotube regions and the environment and the self-consistent charge density functional tightbinding method, which describes the appearance of covalent bonds between tubes. The simulation step was 0.1 fs.

For the experimental studies, we used single-walled nanotubes, which were synthesized by an electric arc method on a Ni-Y catalyst. They were further purified in air with washing in HCl and carboxylated in a mixture of $\text{HNO}_3 / \text{H}_2\text{SO}_4$, then washed with water until neutral reaction. Analysis of the results of Raman spectroscopy showed that the average diameter of CNTs was 1.8 ± 0.2 nm, and that there were defective structures in the array of tubes. As the protein matrix, an aqueous solution of albumin and collagen was used. For the patterning of protein biostructures with a carbon nanoframe, a Ti: Sa femtosecond laser of 810 nm with a pulse duration of 140 fs and a repetition rate of 80 MHz was selected.

In addition, the experimental studies of the interaction of pulsed laser radiation with an array of carbon nanotubes grown on a silicon substrate were carried out. The sample was located perpendicular to the laser beam at the lens focus $F=10$ cm. CNTs were grown by PE-CVD method with Ni-Ti (10/2 nm) catalyst in C_2H_2 , Ar and NH_3 at

mosphere and temperature of 550 °C. Nanotubes in array have average diameter of 40-50 nm and the length of 7.3-7.6 μm.

The source of laser radiation was a solid-state pulsed Nd:YAG laser with wavelength of 1064 nm and a pulse duration of 16 ns. The pulse energy of Nd:YAG laser depended on the optical pumping energy of the active element Nd:YAG and was controlled directly by the laser control unit. Leaving the laser, the beam hit the prism of Glan, transforming radiation with arbitrary polarization into a linearly polarized, parallelly regulating the energy of the beam with a given step. The pulse energy varied in the range of 1.21-4.158 μJ. The energy density of the pulse was in the range of 0.4-2.2 J / cm². After leaving the Glan prism, the laser beam hit the wedge-shaped quartz prism, reflected from it (the energy of the reflected beam was ~ 10% of the original beam) and hit the energy meter based on the Ophir PD-10 sensor. The action was effected by single laser pulses at different areas of the sample.

Results

We performed one modeling experiment for 1V, 2V and 1V + SW defects single-walled carbon nanotubes. Using the finite-difference time-domain method we obtained the patterns of the distribution of the electromagnetic field's magnitude *E* over the volume of carbon nanotubes. Fig. 1a shows the maximum values of the intensity *E*, which are indicated in red. The distribution of temperature along the tube was initially uneven, taking into account the inhomogeneous absorption of the electromagnetic wave's

energy. In the defect area, the temperature was maintained at 50% more than in ideal sections of the tube. One of the results of the binding of nanotubes (12,12) with one 2V defect in each tube, perpendicular to each other is shown in Fig. 1b-d. The unevenness of temperature distribution during nanotubes binding is shown in Fig. 1b. The maximum values of the temperature (1600-1700 K) correspond directly to the close region to the 2V defect.

The distance between the nearest tubes in the solution was in the range of 3.2 to 4 Å. The binding time was determined by many factors, including the distance between the tubes. Figure 1d shows the atomic structure of the tubes when four stable bonds were formed.

We have established that uneven temperature heating leads to the formation of covalent bonds between the tubes even at an initial distance above 3.2 Å. We performed a numerical experiment that described the interactions of two nanotubes (12,12) with defects of 2V type. The change of energy during the formation of bonds in time (within 8 ps) varied in the range -7.43 – 7.36 eV / atom.

Fig. 2 shows an image of scanning electron microscopy of a nanoframe structured by laser radiation from carbon nanotubes in a protein matrix. The sample was located on a conducting silicon substrate and split in the center. Fig. 2 shows a branched tree-like structure of single-walled carbon nanotubes. Laser structuring and the formation of a branched framework under the action of covalent bonding are confirmed by high values of the nanohardness of the material ~ 300 MPa.

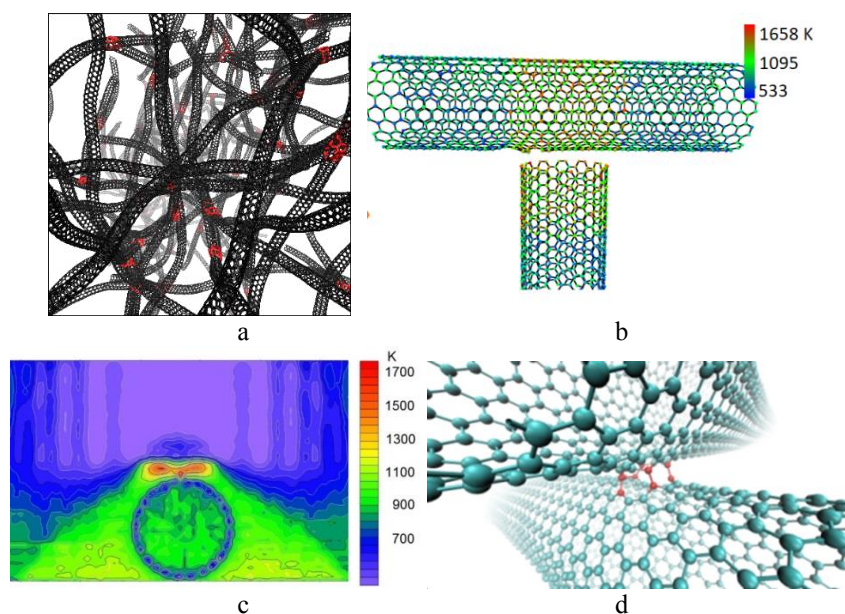


Figure 1: Binding of nanotubes into a carbon nanoframe (a shows the distribution of the maxima of the laser radiation electromagnetic field, b shows the uneven distribution of temperature in the tubes caused by uneven absorption of the energy of the incident laser radiation, c shows the temperature field near the nanotubes contact after cessation of laser irradiation, d shows the process of covalent bonds formation)

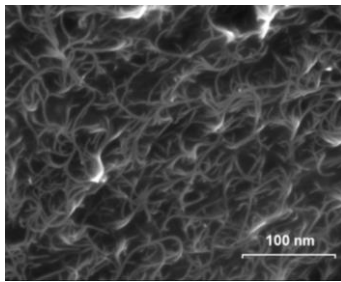


Figure 2: SEM image of a biostructure with a carbon framework in a protein matrix

The study of the CNTs before and after interaction with laser radiation was carried out using scanning electron microscopy (Fig. 3).

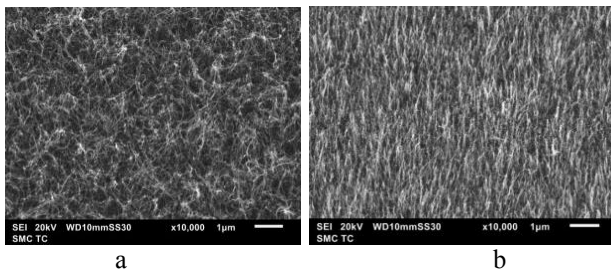


Figure 3: SEM image of a CNTs array before (a) and after (b) laser irradiation with energy of 180.4 μJ

The dependence of the alignment degree of the carbon nanotubes array on the energy of the laser pulse was observed. At energies of less than 100 μJ , the alignment effect was practically not observed. At an energy of 135 μJ , an alignment effect began, which reached a maximum at 180 μJ , and then decreased. At energies above 200 μJ , thinning of carbon nanotubes was observed, as well as partial destruction of their structure.

Conclusions

The mechanism of covalent bonding of single-walled carbon nanotubes under the action of laser heating was revealed. Its essence lies in the formation of hot spots in the areas of defects and open ends of nanotubes due to a strong uneven heating during absorption of laser radiation. It was shown that binding can be controlled by forming hot spots in the necessary tube regions by forming one or two defects of 1V, 2V, SW and 2SW + 1V type. In the regions of these defects, the absorption of the laser beam reaches 50% in comparison with 5% absorption of a nanotube without defects. The change in energy during the formation of bonds in time (within 8 ps) varies in the range -7.43 - 7.36 eV / atom. Self-formation of a frame nanomaterial from nanotubes dispersion predominantly formed by semiconductor tubes with diameter of 1.8 ± 0.2 nm, under irradiation of Ti:Sa femtosecond laser with wavelength of 810 nm was demonstrated experimentally. Samples of bioconstructions had a tree-like branched structure of carbon nanotubes frame with nanohardness up to 300 MPa. Also, it was shown that laser pulse of na-

nosecond duration has a structuring effect on an array of carbon nanotubes. As the energy of the pulse increased, the effect of cleaning and thinning carbon nanotubes was observed. It was associated with laser heating and covalent bonding of nanotubes in defective regions and near the ends of the tubes.

It is expected that the ordered structure of biostructures with carbon nanoframe in protein matrix should promote improved cells fixation. Thus, biostructures will be able to be used as a matrix for cell adhesion and growth, which will be confirmed by in vitro and in vivo studies.

References

- [1] A. Gerasimenko, O. Glukhova, G. Savostyanov, V. Podgaetsky. Laser structuring of carbon nanotubes in the albumin matrix for the creation of composite biostructures. *J Biomed Opt*, 22(6):65003, 2017.
- [2] J. Che et al. Thermal conductivity of carbon nanotubes. *Nanotechnology*, 11:65–69, 2000.
- [3] G. Zhang. *Thermal Transport in Carbon-Based Nanomaterials (Micro and Nano Technologies)*. Elsevier, 2017.
- [4] N. Zhurbina, et.al. Investigation of cell proliferative activity on the surface of the nanocomposite material produced by laser radiation. *Proc. SPIE 9917*: 991718-991724, 2016.
- [5] L. P. Zanello et al. Bone cell proliferation on carbon nanotubes, *Nano Lett.* 6(3):562–567, 2006.
- [6] O. Im, et.al. Biomimetic three-dimensional nanocrystalline hydroxyapatite and magnetically synthesized single-walled carbon nanotube chitosan nanocomposite for bone regeneration. *Int. J. Nanomedicine*, 7:2087-2099, 2012.

Acknowledgements

This work was provided by the Ministry of Education and Science of the Russian Federation (Agreement 14.578.21.0221, RFMEFI57816X0221).

Mixed Reality applications for the collaborative operating room – a prototypical study

N. Marahrens¹, D. Ostler¹, J. Weinzierl¹, N. Kohn¹, T. Vogel^{1,2}, D. Wilhelm^{1,2}, S. Koller¹, H. Feußner^{1,2}

¹Research Group MITI at the University Hospital rechts der Isar of the TU Munich, Trogerstr. 26, Munich, Germany
²Clinic and Polyclinic for Surgery at the University Hospital rechts der Isar of the TU Munich, Ismaninger Str. 22, Munich, Germany

Contact: nils.marahrens@tum.de

Introduction

The rapid development of medical technology enables new treatment methods and leads to a strong increase in minimally invasive surgical interventions. For this reason, more and more specific devices are constantly being added to the OR. At the same time the OR staff faces the challenge to manage the adjustment and timely provision of these devices during surgery [1]. Similarly, nursing teams in Germany are increasingly understaffed and are consequently filled with staff from other European countries that may have difficulties knowing the specific terms in the OR or understanding the requirements for each situation [2].

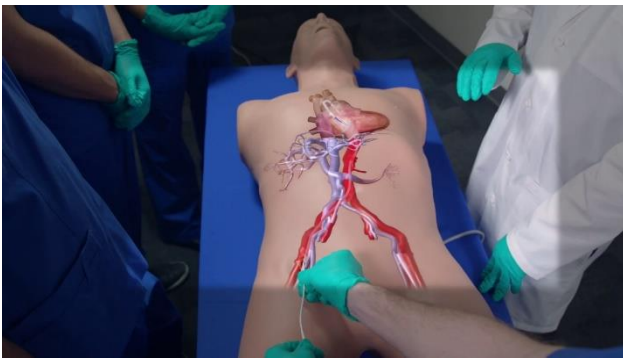


Figure 1: Exemplary application of the HoloLens for medical training (Source: caehealthcare.com)

Strategies and measures must therefore be developed to ensure and further improve efficiency, safety and outcome of the intervention. This requires solutions that bring staff and technology closer together in order to simplify system management of the OR, reduce communication issues and improve staff collaboration.

Mixed Reality (MR) applications may be a key technology to make this vision a reality. They are capable of providing information by more general means than pure language. At the same time, recent developments in machine learning allow enhanced image detection [3], workflow recognition [4] and natural language processing [5] in real time during surgery. In their combination these techniques may enable technical systems to robustly interpret the current surgical context, automatically provide the required information at the right time and react flexibly to changing demands.

In addition to providing solely information, MR application would further allow to sterilely adjust most devices in the OR from a central entity. Previously, this technology has already been used for medical training [6] (also see Fig. 1) and specific surgical applications [7]. However, most developments have mainly focused on the surgeons and less on the remaining OR staff so far.

Under these assumptions this paper investigates the potential of mixed reality applications for sterile interaction within the collaborative operating room. An exemplary use case of an assistive device that supports the scrub nurse in selecting the correct instruments is presented and evaluated in an initial user experience experiment.



Figure 2: Image of the HoloLens (Microsoft, Redmond, WA, USA) as used in the presented mixed reality application (Source: microsoft.com)

Materials and Methods

To realize a simple prototype of the envisioned system, we employed a Microsoft HoloLens (see Fig. 2). The HoloLens is a wearable device that enables the augmentation of the physical world with virtual entities. It is equipped with a multitude of sensors that enable the device to localize itself within the environment (spatial mapping) and enable various modes for user interaction.

Spatial mapping is performed by means of 4 greyscale cameras and a time-of-flight (TOF) sensor that enhances the camera images with further depth information. An additional inertial measurement unit (IMU) may also measure acceleration and spatial orientation. By combining all different sensory data, the HoloLens is able to locate itself and project holograms at any desired location within the room. All necessary sensor fusion is directly processed on the HoloLens' proprietary computer.

Aside from the possibility to interact with the system via head movements and hand gestures, the HoloLens also include four microphones to allow voice control and binaural speaker for audio feedback.

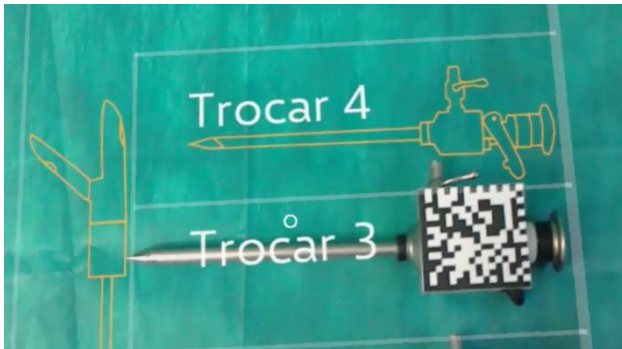


Figure 3: Segment of the grid that is projected onto the surgical tray

Included Functionalities

Our proposed assistive system supports the scrub nurse in identifying the instruments that are currently needed. It projects a grid onto the surgical tray (see Fig. 3). Each grid cell is reserved for one specific instrument and denoted by the instrument's name and contour sketch. With the integrated spatial mapping function, the grid cell pattern is automatically projected onto the surgical tray at a specified location. Through gestures the user is able to flexibly relocate the grid as desired within the plane of the surgical tray. Gestures are robustly recognized by the system even when the hands are covered with surgical gloves.

If an instrument has been placed in its corresponding grid cell, the contour sketch automatically disappears to give the user direct feedback about his or her action. The user may also interact with the system through verbal commands. By calling the name of an instrument the system clearly highlights the respective grid cell with a red box.

Currently, the integrated computer vision software of the HoloLens is not able to recognize and distinguish between the different surgical instruments in the scene. Particular problems arose due to the delicate and similar structure of some instruments. Furthermore, specular reflections from metallic surfaces highly reduced recognition accuracy. An integration of custom image processing algorithms that make use of the spatial information and could feed back their results to the HoloLens in real time are currently and to the authors' best knowledge not applicable within the API for the HoloLens. However, this functionality is crucial for the system to determine if an instrument has been correctly placed in its corresponding grid cell. For the first prototype we therefore attached QR-code markers to each instrument that were recognized within the HoloLens' video frames.

Experimental evaluation

Based on our prototype we performed a user experiment with 14 participants, some with prior OR experience. None had direct experience as a scrub nurse. During the test, participants first received a short introduction to the interaction modalities of the HoloLens such as gesture and voice control. Once participants were acquainted with the HoloLens in general, they were asked to set up the system and test out the assistive functions.

First off, users were presented the projected grid and were asked to relocate the grid to a desired position by means of gesture control. After the grid was in the right position, the participants had to place a total of 13 different surgical instruments in their respective grid cells as it is shown in Fig. 3. If the user had correctly placed the instrument in a grid cell, the contour sketch disappeared. If it did not disappear, the user had to pick up the instrument again, find the correct box and place the instrument there. Additionally, the participants were asked to interact with the system via voice commands in order to highlight the grid cells and contour sketches of specific instruments.

After successful completion the participants were all asked to fill out a User Experience Questionnaire (UEQ) [8], including a total of 26 statements that had to be rated with a 7-step Likert-scale. All statements fell into six different categories: "Attractiveness", "Perspicuity", "Efficiency", "Dependability", "Stimulation" and "Novelty".

To facilitate evaluation, we mapped the 7-step Likert-scale that takes values from 1 to 7, to values between -3 and 3 as it is also done in [9]. The resulting scale made it easier to directly tell if the user experience was rather positive (positive values) or rather negative (negative values).

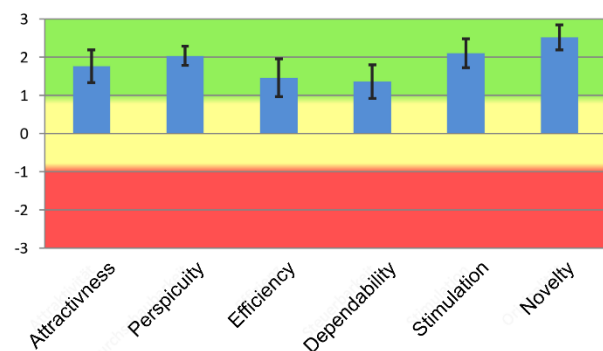


Figure 4: Results from the User Experience Questionnaire (UEQ) [8]

Aside from the user experiments voice recognition accuracy was tested for all 13 instruments by calling their respective name various times (n=30) and recording if the system recognized the command correctly.

Results

All participants were able to accomplish the task without major difficulties and therefore also completed the stand-



ardized questionnaire subsequent to the experiment. The detection of the QR code worked stable, was, however, sensitive to the distance and angle to the HoloLens' camera.

The system received mean ratings between 1.357 and 2.518. Fig. 4 shows the results as means and standard deviations over all participants and for all six categories. The scale is divided into three sections: -3 to -0.8 (very poor / poor), -0.8 to +0.8 (mediocre) and +0.8 to +3 (very good / good), marked by the respective colors red, yellow and green. Therefore, the ratings for all categories were considered as at least "good". The standard deviation takes values of less than 0.5 points in all categories. Specifically "Perspicuity", "Stimulation" and "Novelty", received the highest grades, where "Perspicuity" means how intuitive and clear the system is. Ratings for "Efficiency" and "Dependability" were the lowest, however, still fall into the highest of the three categories and were thus also considered as "good".

A relative comparison with benchmark results for typical UEQ ratings showed that for the categories "Attractiveness", "Perspicuity", "Stimulation" and "Novelty", the presented system ranks among the top 10% of the results contained in the benchmark [9]. The remaining categories "Efficiency" and "Dependability" still rank above average.

Voice detection also worked well for most instruments. Detection rates were above 70% for all instruments. All except the two keyword "PE Forceps" and "Scissors" were even detected with an accuracy of 90% or more.

Discussion

In this context, the results underline that the system was well received by most participants and its user experiences ranks well among other applications. The test clearly showed that the general concept of the system works well and that the interaction between the user and the system is intuitive. Since the test did not primarily include professional scrub nurses, this conclusion may only apply to the general usage of the system in an OR setup. Clear statements about the integration into the actual workflow and its further interaction with the additional OR team members cannot be made at this point.

Conclusions

Currently, the presented system could already be used for training, whereas a sterile application in the OR is hindered by the QR-code tags that are still necessary for instrument recognition. With further advancements in computer vision, however, a direct detection from the image may already be feasible, given that the HoloLens' API allows a practical integration of custom algorithms.

Although the HoloLens is already employed for real medical applications, its weight of 579g and its relatively

short battery life of 2 to 3 hours of active use might restrict their application during real surgery. Particularly for longer surgical interventions, the system might not be practical at its current state.

Future research will be devoted at its integration into the OR and the preexisting workflow. The system is planned to be coupled to a workflow recognition engine that aids at automatically highlighting the required instruments in each situation. We further work on enhancing the system's flexibility by integrating verbal information given by the surgeon. Further user experiments will put a stronger focus on OR staff members, particularly scrub nurses, and their collaboration with the remaining OR team.

References

- [1] Carpintero, E., Pérez, C., Morales, R., et al., Development of a robotic scrub nurse for the operating theatre. *3rd IEEE RAS & EMBS International Conference on Biomedical Robotics and Biomechatronics*, 2010
- [2] C. Schäfer. Risikofaktor Pflegekräftemangel. *Dialyse aktuell*, 16 (09): 483-483, 2012, in German
- [3] Ren, S., He, K., Girshick, R., & Sun, J. (2015). Faster r-cnn: Towards real-time object detection with region proposal networks. In *Advances in neural information processing systems* (pp. 91-99).
- [4] R. Stauder, N. Navab et al. Learning-based Surgical Workflow Detection from Intra-Operative Signals. *arXiv preprint arXiv:1706.00587*, 2017
- [5] Young, T., Hazarika, D., Poria, S., & Cambria, E. (2017). Recent trends in deep learning based natural language processing. *arXiv preprint arXiv:1708.02709*.
- [6] C. Kamphuis et al. Augmented reality in medical education? *Perspectives on medical education* 3.4: 300-311, 2014
- [7] N. Navab, T. Blum et al. First deployments of augmented reality in operating rooms. *Computer*, 45 (7): 48-55, 2012
- [8] B. Laugwitz, M. Schrepp et al. Construction and evaluation of a user experience questionnaire. *Symposium of the Austrian HCI and Usability Engineering Group*, 2008
- [9] M. Schrepp et al. User Experience Questionnaire Benchmark Praxiserfahrungen zum Einsatz im Business-Umfeld. *Usability Professionals*, 13: 348-353, 2013, in German

Acknowledgements

The project was supported by Deutsche Forschungsgemeinschaft (DFG, grant FOR 1321)

Longterm high resolution manometry (HRM) challenges and pitfalls of an automated motility analysis

A. Jell¹, N. Hüser¹, S. He¹, D. Ostler¹, D. Telyshev², S. Selishev², H. Feußner¹

¹Department of Surgery, Klinikum rechts der Isar, Technical University Munich, Germany

²National Research University of Electronic Technology, Moscow, Russia

Introduction

High resolution manometry (HRM) of the esophagus is the gold standard in the diagnosis of esophageal motility disorders[1]. However, it only measures a short period of time and allows only to distinguish between the most common esophageal motor abnormalities with the help of Chicago Classification[2]. As the measurements take place in clinic for a very limited period of time only little is known about circadian changes in esophageal motility. Especially for patients with intermittent symptoms conventional, short-term HRM cannot assess the underlying causes of the disease precisely.

Therefore, we prolonged the time of measurement to a full of 24 hours using a combined ambulatory impedance-manometry device consisting of 36 pressure channels and 15 impedance channels[3]. With this setting it is possible to examine esophageal motor function throughout a whole day whilst the patient is following her/his normal duties.

The aim of our project was to establish normal values for healthy persons and to identify patients with transient esophageal problems as only little is known about normal and pathological patterns when examining esophageal motor function and dysfunction throughout a whole day.

Materials and Methods

For the longterm high resolution manometry (HRM) we used a 10 French Solide State Manometry catheter designed for high resolution impedancomanometry studies (Unisensor, Attikon, Swiss). In the probe, the esophageal pressure values are already digitalized and sent to the portable recording unit MALT™ (Standard Instruments, Karlsruhe, Germany). With the power supply of two standard lithium AA-batteries the systems allows studies up to 26 hours. The recording unit has an internal memory of 1 GB

size and can store pressure plots of 36 pressure channels with a rate of 50 Hertz without the necessity of data compression.



Figure 1: Device for ambulatory high resolution manometry of the esophagus

In addition to the huge amount of pressure raw data, complementary information on body position, eating and drinking habits as well as sleeping is integrated into the dataset.

With this newly developed device we have been recording more than 80 longterm high resolution manometries since the beginning of our project. Technical and clinical feasibility was documented prospectively and iteratively improved.

Evaluation

The 24 hour recordings of normal, healthy test persons were manually analysed. An extended Chicago classification system was used (Fig. 2).

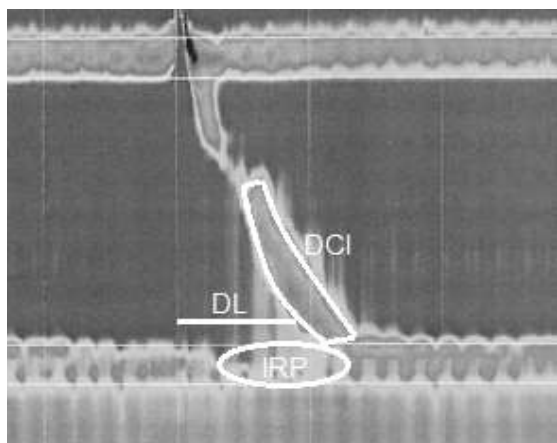


Figure 2: Important values for evaluation of esophageal motility according to Chicago Classification Version 3.0 (DL = distal latency, DCI = distal contraction integral, IRP = integrated relaxation pressure)

Parallely, an automated analysis program was developed, based upon the classical Chicago criteria. An act of swallow was assumed as soon as a relaxation of the upper esophageal sphincter (UES) was followed by sequential contractions measured by the more distal sensors. With the ongoing evaluations, it became clear that this rather rigid algorithm had to be changed as described below.

Results

Technical and organizational problems

Though the probe is quite rigid and has a diameter of about 3mm (10 French) the examination is accepted by our patients and in our healthy volunteers quite effortlessly. Only three measurements had to be stopped before time.

More problematical in the performance of longterm high resolution manometries are technical aspects. The used solid state probes are high end products and are designed for about 200 uses (about 600 operating hours). When extending the time of measurement to 24 hours, the guaranteed operating hours are reached within 25 measurements which rises the costs of a single measurement to around 720 €. Especially with the longterm use the probes need more reiparement and checking which adds additional costs to each examination.

Manual Evaluation

Up to now there is no program for automated computer analysis of HRM and especially non for long-term measurements available.

As expected, manual analysis of the pressure recordings was extremely tedious and time consuming. However, it yielded important new insights.

“Static” parameters

These so called static parameters represent the resting pressure of both high pressure zones in the esophagus: the upper and the lower esophageal sphincters.

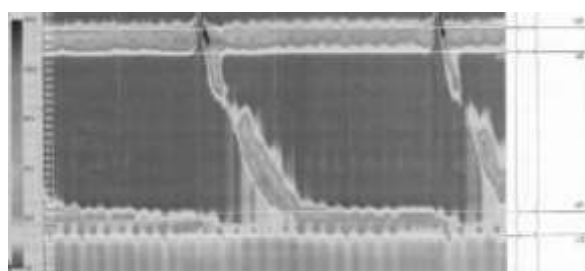


Figure 3: Color-coded HRM pressure plot of a normal swallow that starts with relaxation of upper esophageal sphincter, followed by a propulsive peristalsis and ends by contraction of the lower esophageal sphincter. (right: marking of pressure bands of upper and lower esophageal sphincter)

We found that physiological (complete) swallows as shown in the figure above (Fig. 3) do not at all represent the majority of all motor events of circadian esophageal motility. Depending upon posture (upright/prone) and food intake, a considerable number of incomplete swallows occurred. In these instances, a clear relaxation of the UES is not observed, but the distal contractile sequences show the typical pattern.

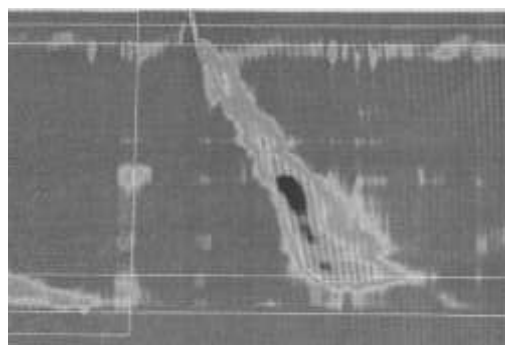


Figure 4: Relaxation of the UES is barely visible. Though a human analysist would recognize the act of swallowing, a machine based system would certainly not recognize this type of motor event

Even more surprisingly, irregular motor events could be detected in healthy people without any esophageal problems. Retropulsive contractile sequences could be observed as well as distal cramps (Fig. 4) or transient relaxations of the lower esophageal sphincter (TLESR) which were often followed by reflux (Fig. 5).

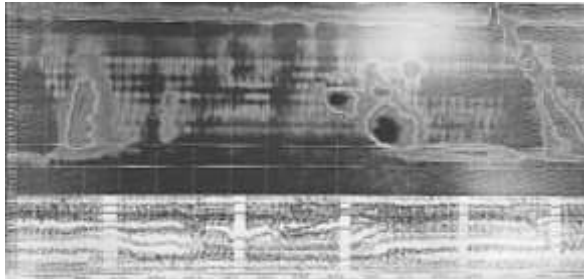


Figure 5: Transient sphincter relaxation, followed by fluid reflux (as seen in impedance measurement at below the HRM plot) and a distal contractile wave before an act of clearance swallowing

Systematic further classification of the normal motility pattern is currently conducted. Up to now, we are still unable to present a complete catalogue of physiological circadian pressure events. At any rate, “irregular” contractile events which were considered pathological in our previous analyses can be found frequently in normal test persons as well.

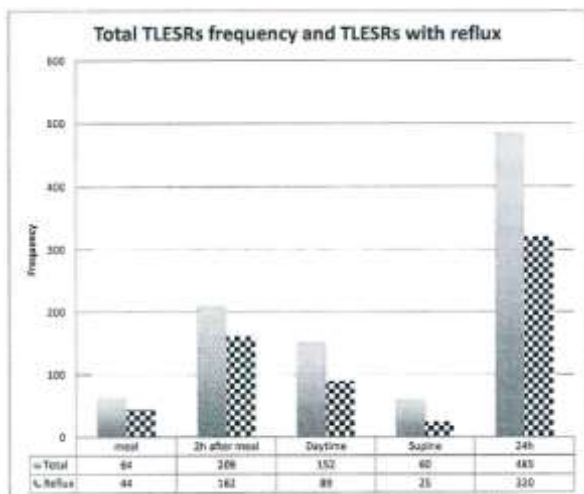


Figure 6: Total number of TLESR and TLESR with reflux

When analysing our patients with reflux disease it shows that the mean resting pressure of the lower esophageal sphincter underlies a slight modulation with an increase of resting pressure and the integrated relaxation pressure during nighttime. Whereas in the upper esophageal sphincter resting and relaxation pressure stay stable throughout the measurement. Most remarkably, the number of TLESR are appearing dependent of the circadian cycle.

Dynamic parameters

Dynamic parameters is the preamble for all values that can only be measured during an act of swallowing (eg. transportation velocity, area under the curve).

In patients with known reflux disease significant changes in the cause of measurement can be seen in the value of DCI (distal) and PCI (proximal contraction integral), the intrabolus pressure (IBP), in distale latency (DL) and distal contraction velocity (DCV).

Problems of automated analysis

As manual analysis is not feasible in clinical practice it is by now possible to get a computer aided analysis according to the newest Chicago Classification. These computer aided programs tend to correctly mark pressure landmarks during swallowing whenever an act of swallowing is marked correctly beforehand. For an expert in analysis of HRM the analysis of a whole dataset can be performed in around 20 hours which excludes it from clinical routine.

Originally an algorithm for detecting an act of swallowing was developed which relied on the pressure changes in the UES. A swallow was assumed if a relaxation in the upper esophageal sphincter was followed by a characteristic postdeglutitive increase of pressure.

The rate of complete swallows that can be evaluated with measurements of the parameters shown in Fig. 1 was very high (>95%) but unfortunately these typical contractile sequences made up only about 1/3 of circadian motor events of the esophagus. Especially motility patterns without oropharyngeal triggering of a swallow (e.g. secondary peristalsis waves for esophageal clearance, ...) aren't considered for analysis at all [4]. Whilst typical motor events can be evaluated with computer-assisted programs the remnant has still to be evaluated manually.

Conclusion

Analysis of longterm high resolution manometry (HRM) is at the moment not yet feasible in clinical routine. It is essential to develop a computer program to bring longterm HRM into clinical practice. As shown above, automatic analysis is by far more complex than it is when performing short time analysis according to the Chicago Classification. As there are



up to now no bigger series on normal and pathological values with longterm manometry studies it is hard to define new, more suitable algorithms for computer analysis of HRM. Further studies will be necessary to build up a big database of normal and pathological

values as well as newer and more elaborated algorithms (eg. deep learning methods) will be necessary for a better understanding of circadian motility patterns of the esophagus.

Conflicts of interest:

No conflict of interests. The project was supported by Dr. Pflieger-Stiftung Bamberg, Germany.

References:

1. Roman S, Pandolfino J, Mion F. High-resolution manometry: a new gold standard to diagnose esophageal dysmotility? *Gastroenterologie clinique et biologique* 2009; 33: 1061-1067
2. Kahrilas PJ, Bredenoord AJ, Fox M et al. The Chicago Classification of esophageal motility disorders, v3.0. *Neurogastroenterol Motil* 2015; 27: 160-174
3. Jell A, Wilhelm D, Ostler D et al. Langzeit-HR-Manometrie der Speiserohre: Erste Beobachtungen aus dem klinischen Einsatz. *Zeitschrift fur Gastroenterologie* 2016; 54: 1069-1075
4. Samoilov A, Telyshev D. Determination of Heart Rate Variability from High-Resolution Esophageal Manometry Data. *Biomedical Engineering*, DOI 10.1007/s10527-018-9742-y:

Investigation of the spectral properties of media based on chitosan and carbon nanotubes

Yu.O. Fedorova¹, A.A. Polokhin¹, D.T. Murashko¹, M.S. Savelyev¹, A.Yu. Gerasimenko^{1,2}

¹National Research University of Electronic Technology, Zelenograd, Moscow, Russia,

²I.M. Sechenov First Moscow State Medical University, Moscow, Russia

Contact: fedorovauo@mail.ru

Introduction

Common diseases of the cardiovascular system include pathological changes in connective tissue structures of the heart and large blood vessels due to atherosclerosis, inflammatory lesions, congenital inferiority or mechanical damage. These diseases led to the development of methods for creating tissue-engineered structures implanted in the area of damage to the tissues of the heart and blood vessels [1]. Such methods involve the formation of a three-dimensional biocompatible scaffold with its subsequent filling with living cells. One of the most effective and modern methods of creating such scaffolds is laser printing.

Biological and synthetic materials are used to create cellular and tissue engineering structures for the restoration of the cardiovascular system [2]. However, biological materials have deficiencies associated with the possibility of transmission of infections, and synthetic compounds do not provide the necessary mechanical and bioresorption characteristics. In view of this, there is a need for new materials for tissue engineering in the field of the cardiovascular system.

To create the considered structures it is proposed to use chitosan, basically this aminosugar is used as a matrix medium for fillers in the form of functional particles [3, 4]. The addition of carbon nanotubes to natural or synthetic polymer structures enhances the mechanical properties and enhances the electroconductive and physiological properties of the structure for restoring the tissues of the cardiovascular system [5].

In this paper, we present a study of chitosan-based samples with inclusions in the form of carbon nanotubes in order to use the composition as a starting material for the preparation of cellular and tissue-engineered structures used in cardiovascular surgery.

Materials and Methods

Two types of water-soluble chitosan, edible and succinate, were used in this study. Edible chitosan (EC) was obtained from high-molecular chitosan by chemical hydrolysis and was a cream colored powder with a main substance content of 88.4%, a moisture content of 3.13% and mineral substances of 0.53%. Chitosan succinate (CS) is derived from crab chitosan by interaction with succinic anhydride. The material was a pearl-cream powder with a residual moisture content of 4.79%, the pH of the aqueous solution was 7.7.

As a filler for the creation of samples, 2.7% aqueous paste based on single-walled carbon nanotubes (SWCNTs) was used. SWCNTs were obtained by gas-phase synthesis with a wash to 99% purity. The diameter of the tubes was 1-2 nm, the length exceeded 5 μm . The feature of nanoparticles was a high specific surface area – 420 m^2/g . Water dispersion media (dispersions) based on SWCNTs with EC and CS were obtained. First, SWCNTs were mixed on a magnetic stirrer for 20 minutes with distilled water to obtain a concentration of 10^{-5} %. The resulting dispersions were then subjected to a powerful ultrasonic field with a power amplitude of ~ 40 W for 50 min. Then a powder of EC and CS with a concentration of 1:49 was gradually added to the homogeneous dispersion of SWCNT. The mixture was then stirred in an ultrasonic bath with an operating frequency of 45 kHz for 40 minutes.

From the final dispersions obtained, film samples were prepared for the study by water evaporation upon the influence of laser radiation. A pulsed ytterbium laser (wavelength 1064 nm) and a semiconductor laser (970 nm wavelength) with a power of no more than 5 W were used as sources of laser radiation.

Raman spectra in the range 100-1800 cm^{-1} were measured using the LabRAM HR Evolution (Horiba) spectroscopic complex. As a source of exciting radiation, a HeNe laser with a wavelength of 633 nm was used.

Absorption spectra of samples in the IR range 4000-400 cm^{-1} (2.5-25 μm) were obtained by the method of attenuation total reflection using the Nicolet iS50 Fourier spectrometer (Thermo).

Results

To study the degree of binding of the aqueous dispersion components of chitosan to carbon nanotubes (CNTs), characteristic amide bands on IR and Raman spectra of film samples were analyzed. To compare the spectra, control samples from pure components are prepared separately.

IR Spectra

Peaks on the spectrum of pure chitosan turned out to be shifted relative to the peaks of films based on chitosan and SWCNT, and their intensity was sharply changed, which indicates the molecules connection of substances among themselves. From the spectrum of EC (see fig. 1), it is seen that the intense peak near 3350 cm^{-1} is due to stretching vibrations O–H and H–H (stretching of bonds);

the band of about 2868 cm^{-1} is connected with the valence vibrations of the C–H bonds.

A group of bands from 500 cm^{-1} to 1660 cm^{-1} is characteristic of the amide group (Amide I–Amide VI bands). Amide I (about 1550 cm^{-1}) characterizes the vibrational ability of the amide group, in which a periodic elongation of the C=O bond occurs, which can be used to judge the degree of acetylation. Comparing with the analogous peak in fig. 2b, we can conclude that the CS degree of acetylation is higher.

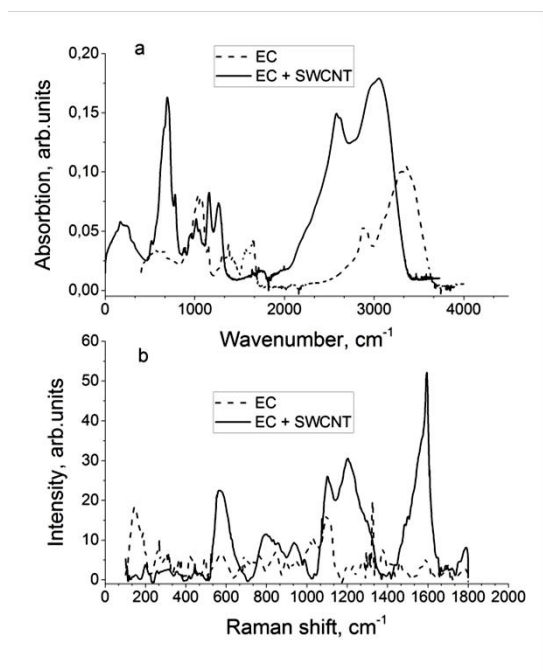


Figure 1: IR (a) and Raman (b) spectra of pure edible chitosan and with addition of CNTs

The absorption band of about 3450 cm^{-1} can be sensitive to adsorbed water, and an increase in the water content leads to an increase in the absorption band of about 1640 cm^{-1} , which was observed on the spectrum of EC with SWCNT. The difference in the intensity of the peaks near 3350 cm^{-1} and 1550 cm^{-1} in the CS spectrum is related to the degree of acetylation. Also, it is possible that the contribution of SWCNTs was more pronounced on the spectrum when connected to the EC.

A wider CS band of about 3350 cm^{-1} in comparison with EC could be associated with the stretching of the O–H bond, which overlaps the N–H stretching in the same region. It should be noted that intense peaks for CS with SWCNTs of about 1040 cm^{-1} and 1200 cm^{-1} are related to the stretching vibrations of C–C and C–O, which confirms the binding of the dispersion components to each other. A similar increase in intensity is observed for EC with SWCNT in the same region with respect to the spectrum of pure chitosan, however, the peak amplitudes are harsher than in the spectrum of CS. It is assumed that the penetration of SWCNTs into a more viscous gel-like

structure of EC with a concentration of 2% was weaker than in the more liquid CS sample.

Raman Spectra

As seen in fig. 1b and 2b, the spectrum of chitosan with SWCNT is shifted relative to the initial chitosan spectrum, which indicates changes in the structure of amino sugars and tubes. These shifts are responsible for connecting the components of the dispersion to each other.

The bands of about 1603 cm^{-1} correspond to the deformation symmetric vibrations of the amino group. The shape of the peaks in the spectrum of EC with SWCNT is similar to that of the spectrum of CS with SWCNT, which is mainly due to a stronger manifestation of the contribution of nanotubes to the Raman spectrum in comparison with the spectra of organic substances.

Peaks with frequencies of about 1200 cm^{-1} and 1120 cm^{-1} are responsible for the stretching vibrations of C–O and C–N, which were manifested in the spectra of EC and CS. These peaks shifted from their original position when chitosan was combined with the tubes, and their intensity increased sharply, which can be explained by the SWNT D mode that is strongly manifested in this region.

It should also be noted that SWCNTs exhibit semiconductor properties and do not have any structural damage, as can be seen from fig. 3b: the ratio of the intensity of the RBM mode (about 500 cm^{-1}), D and 2D modes (about 1200 cm^{-1} and 2800 cm^{-1}) with the G mode intensity (about 1594 cm^{-1}).

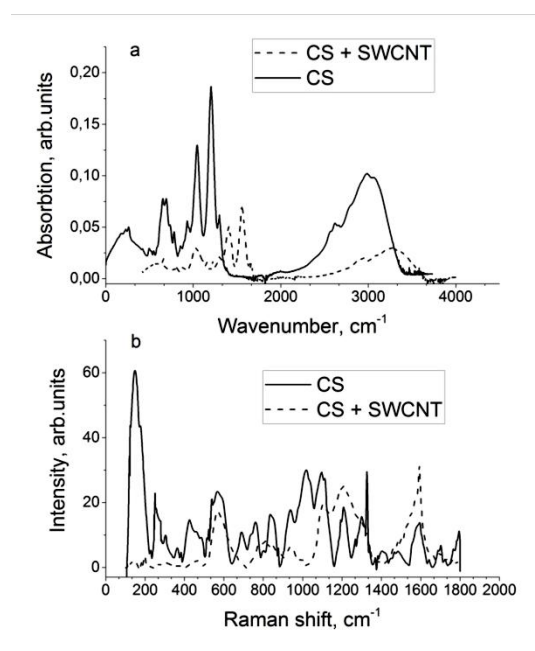


Figure 2: IR (a) and Raman (b) spectra of pure chitosan succinate and with addition of CNTs

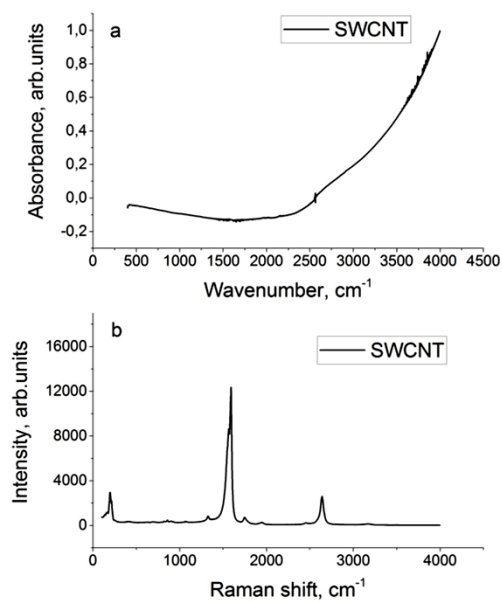


Figure 3: IR (a) and Raman (b) spectra of SWCNTs

Discussion

For the study water dispersions of chitosan and dispersion of chitosan with carbon nanotubes were made. To investigate the properties of materials obtained from these dispersions, film samples were obtained by evaporating the aqueous component under the influence of laser radiation. Based on the results of the study using IR spectroscopy and Raman spectroscopy, it was found that changes in the structure of a sample based on chitosan and SWCNT occurred due to the appearance of intermolecular bonds. It was found that a higher degree of acetylation of CS leads to its more homogeneous dissolution, while EC is prone to gelling. The addition of carbon nanotubes is due to an increase in the hardness of the resulting samples.

Conclusions

Thus, the conducted researches are useful for manufacturing of three-dimensional cellular and tissue engineering designs used for restoration of defects of cardiovascular system.

The work was supported by the Ministry of Education and Science of the Russian Federation (Agreement 14.578.21.0234 RFMEFI57817X0234).

References

- [1] H. Hong, et al. Fabrication of a novel hybrid heart valve leaflet for tissue engineering: an in vitro study. *Artificial organs*, 33(7):554-558, 2009.
- [2] S. Catros, et al. Laser-assisted bioprinting for creating on-demand patterns of human osteoprogenitor cells and nanohydroxyapatite. *Biofabrication*, 3(2):025001, 2011.
- [3] P. V. Popryadukhin, et al. Composite materials based on chitosan and montmorillonite: prospects for use as a matrix for cultivation of stem and regenerative cells. *Cell and Tissue Biology*, 6(1):82-88, 2012.

- [4] P. Matteini, F. Ratto, F. Rossi, S. Centi, L. Dei, R. Pini. Chitosan films doped with gold nanorods as laser-activatable hybrid bioadhesives. *Advanced Materials*, 22(38):4313-4316, 2010.
- [5] M.D. Dozois, L.C. Bahlmann, Y. Zilberman, X.S. Tang. Carbon nanomaterial-enhanced scaffolds for the creation of cardiac tissue constructs: A new frontier in cardiac tissue engineering. *Carbon*, 120:338-349, 2017.

Piezoelectric properties of PVDF and PVDF-TrFE electrospun materials for nerve regeneration

F. Al Halabi¹, O. Gryshkov¹, A. I. Kuhn¹, V. M. Kapralova², B. Glasmacher¹

¹Institute for Multiphase Processes, Leibniz Universität Hannover, Callinstrasse 36, Hannover, Germany

²Higher School of Applied Physics and Space Technologies, Peter the Great Saint-Petersburg Polytechnic University, Polytechnicheskaja str. 29, Saint-Petersburg, Russian Federation

Contact: alhalabi@imp.uni-hannover.de, gryshkov@imp.uni-hannover.de

Introduction

Traumatic injuries and loss of functionality in peripheral nerves often lead to life-long physical restrictions. Currently, the tension-free reconstruction of longer nerve defects applying autologous nerve grafts is a gold standard in nervous tissue repair. However, the main disadvantage of this method - the complete loss of function of the donor nerve - has encouraged the scientific community to develop new tissue-engineered nerve conduits. Biosynthetic nerve guides with innovative material properties could offer alternatives to the available on the market tubular implants with very variable regeneration success. Among materials for designing of artificial nerve conduits, the ones with inherent piezoelectric properties are of high interest. Because of their proven biocompatibility, stimulation of cell ingrowth and piezoelectric properties [1, 2], polyvinylidene fluoride (PVDF) and trifluoroethylene (PVDF-TrFE) are promising materials for designing active implants for nerve regeneration. It is believed that the regeneration of severed nerves could be accelerated by these properties. The current work is based on our previous study [3] and aims to develop a measuring method to describe the electro-mechanical coupling parameter, so-called the piezoelectric module.

Materials and Methods

Preparation of materials for testing: The polyvinylidene fluoride and its copolymer polyvinylidene fluoride-co-trifluoroethylene were used as received without any purification. To prepare the polymer solutions, PVDF (Sigma-Aldrich, MW ~ 530,000 Da) and PVDF-TrFE (Piezotech Arkema, weight ratio 70/30, MW ~ 450,000 Da) were dissolved in N.-Dimethylformamide (DMF) (Fluka Analytical) and acetone (AppliChem GmbH) in a weight ratio of 6:4. For the identification of favorable conditions for production of scaffolds, the solutions with PVDF concentrations of 10%, 15% and 20% as well as PVDF-TrFE of 10%, 15% and 20% were prepared at 50 °C and stored at room temperature overnight prior to electrospinning.

Electrospinning of solutions: The indicated above solutions were processed by means of electrospinning to form scaffolds (fiber mats) [4, 5]. With this method, fiber mats with different polymer mass contents were produced. The focus of the selected manufacturing process was to attain the most mechanically stable fiber mats possible. For this purpose, a preliminary study of the manufacturing parameters was carried out (data not shown). In the electrospinning process, a flow rate of 2 ml/h and voltages of 20-30

kV were applied as optimal process parameters to produce aligned fibers on a rotating aluminum cylindrical collector (300 rpm). The electrospinning time for each sample was 2.5 hours.

FTIR analysis: The Fourier Transform Infrared Spectroscopy (FTIR) was used to record the infrared spectra of the electrospun scaffolds. The spectra were compared to those of untreated/raw materials with respect to the presence of the nonpolar α - and piezoelectric crystalline β -phase. The FTIR spectra were recorded using a PerkinElmer 100 FTIR spectrometer (PerkinElmer, Norwalk, CT, USA) equipped with a triglycine sulfate detector and an attenuated total reflection accessory with a diamond/ZnSe crystal. The acquisition parameters were the following: 4 cm⁻¹ resolution, 8 co-added interferograms, and 4000–550 cm⁻¹ wavenumber range. An automatic CO₂/H₂O vapor correction algorithm was used during recording of the spectra. Spectra analysis and display were carried out using PerkinElmer software.

Measurements using the impact press machine: The developed method is based on the direct piezoelectric effect. For this, the fiber mats were mechanically stressed using the modified impact stress machine (fig. 1) and their induced electrical value was measured.

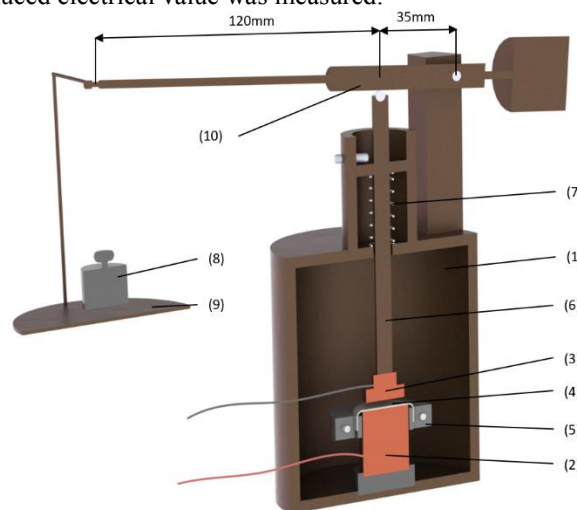


Figure 1: Section of the structure of the impact press machine: (1) measuring cell, (2, 3) electrodes, (4) test sample, (5) clamping device, (6) pressure rod, (7) spring, (8) applied weight, (9) shell, (10) lever

The measuring cell (1) is a closed shell of steel. Due to the influence in the electrical conductor, this shields the measurement against electromagnetic interference (Faraday cage). The lower electrode (2) is located in the meas-

uring cell on a polymer base which is insulated from the measuring chamber. The sample (4) is positioned in a clamping device (5) between the lower and the upper electrode (3). This consists of two rings between which the sample is clamped. The clamping device together with the sample is placed on the lower electrode, so that only the sample is in contact with the electrode surface. Due to the weight of the rings, the sample is evenly stretched over the electrode surface (fig. 2).



Figure 2: Sample without (left) and with the clamping device (right)

The upper electrode is connected to a rod (6), which projects from the measuring cell. The rod is held in position by a spring (7). On the tip of the rod there is a ball, which applies pressure uniformly to the rod and thus to the sample. The mechanical load is applied by means of a lever (10) via a weight (8), which is positioned in a shell (9). The electrodes from the measuring cell were connected to the voltage meter (610C, Keithley Instruments) during loading and unloading. The generated voltage measurement signal was then passed on to the oscilloscope (K8031, Velleman), digitized and graphically displayed on a computer via software. For capacitance measurement, the electrodes were connected to the capacitance meter (E7-20, MNIPI) in the loaded state of the sample after the voltage signal had been decayed.

The measuring principle is based on the direct piezoelectric effect. During mechanical compression of the sample, a voltage difference can be measured on the surfaces. For the determination of the piezoelectric module, the capacitance of the sample C_p must be known. Afterwards, the module d_{33} can be calculated with the following equation:

$$d_{33} = \frac{Q}{F} = \frac{w \cdot U \cdot C_p}{W \cdot F} \quad (1)$$

where Q : induced charge in C, F : impact force in N, U : induced voltage in V, C : electric capacitance in F, w : area of the mechanical load in cm^2 , W : area of the electrodes in cm^2 .

Performing measurements: The samples were fixed in the clamping device and placed on the lower electrode in the measuring cell. The measuring cell was then closed and the pressure rod adjusted so that the upper electrode did not make contact with the sample during resting. A set of weights m_{app} of 48g, 99g, 170g and 363g was used to apply the pressure load on the sample. Considering the weight of the pressure rod (m_{rod}), the upper electrode ($m_{electrode}$), the pressure compensation by the tensioning energy of the spring (m_{spring}), the conversion factor from the arm ratio of the lever (l) and the gravitational acceleration (g), the actual acting force (F_{app}) applied on the sample can be calculated as follows:

$$F_{app} = (m_{app} - m_{rod} - m_{electrode} + m_{spring}) \cdot l \cdot g = (m_{app} - 40g) \cdot \frac{120\text{mm} + 35\text{mm}}{35\text{mm}} \cdot 9,81 \frac{\text{m}}{\text{s}^2} \quad (2)$$

Both the weight of the rod and the electrode as well as the pressure compensation of the spring were approximated with 40g since the contact between the upper electrode and the sample is ensured only at a weight of 40g in the shell. Tab. 1 shows the applied weights (m_{app}) in the shell and the forces (F_{app}) acting on the sample.

Table 1: Applied weights in the shell and the corresponding force on the sample

m_{app}	48 g	99 g	170 g	363 g
F_{app}	0,3 N	2,56 N	5,65 N	14,02 N

For the determination of the piezo modulus d_{33} , the voltage potentials at the surfaces and the capacitance of the samples were measured during the applied force on the sample. Fig. 3 shows the equivalent circuit diagram for the voltage measurement of the examined piezoelectric samples.

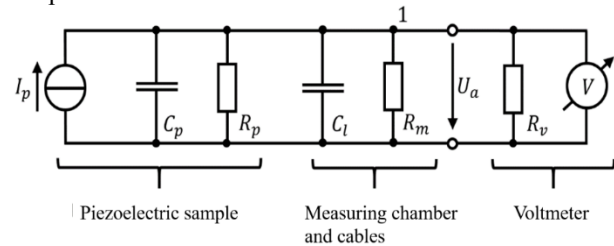


Figure 3: Electrical equivalent circuit diagram of the voltage measurement of the piezoelectric sample

In measuring the capacitance, the total capacitance (C_{tot}) has been recorded in the connected component. This included the capacitance of the sample (C_p) and the parasitic capacitance of the cables (C_l) (fig. 3). The capacitances were connected in parallel in this measurement setup. Thus, the total capacitance (C_{tot}) can be calculated using the following equation:

$$C_{tot} = C_p + C_l \quad (3)$$

Results

Effect of polymer concentration on the crystalline β -phase: Preliminary experiments showed that 10% PVDF solution resulted in generation of fiber mats with the presence of undesired beads. For this reason, this concentration of PVDF was not taken into consideration for further investigations. The study investigated the influence of the polymer concentration on the transformation process of the crystals from α - to the piezoelectric β -phase during electrospinning.

In fig. 4, the normalized FTIR absorption spectra of electrospun fiber mats from 15% and 20% PVDF polymer solution are compared with the spectrum of raw PVDF pellet. The analysis of FTIR data demonstrates that the spectra of both fiber mats from 15% and 20% PVDF solutions do not contain peaks at 796 cm^{-1} , 976 cm^{-1} and 1383 cm^{-1} of the α -phase, as compared to the raw pellet. The characteristic peaks at 840 cm^{-1} and 1275 cm^{-1} of the β -

phase have approximately the same intensity for both fiber mats.

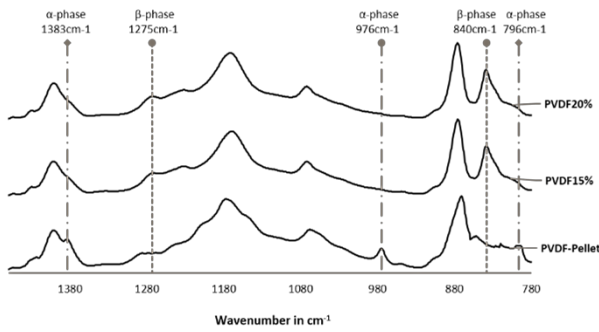


Figure 4: Normalized FTIR spectra of the raw PVDF pellet and PVDF fiber mat made of 15% and 20% polymer concentration in a DMF/acetone (6/4 ratio) solvent

Fig. 5 shows the unprocessed PVDF-TrFE powder as well as fiber mats made of 10%, 15% and 20% PVDF-TrFE solutions by means of electrospinning. In contrast to the PVDF, in which the crystals are converted into the piezoelectric β crystal phase during the electrospinning process, the PVDF-TrFE powder shows the characteristic peaks of the piezoelectric β -phase at 850 cm^{-1} , 1288 cm^{-1} und 1400 cm^{-1} [7]. Thus, the PVDF-TrFE, theoretically, does not require transformation processes for the conversion of crystallites into the β -phase. Furthermore, the three PVDF-TrFE fiber mats show nearly identical peaks at the β -phase-wavelengths.

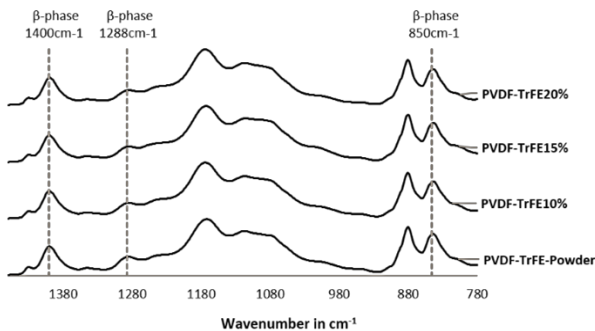


Figure 5: Normalized FTIR spectra of the raw PVDF-TrFE powder and PVDF-TrFE fiber mats made of 10%, 15% and 20% polymer concentration in a DMF/acetone (6/4 ratio) solvent

Effect of polymer concentration on the crystalline β -phase: Five fiber mats per polymer concentration were examined. Each fiber mat was manually loaded and unloaded six times, yielding 60 measuring points for each concentration. The quasi-static frequency of the measuring cycle was 0.2 Hz. Fig. 6 and 7 show measured voltages and sample capacities, respectively. Taking into account the relationship $d_{33} = (U \cdot C)/F$, fig. 8 represents the equivalent piezo modulus d_{33} of the fiber mats produced.

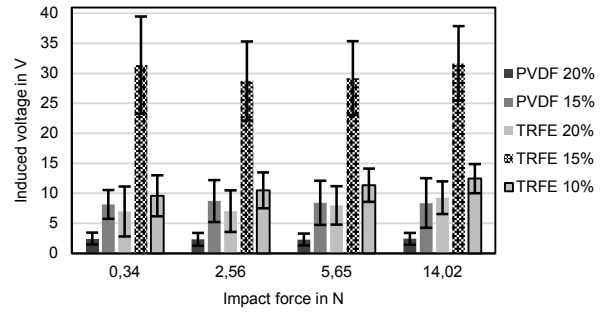


Figure 6: Measured voltages of PVDF and PVDF-TrFE fiber mats (n=6)

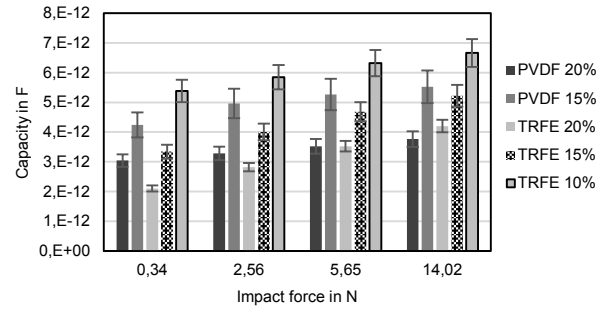


Figure 7: Measured capacities of PVDF and PVDF-TrFE fiber mats (n=6)

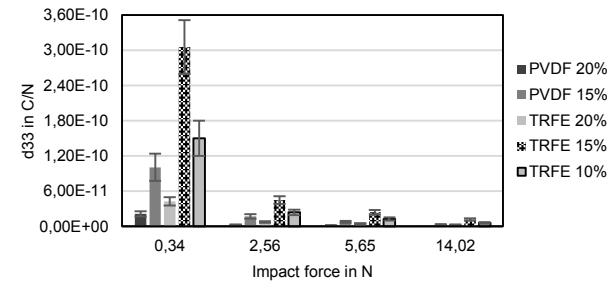


Figure 8: Piezoelectric module d_{33} of PVDF and PVDF-TrFE fiber mats (n=6).

Discussion

The piezomodule represents a geometry-independent parameter of a material, which is constant under different load profiles (by definition $d_{33} = Q/F$). If the piezomodule and the sample capacitance are known, the voltage induced at the sample surfaces during a load can be calculated with the relationship $U = (d_{33} \cdot F)/C$.

The structural transformation of α -phase into β -phase for PVDF was confirmed using FTIR analysis. This effect can be attributed to elongation of fibers during deposition onto grounded collector and simultaneous evaporation of DMF/acetone, which in turn affects orientation of dipole moments in the final PVDF electrospun fiber mat material.

For the piezoelectric investigation of the electro-spun fibrous mats from PVDF and PVDF-TrFE, an impact press machine was developed. In this method, the sample capacitance and the induced voltage were measured and then the induced charge was calculated. In order to reduce the measurement inaccuracies, the measuring charge was processed by a measuring amplifier (self-developed), taking into account the time behavior of the signal. The

measurement results showed a dependence of the piezoelectric modulus on the load, load frequency and fiber mat thickness. This behavior is due to the nonlinear viscoelasticity of the fiber mats. Since the piezoelectric modulus of the fiber mats did not behave uniformly under different load profiles, it is not possible to predict the induced voltage at a certain load.

The electrical response to a specific load profile must therefore be examined individually for different fiber mat geometries. For error-free detection of the induced voltage, a surface-covering contact between the sample surface and the measuring electrodes must be ensured. This can be performed using spinning conducting electrodes from the piezoelectric polymer and graphene oxide, as indicated elsewhere [8]. In addition, for a reproducible production of certain fiber mat geometries, a complete control of the electrospinning process has to be considered.

Conclusions

The aim of this work was to develop a measuring method to describe the electro-mechanical coupling parameter, so called piezoelectric module. The developed method is based on the direct piezoelectric effect. For this, the fiber mats were mechanically stressed and their induced electrical values were subsequently measured. In order to do this, a purely mechanical test cell for static measuring conditions was first constructed. However, the non-conductive surface structure of the fiber mats as well as the time response of the measuring signal were not considered. The measurement process on all fiber mats using the piezo module showed the same influence of the load and load frequency. As the load increased, the piezo module was reduced. Additionally, the increase in the load frequency led to an increase of the piezoelectric module. This behavior is attributed to the non-linear viscoelastic compliance of the fiber mats.

References

- [1] H. Kawai. The Piezoelectricity of Poly (vinylidene Fluoride). *Japan J Appl Phys*, 8: 975-976, 1969.
- [2] S.A.M. Tofail and J. Bauer. *Electrically Active Materials for Medical Devices*. World Scientific Publishing Company 2016.
- [3] F. AL Halabi, L. Freund, A. Repanas, P. Behrens, S. Knigge, K. Haastert-Talini, B. Glasmacher. Effect of different solvents on morphology and properties of piezoelectric PVDF scaffolds for nerve regeneration. *Biomedical Engineering*, 60(S1), 2015, doi: 10.1515/bmt-2015-5000.
- [4] S. Ramakrishna. *An introduction to electrospinning and nanofibers*. World Scientific 2005.
- [5] J. Doshi and D.H. Reneker. Electrospinning process and applications of electrospun fibers. *J Electrostatics*, 35(2-3): 151-160, 1995.
- [6] A. Szentivanyi, T. Chakradeo, H. Zernetsch, B. Glasmacher. Electrospun cellular microenvironments. Understanding controlled release and scaffold structure. *Adv Drug Deliv Rev*, 63(4-5): 209-220, 2011.
- [7] D. Mao, B.E. Gnade and M.A. Quevedo-Lopez. Ferroelectric Properties and Polarization Switching Kinetic of Poly

(vinylidene fluoride-trifluoroethylene) Copolymer. In M. Lallart, editor, *Ferroelectrics - Physical Effects*, chapter 4, 2011, ISBN 978-953-307-453-5, doi: 10.5772/17147.

- [8] B. Li, F. Zhang, S. Guan, J. Zheng, C. Xu. Wearable piezoelectric device assembled by one-step continuous electrospinning. *J Mater Chem C*, 4(29): 6988-6995, 2016.

Acknowledgements

The authors acknowledge the DAAD Program Strategic Partnership with Peter the Great Saint-Petersburg Polytechnic University, Igor Katz for his excellent technical assistance as well as Prof. Dr. W.F Wolkers for assistance with FTIR experiments.

Copyright

We agree on non-exclusive transfer of copyright of our work.

Evaluation of the P300 parameters with photic stimulation

A.N. Dmitriev¹, S.I. Shchukin¹

¹Bauman Moscow State Technical University, Moscow, Russian Federation
Contact: dmitalexnic@gmail.com

Introduction

Modern rehabilitation methods for patients with musculoskeletal problems after stroke include the following: therapeutic physical training methods, massage, physiotherapy, high-tech methods, etc. [1] High-tech methods include: the creation of supportive and "stimulating" robotic devices, the use of virtual reality, transcranial magnetic stimulation and BCI is often used for rehabilitation tasks based on movement presentation [2, 3]. Currently, the use of BCI to control fingers movement based on the cognitive evoked potential (EP) P300 has been studied [4].

The purpose of this paper is to study the influence of spatial and temporal stimulation parameters on P300 detection.

Materials and Methods

Two volunteers have participated in experiment, the first one is a male at 23 years old and the second is a female at 22 years old. The volunteers had been placed in a comfortable armchair at a distance of 70 cm from square photic stimulation matrix (PSM). PSM consists of 9 LEDs with a 574 nm wavelength. The task for the participants was explained in detail, thus they had to follow certain target stimuli (TS). The TS number corresponded to the diode position in the PSM (Fig. 1). The spatial interval was equal as:

$$X = \arctg(Xf/D) \quad (1)$$

Where Xf is the actual size between nearest LEDs in PSM (for each matrix interval is 1 cm, 2 cm and 3 cm relatively), D – distance between volunteers and PSM.

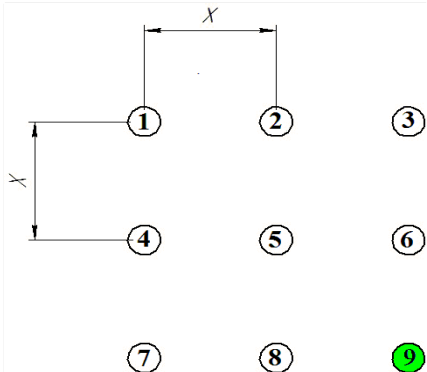


Figure 1: Scheme of PSM, «X» is spatial interval with nearest LED in PSM. LED with number «9» was highlighted

The experiment consisted of 6 experimental series (ES) for the first volunteers and 3 for the second (Table 1). Each experimental series consisted of 3 alternations of stimulation and relaxation intervals (Figure 2).

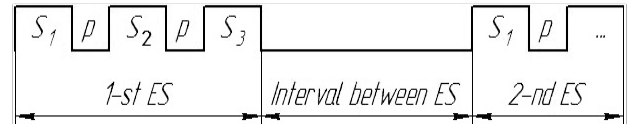


Figure 2: Time diagram of photic stimulation. S_i – interval stimulation in experimental series, i – serial number of TS, p – pause between stimulation probes S_{i+1} and S_i

Photic stimulation was performed using the oddball paradigm [5]. TS was given once in a 9 stimuli series, the rest were non-target stimuli (NTS). Thus, in a 9 stimuli series, each LED in the PSM was highlighted [6].

The volunteers should mentally count the number of TS highlights during stimulation, the stimulation follows by a 20 second rest (Figure 2) in which the subject had reported the TS counted number. Then the subject again counted the number of TS, so the procedure was repeated 3 times (3 numbers were counted).

After that, the stimulation parameters such as stimulation frequency, PSM size, and stimulation time were varied and the following experimental series was performed (see Table 1).

Table 1: Experimental procedures

Experimental procedure 1						
Number of stimulation mode	1A	1B	1C	1D	1E	1F
Numbers of TS	9,1,1	9,1,1	9,1,1	9,1,1	9,1,1	9,1,1
Frequency, Hz	1	5	3	5	1	5
Time, s	200	50	100	50	200	50
Spatial interval in PSM, °	2.4	2.4	1.6	1.6	1.6	0.8
Experimental procedure 2						
Number of stimulation mode	2A		2B		2C	
Numbers of TS	1,1,2		1,1,2		1,1,2	
Frequency, Hz	1		3		1	
Time, s	200		100		200	
Spatial interval in PSM, °	2.4		2.4		1.6	

Electrodes are placed according to the international system "10-20", ipsilateral ear electrodes were used as reference electrode; the earth electrode was installed on one cm above the nasion.

The EEG recording was performed using "Neuron-Spectrum-5". The sampling frequency is 500 Hz, the signal was filtered in the frequency band from 0.7 to 35 Hz. The electrode-skin impedance was measured at the beginning of the experiment and it was checked that electrode-skin impedance did not exceed 20 kΩ during the experiment. Table 2 shows the detailed parameters of the experiment.

Table 2: Parameters of experiment

	Conditions for 1-st subject	Conditions for 2-nd subject
Sound noise level, dB	50	45
Illumination of the room, lux	570	570
Experimental procedure	1	2
Room temperature, °C	24	24

Matlab R2011b software was used for experimental data processing. The coherent averaging method was used with an analysis period of 500 ms. for obtaining the EP.

Results

Figure 3 shows the graphs of typical EP in stimulation mode 1A. The signal 9 shows the EP response to TS. A positive peak is observed with amplitude in the order of 12 μV in the 350 ms region. The signal amplitude in response to the NTS in the region from 300 to 400 ms has not exceeded the value of 7 μV.

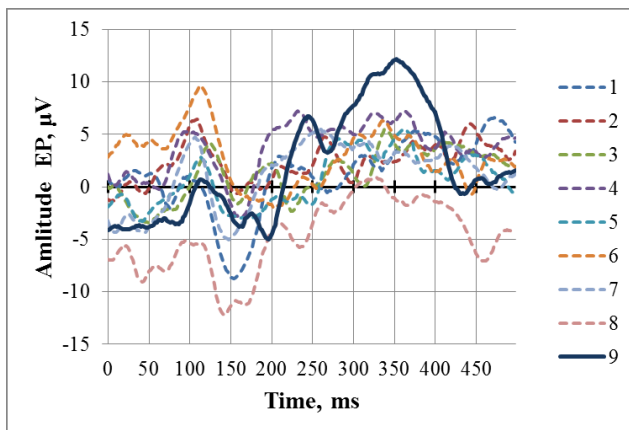


Figure 3: Typical EPs in PzA1 lead of photic stimulation. 1,2,3,4,5,6,7,8 – EPs response of number NTS, 9 – EP response of TS. Number of analyzed EEG epoch is 21 for average

Figure 4 shows the EP in stimulation mode 1B. The graphs have oscillations form. The EP on the TS is not significantly different from the response to the NTS.

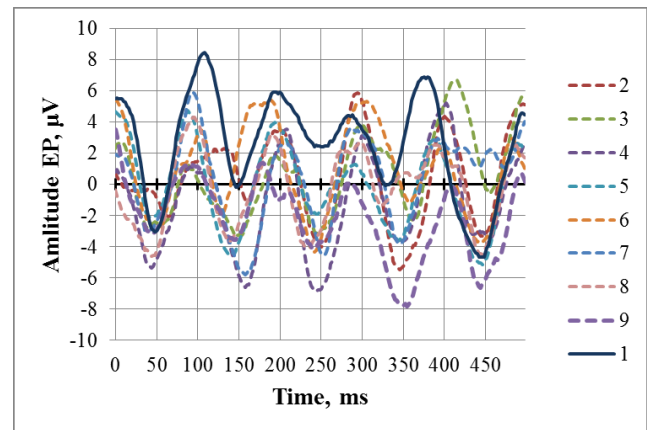


Figure 4: EPs in PzA1 lead of photic stimulation with 5 Hz frequency. 2,3,4,5,6,7,8,9 – EPs response of number NTS, 1 – EP response of TS. Number of analyzed EEG epoch is 27 for average

Based on the results of the experimental studies, the amplitudes and latencies of the EP P300, EP amplitudes in response to NTS were obtained under different stimulation modes (Table 3). The EP amplitude was defined as the maximum value of signal in the region from 300 to 400 ms. The average difference between the amplitudes of P300 and EP on the NTS is as follows:

$$\Delta A = \sum_{i=1}^N (A_{P300}^i - A_{EP}^i) \quad (2)$$

where N is the number of stimulations in the experimental series ($N = 3$), i – is the sequence number of the stimulation in experimental series, A_{P300}^i – is the amplitude of P300 for the i -th stimulation, A_{EP}^i – is the maximum amplitude of EP for the i -th stimulation in the time window from 300 up to 400 ms, $f(A_{P300}^i, A_{EP}^i)$ – is the amplitude difference function, equal to:

$$f(A_{P300}^i, A_{EP}^i) = \begin{cases} \dots \end{cases} \quad (3)$$

Table 3: Experimental results with two subjects

N	Amplitude P300, μV	Latency P300, ms	Amplitude EPs, μV	Stimulation mode	μV
Subject 1					
1	12	354	7	1A	6,3
2	17	370	10		
3	17	372	10		
4	11	308	6	1B	3,7
5	7	382	7		
6	10	378	4		
7	8	348	2	1C	5,7
8	11	372	5		
9	8	390	3		
10	10	376	3	1D	2,3
11	4	370	5		
12	4	368	5		
13	15	338	8	1E	7,7
14	15	374	10		
15	20	368	9		
16	11	302	5	1F	4,3
17	9	302	5		
18	8	304	5		
Subject 2					
1	9	372	4	2A	3,7
2	7	362	4		
3	7	370	4		
4	1	386	2	2B	0,7
5	4	382	2		
6	2	282	4		
7	5	356	4	2C	1
8	2	390	5		
9	5	300	3		

The P300 was detected if its amplitude was greater than the EP amplitude on the NTS. Based on the values of Table 3, P300 detection dependencies for different stimulation modes were plotted (Figures 5 and 6).

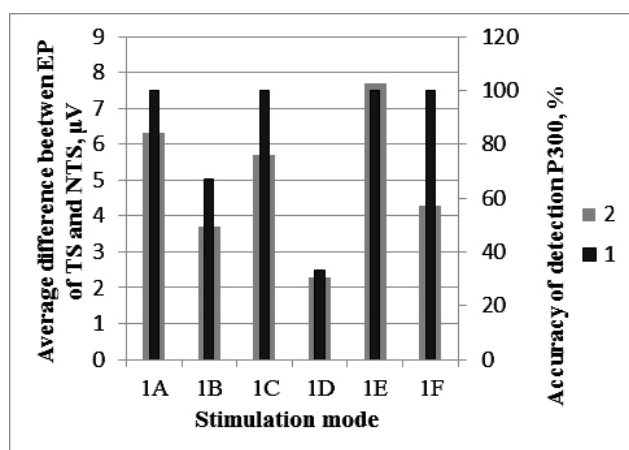


Figure 5: Evaluate of P300 detection with different stimulation mode for subject 1. 1 – The accuracy of P300 detection, 2 – The amplitude average difference value in different stimulation mode

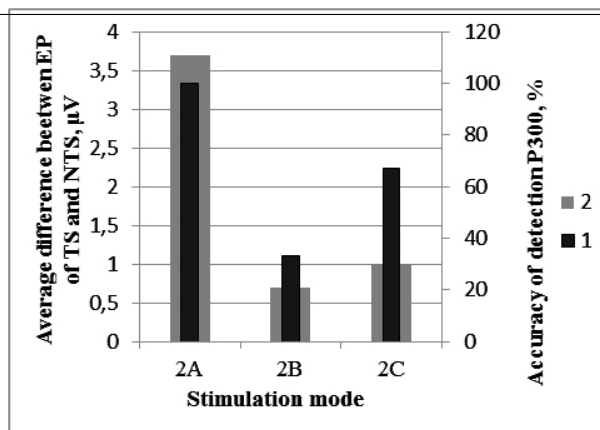


Figure 6: Evaluate of P300 detection with different stimulation mode for subject 2. 1 – The accuracy of P300 detection, 2 – The amplitude average difference value in different stimulation mode

Discussion

One of the most important stimulation parameters during P300 registration is the photic stimulation frequency. Figure 3 shows the typical EP. The graph shows the main peak, which corresponds to P300 presence in response to TS. The visual EP (VEPs) P100 and N145 are also presented on the graph. This EP form is typical for a photic stimulation with 1 Hz frequency. The P300 amplitude varies from 12 to 20 μV and the latency is approximately 360-370 ms.

The photic stimulation frequency increasing to 3 Hz leads the P300 amplitude to decrease and the latency variability to increases. However, the accuracy of P300 determination was not decreased for the first volunteer (Figure 5).

The photic stimulation frequency increasing to 5 Hz leads to the occurrence of oscillations with a 10 Hz frequency and an amplitude in the order of 7 μV . These oscillations are superimposed on the EP P300 and can mask it. The reason of these oscillations is associated with the appearance of steady-state VEPs with photic stimulation frequency increasing, which corresponds to the results of previous work [6]. Against the background of VEPs, the amplitude of P300 decreases and varies in the range from 4 to 11 μV , which in turn affects the P300 detection.

As for the second volunteer, EP P300 had a slightly smaller amplitude from 7 to 9 μV at a stimulation rate of 1 Hz. However, even a slight change in the stimulation modes (an increase in the frequency to 3 Hz or a decrease in spatial interval) significantly reduced the amplitude of P300 (Table 3). As a result, the detection accuracy of P300 decreased (Figure 6). Such a decrease in the P300 amplitude can be associated with fatigue and loss of attention concentration. Therefore, to take an objective account of the involvement degree of patient during study, additional independent measurements must be carried out. Spatial interval with photic stimulation frequencies of 1 and 3 Hz did not affect the accuracy of P300 determination. The amplitudes of VEPs and P300 were approximately in the same values range.

In previous work [6] it was shown that the spatial interval influence on the P300 detection in a 5 Hz photic stimulation and it was assumed that a decrease in spatial interval reduces the accuracy of P300 determination. However, based on the results of current experimental studies, it was found that at 5 Hz photic stimulation, the P300 recognition accuracy for spatial interval 2.4 °, 1.6 ° and 0.8 ° was 67%, 33% and 100%, respectively.

Thus, the spatial interval influence on the accuracy of P300 detection is more complex.

Conclusions

It was shown that the accuracy of the EP P300 amplitude decreases and the latency becomes more variable during a 5 Hz frequency photic stimulation. The most stable high-amplitude P300 signals were allocated at 1 Hz photic stimulation. At spatial interval in the PSM, on the one hand, the amplitude of P300 increases, while the amplitude of the VEPs that can mask the signal increases in the other hand. During P300 registration, it is important to monitor the concentration of patient's attention within the limit of cognitive task performing.

References

- [1] O.A. Mokienko, N.A. Suponeva, G.A. Asiatskaya, A.S. Klotchkow etc. Clinical recommendation «Stroke in adult: central paresis of upper limb". Rehabilitation specialist's union of Russia, Moscow, 2017.
- [2] O.A. Mokienko, P.D. Bobrov, L.A. Chernikova, A.A. Frolov. Based on motor imagery brain-computer interface for rehabilitation patients with hemiparesis, J Byulleten Siberian medicine, 12: 30-35, 2013.
- [3] K. K. Ang, C. Guan, K. Sui Geok Chua, B. T. Ang etc. Motor imagery BCI for upper limb stroke rehabilitation: an evaluation. IEEE International Conference on Engineering in Medicine and Biology Society(EMBC), Tokio, 261 –264, 2017.
- [4] A.Ya. Kaplan, D.D. Zhigul'skaya, D.A. Kirjanov. Research the possibility single fingers of human phantom arm management in brain computer-interface circuit. J Russian State Medical University messenger, Moscow, 2: 26-30, 2017.
- [5] V.V. Gnezditsky. Vyzvannye potentsialy v klinicheskoy praktike. TRTU, Taganrog, 1997.
- [6] A.N. Dmitriev, I.K. Sergeev, S.I. Shchukin. Evaluation influence spatial distance between photostimulation's on detection P300. J Biomedicinskaya radioelektronika, 9: 19-22, 2017.

Telephone call management in the cognitive operating room

N. Kohn¹, D. Ostler¹, S. Koller¹, N. Marahrens¹, N. Samm^{1,2}, M. Kranzfelder^{1,2}, T. Vogel^{1,2}, D. Wilhelm^{1,2},
H. Feußner^{1,2}

¹Forschungsgruppe MITI, Klinikum rechts der Isar der TU München, Trogerstraße 26, 81675, München, Germany

²Klinik und Poliklinik für Chirurgie, Klinikum rechts der Isar der TU München, Ismaninger Straße 22, 81675 München, Germany

Contact: nils.kohn@tum.de

Introduction

Mobile phones increase the reachability of surgeons and health care providers, thus facilitating decisions making and improving patient care [1,2]. Accordingly, phones are regularly taken into the operating room (OR).

On the other hand, any intraoperative interruption increases the workload and may lead to a negative influence on the outcome [3,4]. Incoming telephone calls are responsible for as much as 1/4 of all disturbing intraoperative events [5]. To avoid this type of interruption, strict interdiction of telephone calls could be a simple and effective means. However the majority of incoming calls is not time-critical and not important, the lack of reachability could be detrimental in some cases. Accordingly, a complete elimination of mobile phones out of the OR is not an option.

To solve this problem, a situational aware system could be helpful which is able to discriminate between “important” calls and those which can easily be postponed. This paper discusses if a cognitive OR system could be used for a situation-adapted preselection of incoming telephone calls for the members of the surgical team.

Materials and Methods

Cognitive OR

In our “cognitive OR”, a central control and steering system is established, which collects a wide range of incoming information in real time [6]. Through “intelligent” interpretation of these data, based upon highly grained patient and surgical workflow models, the system is always aware of the actual situation and even capable to predict forthcoming events including the time left to the end of the surgery. In addition, it even classifies the actual state of the surgery according to “normal”, “irregular” or “critical”. The system described here is a middle ware between the person on the telephone and the surgeon addressed.

Call routing

Incoming calls for the surgeon (in our case to a DECT phone) are not directly forwarded to his phone. Instead the calls are routed to a call handler (Fig. 1). The call handler is provided by an Asterisk based VOIP server. This VOIP server directly interacts with the cognitive OR to get information about the current status of the surgery including the remaining duration. In addition, the central database is informed about incoming calls and is therefore

able to display these calls on a central information unit or create a list of missed calls after the operation is completed. The VOIP server is also able to distinguish between calls from within the hospital network and calls from outside.

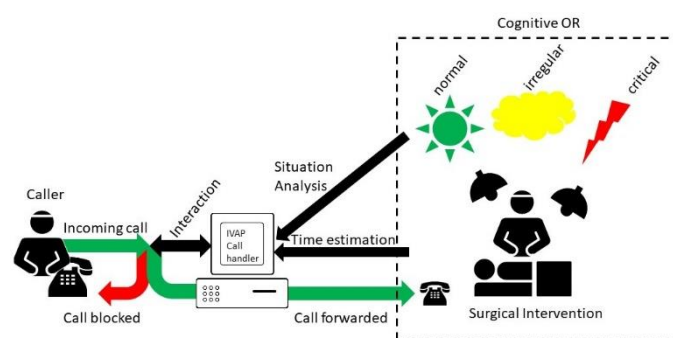


Figure 1: Call routing model

Caller interaction module

The decision whether the surgeon should be encountered with the call or not depends upon three different aspects:

- I) Significance of the request
- II) Actual surgical situation
- III) Time line

Many calls are neither time critical nor really important, but, of course, the system will be unable to classify the urgency of the call. This has to be left to the caller. The system, however, provides the necessary information to enable the caller to weigh up whether it is justified to contact the surgeon immediately or not.

- II) Actual surgical situation

The workload during a surgical operation varies. If it is a comparatively easy case and if everything is running smoothly, the surgeon should be more open to respond to a telephone call than under severe strain. The situational aware system is able to classify the workflow as either “normal” (green), “irregular” but not yet dangerous (yellow) or “critical” (red). Accordingly, answers A, B or C

are selected. The type of answer may vary in the course of the operation.

Accordingly, the caller will be informed as follows:

- A) "Dr. NN is currently doing a surgery which will probably be finished in ... minutes/hours. Nonetheless, you could be put through if required. In this case, please dial "2".

The threshold is, thus, comparatively low to contact the surgeon right now.

The next step is to make the caller a bit more hesitating to get connected:

- B) "Dr. NN is at the OR table at the moment. The surgery will last for another ... minutes/hours. Please, do not disturb unnecessarily. However, if your matter is urgent and cannot wait, please dial "2".

It is assumed that the caller rather refrains from being put through to the surgeon.

If the situation in the OR is really critical and any unnecessary distraction has to be avoided, the reply has to be very deliberate:

- C) "Dr. NN is currently doing a surgery. A call can only be accepted in vital cases. Can your call wait for another ... minutes/hours? Only if you are sure it cannot wait dial "2".

In this case, only really urgent calls should be connected.

III) Time line – estimated duration of the surgery

At the beginning of an operation it has to be expected that the surgeon will not be directly available on the phone for a considerable period of time. Accordingly, a better access should be granted to the caller as compared to later phases of the operation. If not determined otherwise, the system should routinely start with answer "A". After 2/3 of the estimated duration, the answer is automatically switched to "B". In any case, the caller will be informed about the expected duration of the operation.

Thus, the telephone management does not decide upon whether a caller is connected or not but it just modulates the threshold to contact the surgeon during the operation or not. To find out whether this method is effective in reducing the number of incoming calls without depriving the caller of the ability to reach the surgeon in critical cases, a study was conducted.

Survey

A list of different scenarios was presented to different healthcare providers of a surgical unit comprehending three different groups of matters of minor (class III), major (class II) or vital (class I) importance. Each test person was summoned up to call the respective doctor and got

either the answer A, B or C, each with 3 different time estimations (60, 30 or 15 min till the end of surgery). It was protocolled if he/she insisted about getting connected.

Class III scenarios:

1. A former patient visits the surgical floor and asks whether he could briefly see the doctor who had successfully done his surgery 3 weeks in order to express his thanks.
2. The administration calls and asks to transfer a message to the doctor which is not urgent but important.

Class II scenarios:

1. The relatives of a patient are just paying her a visit. Since the patient will be discharged within the next days, they would like to ask for the doctor to get information about the organization of the further care.
2. A patient waiting for her surgery which will take place in about 2 – 3 hours is very thirsty. It should be adequate to give her 500 or 1000 ml of saline

Class I scenarios

1. A patient with the signs of an acute secondary haemorrhage after a cholecystectomy
2. A patient with clear clinical signs of an acute pulmonary embolism

In addition, every test person was asked to judge upon the value of receiving the estimated time left till the end of the operation by using a modified Likert Scale (negligible=1 to very helpful=5). To test the overall acceptance of the system the same Likert Scale was used.

Results

A number of 46 different healthcare providers participated in the survey. The results show a clear correlation between the significance of the request and the number of calls passed through (Fig. 2). For a request of minor importance (class III) 99% of all test persons dispense with a connection of their call. Out of 414 calls only 4 calls were forwarded. For the scenario with a request of major importance (class II) 7% of all calls were forwarded to the surgeon (29 out of 414 calls), mostly in a normal OR situation. In case of a request of vital importance (class I) 78% of all test persons decided to be connect to the surgeon (324 out of 414 calls). The results of the Likert scale for the value of receiving the estimated time left till the end of the operation were 4.0 for a request of vital importance, 3.5 for major importance and 2.6 for minor importance. The remaining operation time only showed an influence to class I scenarios (Fig. 3). Most callers refrained from being put through for the case of 15 minutes remaining operation time (63%, 57 out of 90 blocked

calls). The overall acceptance of the system was resulted in a value of 3.5.

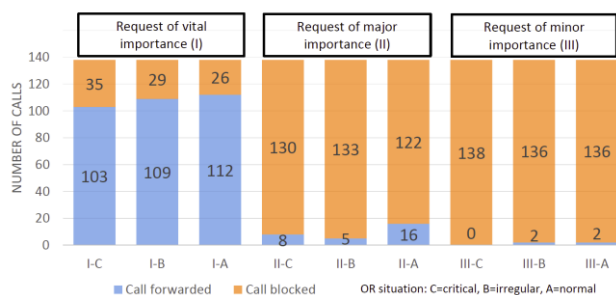


Figure 2: Calls blocked/forwarded by importance of the request and OR situation

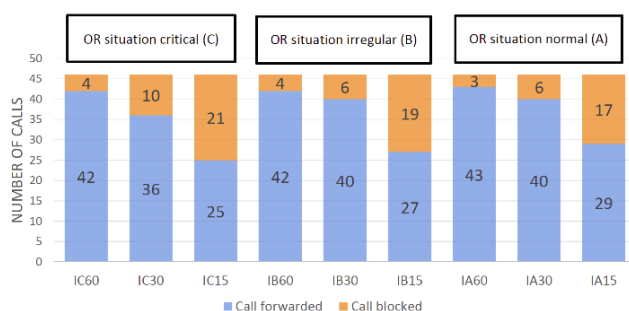


Figure 3: Calls blocked/forwarded in case of a vital request by OR situation and remaining time

Discussion

The result of the survey clearly shows the advantage of the telephone management system. Unnecessary calls (request of minor importance) can be blocked and the surgeon is not constantly interrupted during the surgery. On the other hand important calls are still forwarded into the OR. The definition of the three different thresholds in combination with the estimation of the time left till the end of the surgery deliver the caller a clear impression of the current situation in the OR. Not only the surgeon, but also the caller benefits from the system. The time estimation was considered very useful by the vast majority of the test persons. The estimation is an important hint for most callers to decide whether they want to be connect or not, especially in class I scenarios. The prognosis also avoids unnecessary further call attempts within the estimated time period.

Conclusions

In this paper we presented a concept for telephone call management within the OR. A survey under different healthcare providers showed a broad acceptance and the need for such a system. Telephone management in the OR has to potential to reduce unwanted interruption during surgeries as well as to reduce the workload of surgeons and nurses without blocking urgent or important calls. The next step is to adapt these findings and to evaluate the call management system under real surgical conditions.

References

- [1] Angarita, F. A., Strickland, M., Acuna, S. A. (2015). Incorporating smartphones into clinical practice. *Annals of Medicine and Surgery*, 4(2), 187.
- [2] Mentis, H. M., Chellali, A., Manser, K., Cao, C. G., Schwaizberg, S. D. (2016). A systematic review of the effect of distraction on surgeon performance: directions for operating room policy and surgical training. *Surgical endoscopy*, 30(5), 1713-1724.
- [3] Weigl, M., Stefan, P., Abhari, K., Wucherer, P., Fallavollita, P., Lazarovici, M., Catchpole, K. (2016). Intra-operative disruptions, surgeon's mental workload, and technical performance in a full-scale simulated procedure. *Surgical endoscopy*, 30(2), 559-566.
- [4] Arora, S., Sevdalis, N., Nestel, D., Woloshynowych, M., Darzi, A., Kneebone, R. (2010). The impact of stress on surgical performance: a systematic review of the literature. *Surgery*, 147(3), 318-330.
- [5] Weigl, M., Antoniadis, S., Chiapponi, C., Bruns, C., Sevdalis, N. (2015). The impact of intra-operative interruptions on surgeons' perceived workload: an observational study in elective general and orthopedic surgery. *Surgical endoscopy*, 29(1), 145-153.
- [6] Ostler, D., Kranzfelder, M., Stauder, R., Wilhelm, D., Feussner, H., & Schneider, A. (2015). A centralized data acquisition framework for operating theatres. In *E-health Networking, Application & Services (HealthCom), 2015 17th International Conference on* (pp. 1-5). IEEE.

Acknowledgements

This work was done with grant support by the Bavarian Research Foundation (BFS).

Translation Dynamics in Holistic Analysis of Functional Human-body System

J. Mau^{1,2}

¹Heinrich Heine University Düsseldorf, School of Medicine, Moorenstr. 5, Düsseldorf, Germany

²iqmeth Privates Institut für Quantitative Methodik, Buschstr. 5, Krefeld, Germany

Contact: j.mau@hhu.de

Introduction

The core tenet in system fault diagnostics is that behavior of the whole emerges from activity of functional components and coordination of their interaction. This motivates a *drill-down* approach in functional analysis of complex systems [1, 2].

Manned spacecraft, aircraft carriers, submarines, and the socio-biological system of human body with person's actions all impress by their complexity of interwoven detail as soon as one can look behind their encasement, and full comprehension of functional structures and of output in response to stimuli input will often seem impossible. A systematic approach may then start from construction principles that let the apparatus fulfill its mission: for example, components that allow the plane to fly (wings, propulsion), to take off and to land (wheels), and to carry goods and passengers (cabin). Next, the set of vital prerequisites, as energy supply, wiring, cabin air, to mention a few. Finally, all equipment, including human operators, to pilot the plane's operations – have orientation, decide on direction, and interact with outside world. Apart from disrupted material integrity of whole plane, review of these items for clues is witnessed, for example whenever an Airbus or Boeing disappears on a scheduled passenger flight over the oceans. Speculating about malfunction of said *productivity* sub-systems, *vital functions* sub-systems, *operational functions* sub-systems illustrates a scaling understanding that is equally seen in a doctor's scrutinizing first view of a patient as totality of person 'encased' in body system before deciding on an entry point for diagnostic work-up.

Definition 1 *Highly complex systems intended by design for purposeful action are called production systems.*

Principle 1 *Production systems share a tri-partite functional decomposition of their ensemble, the Whole, into vital functions, productivity functions, and operational functions, referred to as *wirk-components*, meaning components for effectuation, in German more precisely *Komponenten des Bewirkens*.*

Corollary 1 *The tri-partite functional decomposition is then canonical among all production systems.*

The decomposition is exhaustive and non-overlapping. Its components are referred to as *canonical wirk-components*.

Principle 2 *At any moment, the behavioral activity of the Whole is a complete translation of interaction between its three canonical *wirk-components* and their functional properties currently prevailing.*

These principles are to apply throughout though systems differ substantially in material realization and in designated environment. The present exposition then describes an equally canonical *configuration of effectuation dynamics*, a *wirkgefüge* independent of its physical realization, that first energizes the cooperation of *canonical wirk-components* - the *logical units* at tri-partite "function-level no.1" - and then translates this to whole-body "function-level 0" aggregate dynamics.

The configuration of control couplings that permits the human body system to energize required action of its *canonical wirk-components* in any situation and that is conceptually equally independent of its material realization, is referred to as *schaltgefüge*, which is considered as the mission of *Wiener* [3]-sense "kybernetik" in [4]. By their independence of material realization, *axiomatic wirkgefüge* and *kybernetik schaltgefüge* then require each other, which explains the level of abstraction in the present exposition.

Materials and Methods

Prerequisites

The design of *axiomatic wirkgefüge* exploits intuitive concepts from electric direct-current circuits: tension (voltage), accumulated charge, capacity, resistance, supply and consumer power (wattage) demand, that are basic – not to suggest that physical electricity is actually involved.

Definition 2 *The axiomatic *wirkgefüge* consists of a ubiquitous source with potential difference (voltage) U_0 , and for every single logical unit, of a supply condenser of capacity C for buffer storage of supply charge $Q_s(t)$ by time t , a resistor with resistance $R_s(t)$ for passage control of supply current (amperage) $I_s(t)$ to said condenser, and of another condenser for charge consumption, conceived as a mirror of the supply-part condenser, with current voltage $U_c(t)$ generated by its current charge $Q_c(t)$ as source for the demand part, another resistor with resistance $R_d(t)$ for passage control of demand current (amperage) $I_d(t)$ to an end consumer with demand wattage $P_e(t)$.*

Principle 3 (Sluggishness) *The exposition focuses on almost instantaneous charge increments and decrements on supply and demand part condensers, respectively, in any incremental time interval $[t, t + dt]$, $t > 0$; accumulated charges Q are assumed continuous functions $(Q(t))_{t>0}$ with derivative $(I(t))_{t>0}$ everywhere. Voltages, resistances, wattages, however are assumed to lag behind, shown in their pre- t values, $U(t-)$, $R(t-)$, $P(t-)$. They can then be*

assumed to have currently fixed values during an arbitrarily small amount of time while accumulated charge on the condensers changes.

Remark 1 The concept of a “mirror” condenser is introduced for use in the postponed control regimen, in particular to control access to available supply charge.

Assumption 1 Ohm’s law and Kirchoff’s rules as known for direct electric current circuits do apply in the axiomatic wirkgefüge.

Remark 2 For human body system, source voltage may be thought of being generated by the cellular system, the body’s material base layer, while effectuation dynamics affect only the activity on function levels above the cellular system. That all functional activity is realized by ubiquitous living cells may ‘close the loop’ for the circuit.

Generic Single Circuit

The axiomatic wirkgefüge of Def. 2 applies; see Fig. 1 for illustration.

Single-circuit supply-part

Define the charge supply part through quadruple $[U_0, (R_s(t))_{t>0}, C, (Q_s(t))_{t\geq 0}]$. To determine supply current $I_s(t)$ explicitly, note that ohmic resistance $R_s(t)$ implies a voltage drop of $U_s^*(t) = R_s(t)I_s(t)$ that leaves an effective supply voltage $U_s(t)$ at the condenser of $U_s(t) = U_0 - U_s^*(t)$, that generates t -prevalent charge $Q_s(t)$ on the condenser through $Q_s(t) = CU_s(t)$. While $U_s(t) = U_0$ when $R_s(t) = 0$, $R_s(t) > 0$ permits re-arrangement such that $I_s(t) = U_0/R_s(t) - Q_s(t)/[CR_s(t)]$, and, by $dQ_s(t) = I_s(t)dt$, a supply-charge increment during $[t, t + dt]$ of

$$dQ_s(t) = \frac{U_0C - Q_s(t)}{CR_s(t)}dt \quad (1)$$

yields the first-order differential equation

$$U_0C = \dot{Q}_s(t)R_s(t)C + Q_s(t) \quad (2)$$

with $Q_s(0) = 0$. For constant resistance $R_s(t) \equiv R_s^* > 0$, a solution of (2) is

$$Q_s(t) = U_0C \left(1 - e^{-\frac{1}{R_s^*C}t} \right). \quad (3)$$

Single circuit demand-part

With Q_c differentiable, the quadruple

$$[(Q_c(t))_{t\geq 0}, C, (R_d(t))_{t>0}, (P_e(t))_{t>0}] \quad (4)$$

defines the charge demand part according to end-consumer power demand $P_e(t)$; demand-circuit current is $I_d(t) = \dot{Q}_c(t)$, voltage drop at demand-control resistor of resistance $R_d(t)$ then is $U_d(t) = R_d(t)\dot{Q}_c(t)$. With source voltage $U_c(t) = Q_c(t)/C$ for consumption according to t -prevalent condenser charge $Q_c(t)$, effective voltage $U_e(t)$ at

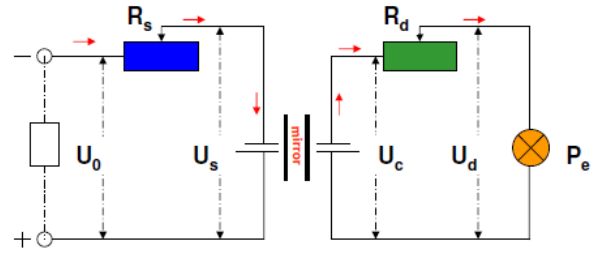


Figure 1: The motivation for the generic single-circuit according to Def. 2 is illustrated as if it were a pair of electric circuits.

the end consumer is then $U_e(t) = U_c(t) - U_d(t)$ with ohmic resistance $R_e(t) = U_e(t)/\dot{Q}_c(t)$ and power (wattage) $P_e(t)$, $P_e(t) = U_e(t)\dot{Q}_c(t)$, at any time $t > 0$. While $U_e(t) = U_c(t)$ when $R_d(t) = 0$, $R_d(t) > 0$ permits rearrangement that gives a first-order quadratic differential equation in Q_c ,

$$\dot{Q}_c^2(t) - \dot{Q}_c(t) \frac{Q_c(t)}{CR_d(t)} + \frac{P_e(t)}{R_d(t)} = 0, \quad (5)$$

which implies a decremental change in charge on the demand-part condenser. that depends on t -prevalent condenser charge $Q_c(t)$, end-consumer’s pre- t -power (wattage) demand $P_e(t)$, and pre- t demand-current control resistance $R_d(t)$, for a fixed capacity C .

When one absorbs the demand-control resistor’s and the end-consumer’s ohmic resistances into one resistor according to their serial connection, $R(t) = R_d(t) + R_e(t)$, one obtains the linear first-order differential equation in $Q_c(t)$,

$$\dot{Q}_c(t) = -\frac{Q_c(t)}{CR(t)}. \quad (6)$$

Results

A Triple Circuit

The triple-circuit wirkgefüge will have one copy of the generic single-circuit in Sect. ”Generic Single Circuit“ for each Wirkkomponente, set in a parallel connection which implies common source voltage U_0 for each while total current and moved charges split at the branching points into the partial circuits, see Fig. 2.

For each replication identified by a subscript i , for $i = 1, 2, 3$, one has (1) now as

$$dQ_{si}(t) = \frac{1}{R_{si}(t)C_i} (U_0C_i - Q_{si}(t))dt. \quad (7)$$

and (5) as

$$dQ_{ci}(t) = -\frac{Q_{ci}(t)dt}{C_iR_{ci}(t)} \quad (8)$$

$$\dot{Q}_{ci}(t)Q_{ci}(t) = R_{di}(t)C_i\dot{Q}_{ci}^2(t) + C_iP_{ei}(t). \quad (9)$$

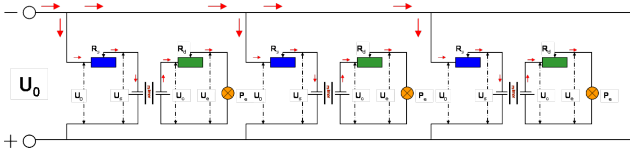


Figure 2: Schematic triple-circuit in parallel connection of three replicates of generic circuit in Fig. 1.

Up-scaling: triple- to single-circuit

For clarity of exposition, it is helpful to use superscripts FL0 and FL1 in order distinguish the appropriate function levels in notation, whenever both function levels are involved in a statement.

Up-scaling supply-parts

Here, it has to be shown that the configuration permits to re-obtain (2) from the triple in (7).

Capacities and t -prevalent charges on the three supply-part condensers add up as much as currents according to Kirchhoff's rule, $C_s = C_1 + C_2 + C_3$, $Q_s(t) = Q_{s1}(t) + Q_{s2}(t) + Q_{s3}(t)$, $I_s(t) = I_{s1}(t) + I_{s2}(t) + I_{s3}(t)$, while for supply-control resistances $((R_s)^{-1})(t) = R_{s1}^{-1}(t) + R_{s2}^{-1}(t) + R_{s3}^{-1}(t)$ holds.

Theorem 1 The FL1 triple-circuit supply-parts defined by

$$[C_i^{\text{FL1}}, Q_{si}^{\text{FL1}}(t), R_{si}^{\text{FL1}}(t)]_{i=1,2,3;t>0} \quad (10)$$

translate into a FL0 single-circuit supply-part

$$[C_s^{\text{FL0}}, Q_s^{\text{FL0}}(t), R_s^{\text{FL0}}(t)]_{t>0} \quad (11)$$

by summation of capacities, charges, and inverse resistances,

$$C_s^{\text{FL0}} = C_s^{\text{FL1}}, \quad (12)$$

$$Q_s^{\text{FL0}}(t) = Q_s^{\text{FL1}}(t), t > 0, \quad (13)$$

$$(R_s^{\text{FL0}})^{-1}(t) = (R_s^{\text{FL1}})^{-1}(t), t > 0. \quad (14)$$

Proof: Rewriting (7) for each i ,

$$dQ_{si}(t) = \frac{U_0}{R_{si}(t-)} - \frac{Q_{si}(t)dt}{R_{si}(t-)C_i} \quad (15)$$

and observing that $Q_{si}(t) = U_{si}(t)C_i$ for the supply-part condensers and $U_{si}(t-)/R_{si}(t-) = I_{si}(t)$, for every i , summation of (7) over $i = 1, 2, 3$ yields indeed

$$dQ_s(t) = \frac{1}{C_s} (R_s)^{-1}(t-)(U_0 C_s - Q_s(t)) dt \quad (16)$$

Up-scaling demand-parts.

It now has to be shown that the configuration permits to re-obtain (5) from the triple in (9), too.

Capacities C_i and t -prevalent charges $Q_{ci}(t)$ on the three demand-part (mirror) condensers, and end-consumers' power demands (wattages) $P_{ei}(t)$ are first added, $C_s =$

$C_1 + C_2 + C_3$, $Q_c(t) = Q_{c1}(t) + Q_{c2}(t) + Q_{c3}(t)$, and $P_e(t) = P_{e1}(t) + P_{e2}(t) + P_{e3}(t)$.

One then has to construct a demand-part circuit at FL0 with the desired properties that arise from summations across respective circuits at FL1. To organize the train of thought, a general lemma is helpful.

Lemma 1 For any single circuit with condenser of capacity C and t -prevalent charges $Q(t), t \geq 0$, and with a consumer of power demand $P(t), t \geq 0$, there exists a resistor of resistance $R(t), t \geq 0$, such that

$$R(t) = \frac{\frac{Q(t)}{C} - \frac{P(t)}{Q(t)}}{\dot{Q}(t)} \quad (17)$$

for any $t, \dot{Q}(t) > 0, t \geq 0$.

Proof: On the condenser, t -prevalent charges $Q(t)$ imply t -prevalent voltages $U(t)$ and $U(t) = Q(t)/C$ for any $t \geq 0$. Voltage drop $U_P(t)$ at t according to a t -prevalent power demand $P(t)$ is $U_P(t) = P(t)/\dot{Q}(t)$, for any $t \geq 0$. For any residual voltage $U(t) - U_P(t) \geq 0$, there is a resistor in the circuit which implies a voltage drop $U_R(t) = U(t) - U_P(t)$ at t ; its resistance $R(t)$ is then $R(t) = U_R(t)/\dot{Q}(t)$, for any $t \geq 0$. Together, these results prove the Lemma.

It remains to identify FL0 capacity, charges, powers from the FL1 triple-circuits summaries, first, and then to apply the Lemma in order to finalize the up-scaling.

Theorem 2 The FL1 triple-circuit demand-parts defined by

$$[C_i^{\text{FL1}}, Q_{ci}^{\text{FL1}}(t), R_{di}^{\text{FL1}}(t), P_{ei}^{\text{FL1}}(t)]_{i=1,2,3;t>0} \quad (18)$$

translate into a FL0 single-circuit demand-part

$$[C_c^{\text{FL0}}, Q_c^{\text{FL0}}(t), R_d^{\text{FL0}}(t), P_e^{\text{FL0}}(t)]_{t>0} \quad (19)$$

by summations of capacities, charges, and power demands,

$$C_c^{\text{FL0}} = C_c^{\text{FL1}}, \quad (20)$$

$$Q_c^{\text{FL0}}(t) = Q_c^{\text{FL1}}(t), t > 0, \quad (21)$$

$$P_e^{\text{FL0}}(t) = P_e^{\text{FL1}}(t), t > 0; \quad (22)$$

and a derived resistance

$$R_d^{\text{FL0}}(t-) = \frac{\frac{Q_c^{\text{FL0}}(t)}{C_c^{\text{FL0}}} - \frac{P_e^{\text{FL0}}(t-)}{Q_c^{\text{FL0}}(t)}}{\dot{Q}_c^{\text{FL0}}(t)} \quad (23)$$

for the demand-control resistor.

Proof: With $C = C_c^{\text{FL1}}$, $Q(t) = Q_c^{\text{FL1}}(t)$, and $P(t) = P_e^{\text{FL1}}(t)$, the assertion follows from Lemma 1.

Remark 3 Note that (23) is the quadratic first-order differential equation (5).

Discussion

Methodology

An axiomatic *wirkgefuge* is described as a mathematical framework for translation of dynamics from canonical tripartite "function-level no.1" to whole-body "function-level

0” aggregate. It splits the aggregate’s functional activity according to the number of the aggregate’s constituent logical units and distributes its charge according to their respective demands; but it also re-combines individual units’ dynamics into the dynamics of their aggregate whole. This points to its use at other function levels: One may consider the liver organ as an aggregate whole at “function-level no. n ” for some positive number n , say, and involve its *wirk-components* as logical units on “function-level no. $(n + 1)$ ”, taking care that the decomposition is exhaustive and non-overlapping. In this way, one can start to work downwards from any logical unit in a functional hierarchy; to work upwards, however, one has to take into account *all* logical-unit “neighbors” on the same function level before one can up-scale to upper level dynamics. Hence, drill-down appears to be the preferable direction.

The mathematics of *axiomatic wirkgefüge* is deliberately simple, and may seem too simplistic to be relevant, at first sight. However, it rapidly builds up complexity when decomposing functional aggregates into logical units way down - long before one gets to the bottom of 10^{14} living cells, each a burn chamber and base functional unit. It then reminds one of the wheat-chessboard problem.

This exposition merely describes the “firing” in the sense of energy transfer dynamics; specification of a control regimen of dynamics in single and in triple circuits is postponed. The differential equations were hence left without solutions, as the side conditions that are necessary to obtain specific solutions depend on an adequate “wiring” in the sense of a *kybernetik schaltgefüge* that permits the human body system to energize required action of its *axiomatic wirkgefüge* in any situation for preservation of its integrity and survival. Their common independence of physical realization is expected to permit to design both configurations by analogy with better understood complex engineered production systems.

Medical Perspective

Partition of whole-body’s power demand into its canonical *wirk-components* - vital, productional, operational - marks an entry point for investigation of partitional variation in different stressing (by exposures or interventions) scenarios and of any discrepancy in power-demand partitioning from so-called “normal” population in various disorders; disablement, impairment, somatic or psychic chronic disease can be expected to imply partition shifts in either productivity (musculo-skeletal locomotor function, sexual reproductivity), or operational ability (communication with body’s outside world, self-steering one’s operations), or vital-functions activity (e.g. respiration, circulation, immune response, nervous control, hormonal regulation, food intake, digestion, waste ejection), and possibly in more than one. Detectable as deviations from “normal” whenever it manifests itself in person’s behavior, evidence of persistent shifted partitioning may also be of interest in a context of unspecific screening for power-demand anomalies in human body system.

Specifically, among the first would be investigations in patients with manifest movement disorders and Parkinson’s disease, as well as in patients in different stages of progressive recovery, functional rehabilitation, work and social-life re-integration, and life-balance restoration after an ischemic stroke with moderate to severe neurological deficits [5]; for healthy-subject controls, athletes will be first choice in these investigations.

The practical implementation poses challenging problems regarding technology for taking specific measurements of *wirk-components* power demands and methodology of its application. Relative assessments will be in foreground. Whole-body power demands when “sleeping”, “awake lying still” of 77 cal/h, “sitting at rest”, “standing relaxed”, “walking slowly”, and “running” of 65 cal/h, 77 cal/h, 100 cal/h, 105 cal/h, 200 cal/h, and 570 cal/h, respectively, [6], give first clues, e.g. to net walking-power demand against background upright posture, of 95 cal/h. (Note that an interface for exchange with outside world in total energy balances is not included.)

Conclusions

The axiomatic construct suggests a path into multi-scale modeling of human body system *wirkgefüge*, coherent by design, and progress will be made from top to bottom. This way, impact from health-compromising exogenous factors can be integrated at any level, but applicability in clinical context is still to be confirmed.

References

- [1] J. Mau. Systems Neuroergonomics. In R. Wang and X. Pan, editors, *Advances in Cognitive Neurodynamics (V)*, chapter 59, pages 431–437. Springer Science+Business Media, Singapore, jan 2016.
- [2] J. Mau. Reducing complexity in modeling human body. In *Proceedings of The XVIII International Conference on Complex Systems: Control and Modeling Problems (CSCMP-2016)*, pages 23–28. Samara, Russia, sep 2016.
- [3] N. Wiener. *Cybernetics or Control and Information in the Animal and the Machine*. Massachusetts Institute of Technology, Boston, 1961.
- [4] H. Sachsse. *Einführung in die Kybernetik*. Vieweg, Braunschweig, 1974.
- [5] J. Mau. Kybernetic modeling of human body system. In *Proceedings of the 12th Russian German Conference on Biomedical Engineering (XII RGC’2016)*, Suzdal, Russia, pages 11–15. Vladimir, Russia, jul 2016.
- [6] J. E. Hall. *Guyton and Hall Textbook of Medical Physiology*. Saunders, Philadelphia, 12 edition, 2011.

Acknowledgments

Gratefully received comments by Alexander Churilov (St Petersburg), Hans-Werner Müller (Düsseldorf), and Wen-Xiao Zhao (Beijing) helped to improve the presentation of content. All errors are mine, however.

Enabling “Surgery 4.0”: 5G Data Transmission in Minimally-invasive Surgery

T. Vogel^{1,2}, N. Marahrens¹, S. Koller¹, A. Jell^{1,2}, D. Ostler¹, W. Weigel³, J. Eichinger³, H. Feußner^{1,2}, M. Kranzfelder^{1,2}

¹ Research Group Minimally Invasive Interdisciplinary Therapeutical Interventions (MITI), Klinikum rechts der Isar, TU Munich, Germany;

² Department of Surgery, Klinikum rechts der Isar, TU Munich, Germany;

³ Huawei Munich Research Centre, Germany

Contact: michael.kranzfelder@tum.de

Introduction

With the expansion of the digital functionalities in the OR in the sense of "Surgery 4.0" facilitating important applications such as real-time person or asset track- and tracing or tele-robotic surgery, the question of improved data transmission quality becomes more and more urgent (1). As the currently available technologies for data transmission in the OR (Ethernet/LAN, W-LAN, Bluetooth) are limited in terms of transmission rate, latency and signal stability (2), the upcoming mobile data transmission technology 5G seem to offer a high potential.

5G includes the following characteristics as compared to the current mobile transmission standard 4G/LTE: a 100 times higher data transmission rate (up to 10 Gbps), an extremely low latency (1ms) and 1000 times higher capacity (3). The possibility of transmitting a high data volume almost without delay with high precision and stability makes the 5G technology interesting for different medical applications.

It is not yet known whether the promising 5G mobile telecommunication performance is sufficient for the demanding medical applications such as person or asset track- and tracing, video data transmission for telemedicine and tele-robotic surgical operations, where fast, secure and ubiquitously available data transmission is essential.

The latter is the basic prerequisite for the emerging field of cognitive surgery (4), in which the surgical team is extensively supported in its work by the digitalized OR environment. It was the purpose of this research project to evaluate possible fields of applications for 5G to enable Surgery 4.0.

The manuscript comprehends of two different sections:

- a) A Delphi study evaluating the expectations and acceptance of 5G in the medical (surgical) field in general
- b) The evaluation of 5G technology for a surgical telepresence application (use-case tele-robotic surgery)

Materials and Methods

Delphi study

In order to first obtain an estimation of possible 5G applications in the medical field, necessary technical developments and comparison to currently available data transmission technologies (4G/LTE, WLAN), a Delphi study was carried out. The Delphi method is a structured communication method, which relies on a panel of experts. It is based on the principle that forecasts from a structured group of individuals are more accurate than those from unstructured groups (5).

In two rounds, a fixed panel of 12 experts (industry n= 9, small and medium size enterprises n= 2, academic institution n= 1) provided a written assessment of a list of 28 theses/questions related to the potential future developments of 5G, which was compiled as questionnaire by the authors. The theses/questions were grouped in five different sections: experience, trend, impact, promoting and detaining factors with/of 5G technology. For every thesis/question, probability was explored and in a second round, the results of the previous round were given as feedback. Subsequently, experts were asked to reassess the hypotheses and either confirm or revise their own opinion, where it diverges from the majority opinion.

Surgical Telepresence

Telepresence in general refers to a set of technologies allowing a person to feel as if they were present, to give the appearance of being present, or to have an effect (via tele-robotics) at a place other than their true location (6).

The term teleconsultation in the medical field means an image- or video-based consultation of a remote expert giving verbal advice during an operation or procedure. Whereas surgical telepresence reveals a (real) physical action at the

distant point of care by a consultant. In this case, a mechatronic support system (e.g. a surgical robot = slave) processes the haptic commands of a consultant entered into an interface (master) into precise manipulations at the remote surgical site (7). As compared to teleconsultation, the requirements of data transmission volume, rate and latency are significantly higher for telepresence, since any delay or interruption of the dataflow would be extremely hazardous.

To evaluate 5G performance for surgical telepresence, we set up an ex-vivo use-case using the robotic camera control arm SoloAssist® (AKTORmed, Barbing, Germany) as slave system maneuvering a laparoscope inside the abdominal cavity of the OR phantom ELITE (CLA Coburg, Germany). Data transmission characteristics were measured. Control commands for the slave system (move up-down-left-right, zoom-in and out) were manually entered into a graphical user interface (GUI, Fig. 1) and data transmission to the robotic camera control arm was conducted with 5G. Normally, data transmission from the input interface to the robot is tethered.

Communication with the SoloAssist® is bidirectional and was realized through a CAN-interface. It allows to send movement commands to and receive position information from the robotic camera control arm. The unidirectional (video) data exchange with the laparoscope unit (K. Storz, Tuttlingen, Germany) was realized through a frame grabber. It receives the analog signal from the laparoscope through a coaxial connection and converts it to digital format. Key capabilities of the 5G testbed (5G NR V2V oriented) are given in Table 1.

Latency	< 2ms
Data rate	Uplink 6 Mbps (HD), Downlink < 10kbps
Wireless range between terminal / sensor and 5G access point	Indoor < 20 m
Interface	1 Gigabit Ethernet (cat6)
Transfer mode	Ultra-reliable low latency communication (URLLC)
Terminal speed	0 kmph
Duplex Mode (LTE)	Time Division Duplex (TDD)
Frequency	2.6 GHz / 20MHz

Table 1. Characteristics of the Huawei 5G testbed (USRP X310). Versatile data interface configurable to support different 5G applications using low-latency (<1ms) machine-type communication.

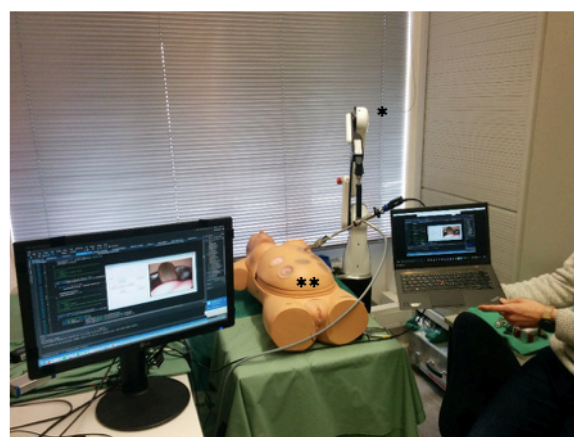
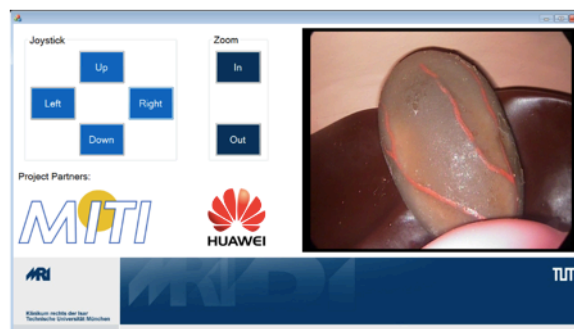


Figure 1. Upper figure: Graphical user interface (GUI) on a tablet computer. Touchscreen to enter the direction of movement for the robotic camera arm SoloAssist® (move up-down-left-right, zoom-in and out), display of the video image (gallbladder). Lower figure: The robotic camera arm (*), maneuvering the laparoscope inside the abdominal cavity of the operating phantom ELITE (**, CLA Coburg), is controlled via GUI by means of 5G data transmission.

Results

Delphi study

At time of abstract submission n= 10 experts (83 %) had completed two survey rounds. Principal points are: 5G technology is regarded as trend-setting for the future transfer of information in the healthcare domain (85.7% agree / 14.3% agree fully). The current mobile standard 4G/LTE is assessed not to be sufficiently suitable for the expected future data transmission requirements (57.1% agree fully). According to expert opinion, the financing of 5G-based services should be actively supported by healthcare politics (42.9% agree fully / 57.1% agree more likely) and potential industry partners should be involved as early as possible in the process of 5G integration in healthcare applications (71.3% agree fully / 28.7% agree more likely).

Preliminary study results confirm our use-case hypotheses that telepresence with 5G data transmission improves medical care in remote regions by actively including spe-

cialist knowledge and skill into patient diagnostic or treatment (85.7% agree with operation of 5G technology).

Uncertain yet is the question, whether the experience gained so far with mobile data technology (4G/LTE) allows a good assessment of which problems, requirements and opportunities arise with the implementation of the new 5G data technology or not (57.1% neutral / 28.6% hardly agree / 14.3% tend to agree).

Telepresence

The active involvement of an expert over a distance in the course of an operation was realized in the telepresence use-case. By implementation of the 5G data transmission module, the robotic camera-control arm SoloAssist® was successfully maneuvered wireless without any data transmission interruptions or data transmission delay. A prototype installation of the system was presented at the Mobile Broad Band Forum (MBBF) in London in December 2017.

5G technology allows different settings of the transmission parameters of the physical layer. Especially for the URLLC mode that is used in our setup, a careful parameter selection (e.g. subcarrier spacing and time transmission internal (TTI) length) is important to achieve a minimum of latency combined with a high robustness against transmission errors (Fig. 2).



Figure 2. Latency of 5G data transmission can be reduced to < 1ms by carefully selecting the transmission parameters. The measured signal delay of the deployed 5G module including encoding and decoding was 0.41ms.

The evaluation of the transmission properties in terms of reliability is shown in Figure 3. Classic OFDM (Orthogonal Frequency-Division Multiplexing, used in 4G) was compared with a filtered variant (p/f- OFDM, used in 5G). Two different radio channels were used. Measurements showed that a minimum signal-to-noise ratio of 15dB is required to achieve a 99.999% reliability.

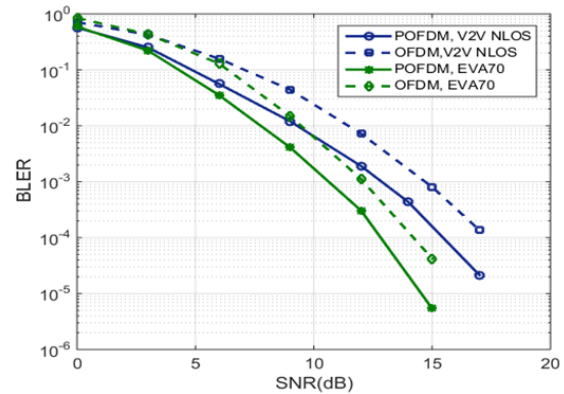


Figure 3. Reliability of radio transmission. OFDM (Orthogonal Frequency Division Multiplexing, used in 4G). p/f- OFDM are filtered variants used in 5G. Radio channels: V2V (Vehicle to vehicle), NLOS (Non line of sight pass) and EVA70 (Extended vehicular A). BLER = block error rate, SNR = signal to noise ratio.

Conclusion

Advanced mobile telecommunication technologies have the potential to enable future applications of “Surgery 4.0”. Preliminary results of the Delphi study reveal a positive perspective of 5G implementation in a clinical environment. 5G data transmission creates a future-oriented possibility of telepresence, which is not yet available in this form. For upcoming research, special focus should be put on medical real-time interaction applications, especially remote robotic surgery, as the future 5G standard will not only provide high data rates for the transmission of multimedia content up to virtual reality, but also an extremely reduced latency and simultaneously high reliability of data transmission.

Acknowledgements

The author(s) declared no potential conflicts of interest with respect to the research, authorship, and/or publication of this article. This research project is funded by the Bavarian Government (MED-1705-0003).

References

1. Feußner H, Park A. Surgery 4.0: the natural culmination of the industrial revolution? Innovative Surgical Sciences.
2. Li QC, Niu H, Papathanassiou AT, Wu G. 5G network capacity: Key elements and technologies. IEEE Vehicular Technology Magazine. 2014;9(1):71-8.



3. What is 5G? Characteristics and usages 2018.
Available from:
<https://www.gemalto.com/mobile/inspired/5G>.
4. Kranzfelder M, Schneider A, Fiolka A, Koller S, Reiser S, Vogel T, et al. Reliability of sensor-based real-time workflow recognition in laparoscopic cholecystectomy. *International journal of computer assisted radiology and surgery*. 2014;9(6):941-8.
5. Okoli C, Pawlowski SD. The Delphi method as a research tool: an example, design considerations and applications. *Information & management*. 2004;42(1):15-29.
6. Draper JV, Kaber DB, Usher JM. Telepresence. *Human factors*. 1998;40(3):354-75.
7. Kranzfelder M, Schneider A, Fiolka A, Koller S, Wilhelm D, Reiser S, et al. What Do We Really Need? Visions of an Ideal Human–Machine Interface for NOTES Mechatronic Support Systems From the View of Surgeons, Gastroenterologists, and Medical Engineers. *Surgical innovation*. 2015;22(4):432-40.

IVAP 2025 – Towards the collaborative operating room

D. Ostler¹, N. Marahrens¹, N. Kohn¹, S. Koller¹, M. Kranzfelder^{1,2}, H. Feussner^{1,2}, D. Wilhelm^{1,2}

¹ Research Group MITI, Klinikum rechts der Isar, Technical University Munich,
Trogerstr. 26, 81675 Munich, Germany

² Department of Surgery, Klinikum rechts der Isar, Technical University Munich,
Ismaninger Str. 22, 81675 Munich, Germany

Contact: daniel.ostler@tum.de

Introduction

The advances in digitalization and information processing are influencing interventional medicine. Medical devices include a growing number of functionalities, which provide more operational flexibility while increasing complexity of the OR environment [1]. Adapting to this development provides an essential challenge and opportunity to optimize modern surgery and therapy procedures. With the advancements of digital assistance systems, it can be ensured that the surgeon concentrates on the essential, namely the patient and the operation, rather than being distracted by the technical overflow of peripheral devices. In this work we present our vision and first results of a collaborative operating room that actively supports context-sensitive intra- and postoperative surgical therapy. To achieve this goal we enhanced a new Operating Room (OR) for comprehensive data acquisition, recognition of the OR team and computational tools for workflow analysis in order to achieve an understanding of the situational sequence and semi-automatic assistance and ensure an increased security level.

The functioning of the cognitive surgical environment is demonstrated by a typical example: the laparoscopic resection of the gallbladder for symptomatic gallstones. Such an operation is very common and is performed about 200,000 times a year in Germany. The procedure is highly standardized.

Materials and Methods

The basic idea of this concept relies on three pillars: First, precise analysis and comprehensive acquisition of all available information about the surgical situation, second, by the interpretation using comprehensive structured knowledge and third, the derivation of the relevant assistance functions and smart services. The system components involved, continually feedback to the IVAP OR-system and thereby verify the workflow, as illustrated in Figure 1. These main components are described in more detail in the following section.

Data acquisition

An important prerequisite for situational awareness of the cognitive-technical system is the actual ability of "understanding" similar to a surgeon. A robust interpretation of

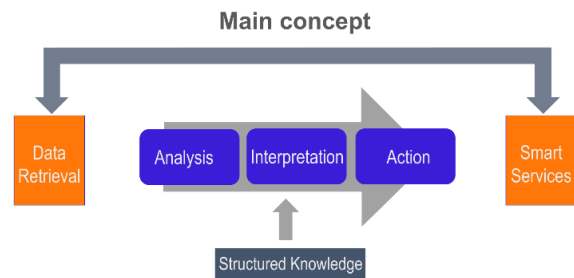


Figure 1: Main concept of the collaborative operating room is based upon three pillars: analysis of captured data, interpretation of comprehensive real-time information based on structured knowledge and the prediction of further activities and their execution (action) in the form of smart services.

the current surgical context requires a centralized continuous provision with real time data as shown in [2]. We implemented a central data acquisition framework as illustrated schematically in Figure 2.

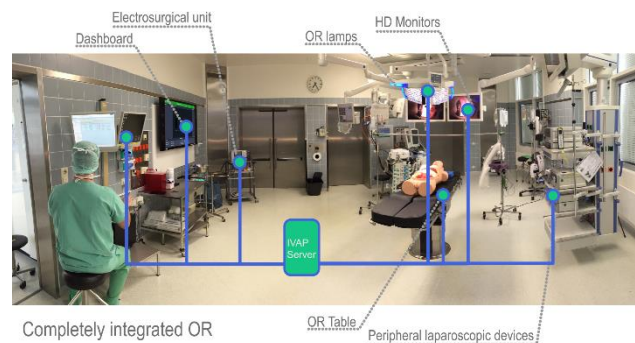


Figure 2: Schematic illustration of a centralized data acquisition within the OR

This broad variety of data is heterogeneous by nature and can be grouped as follows:

1. *Device data:* Status of installed and peripheral surgical components. In particular, we collect information about the operating table, room-, surgical- and endoscopic light, insufflation pressure and flow, aspiration and suction volume, usage of the electrosurgical devices, and surgical instruments in use.

2. *Data on the surgical team members:* The OR is equipped with four Bluetooth-Low-Energy (BLE) antennas, which allow capturing the presence of staff members and a coarse localization within in the OR. Subject to their permission, the level of experience of staff members is stored in a database.
3. *Pre- and intraoperative patient data:* previous diseases, laboratory values, anaesthesiological data. The clinical information system (CIS) provides a wide range of patient-relevant data. Statistical methods and machine learning are currently being evaluated in order to estimate the preoperative course of the operation.
4. *Image and video data:* pre- and intraoperative radiological imaging, endoscopic video data, overview cameras. Especially the video data contains a lot of information, which has to be extracted by suitable algorithms.

This categorization naturally involves overlaps, e.g. regarding information, which can be derived from the different video streams. For example, the overview camera can be used to track staff movement or to detect the use of special equipment (e.g. C-arm). The laparoscopic image is all the visual information the surgeon has from the surgical site inside the patient. Therefore, a lot of information about the surgical procedure and usage of instruments can be deduced by means of computer vision methods. We have applied Deep Learning methods on the laparoscopic video stream to perform an end-to-end surgical phase recognition from the laparoscopic video frames, as shown in [3]. Additionally a convolutional neural network (CNN) was trained to detect instruments in the laparoscopic image and autonomously controls a camera guidance robot [4].

All data – device, sensor and inferred from video frames – is collected centrally in real time and stored for further processing. Alongside the structured knowledge, this data forms the input for the determination of the surgical workflow.

Structured knowledge

In order to recognize the actual surgical process, which can deviate from the planned course, the system requires a detailed OR-model. The OR-model consists a systematic, finely granulated description of the course of action, including all conceivable variants and the description of alternative points. Regarding the case of laparoscopic Cholecystectomy, the model consists of eight phases, each of which is precisely modeled. The highly standardized procedure consists of 32 different surgical steps, about 1,600 actions and about 16,000 surgical manipulations. The modelling was done using the Business Process Model and Notation (BPMN) 2.0.

Based on these models, a rule-engine was designed, which performs the actual interpretation of the data in the central database and derives relevant actions and support functions.

Derived action: (semi-)autonomous support

The autonomous execution of actions by the IVAP OR-system in a closed loop would be desirable and technically feasible. However, this is currently prevented by regulatory barriers. Therefore, only entirely uncritical actions are performed automatically such as switching off the room lights or closing the window blinds. More critical support functions are implemented in a semi-autonomous i.e. human-in-the-loop manner. Decisions and actions are prepared by the system, but must always be acknowledged or carried out by a person. Hence, specific human machine interfaces were designed as part of the cognitive OR concept.

Human machine interaction

The communication between the system and the surgical staff is implemented in different ways. Since speech is one of the most natural forms of communication, a voice output (based on Microsoft Speech API) was integrated. Because this can easily lead to disturbance of the team, speech synthesis of messages and warnings is only used before the operation (greetings of the surgeons) or when a staff member's immediate attention is required. The display of messages on the central dashboard or small tablet screens close to the scrub nurse is much less disturbing. Those messages can be status updates, non-urgent messages or recommendations for actions. Additionally, the touchscreens can be used as backchannels for user input into the cognitive IVAP OR-system as shown in Figure 3.

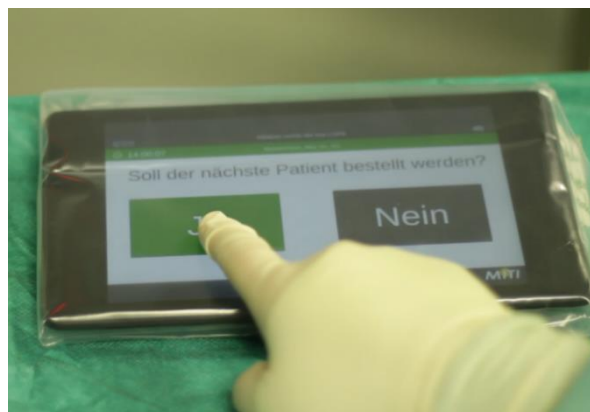


Figure 3: User-input on sterilely packed tablet. The IVAP OR-system asks, whether the next patient should be ordered and waits for approval by the user.

Results

Comprehensive networking of all OR components and the installation of a few additional sensors enabled an ordinary OR to be converted into a framework for surgical data acquisition and laid the foundations for an intelligent support of the OR team.

Since cognitive support needs situational awareness, a substantial amount of effort was invested into the recognition of surgical phases and actions. While the sensor driven recognition was shown by [5] we implemented a CNN for the detection of the surgical phase within the laparoscopic

video. The CNN performed with an average precision of 65.9% and an average Recall of 74.7% [3].

Based on the surgical phase recognition and the sensor- and device data driven rule-engine, we implemented a number of assistive functions. These functions can be categorized as follows:

1. *Room control*: control of window blinds and room lights
2. *Personalized setup*: recognition and greeting of the surgeon. Display of preferred settings (e.g. height of surgical table)
3. *Monitoring of device settings*: device parameters are cautiously monitored. In case of deviation from the specifications, warnings are given as visual display or voice output (e.g. insufficient brightness of the endoscopic light source, excessive patient pressure of the insufflator).
4. *Optimization of associated processes*: situational reminders for Team-Time-Out, ordering of the next patient and notification of cleaning staff at the end of surgery.

Conclusions

The passive conglomerate of different high-tech modules was transformed into an integrated collaborative assistance system. The successful implementation of this project represents the first major step in the direction of Surgery 4.0 [6]. While in the case of laparoscopic cholecystectomy, a manual “top-down” modelling was possible, methods for automatic abstraction of surgical models using statistical and machine learning approaches is the subject of our current research.

References

- [1] Kenngott H, Wagner M, Preukschas A et al. Der intelligente Operationssaal. *Der Chirurg* 87:1033-1038, 2016.
- [2] Ostler D, Kranzfelder M, Stauder R et al. A centralized data acquisition framework for operating theatres. In: *E-health Networking, Application & Services (HealthCom)*, 17th International Conference on. IEEE, p 1-5, 2015.
- [3] Stauder R, Ostler D, Kranzfelder M et al. The TUM LapChole dataset for the M2CAI 2016 workflow challenge. *arXiv preprint arXiv:1610.09278*, 2016
- [4] Marahrens N, Koller S, Ostler D et al. Deep learning-based robotic endoscope guidance. In: *Jahrestagung CURAC*, 2017.
- [5] Kranzfelder M, Schneider A, Fiolka A et al. Reliability of sensor-based real-time workflow recognition in laparoscopic cholecystectomy. *International journal of computer assisted radiology and surgery* 9:941-948, 2014.
- [6] Feussner H, Ostler D, Kranzfelder M et al., *Surgery 4.0*. In *Health 4.0: How Virtualization and Big Data are Revolutionizing Healthcare* (pp. 91-107). Springer, Cham, 2017.

Acknowledgements

This research project “Interventionsarbeitsplatz (IVAP) 2025” was funded by the Bavarian Research Foundation.

Creation of 3D nanocomposite bioconstructions using a layer-by-layer laser prototyping device

U.E. Kurilova¹, N.N.Zhurbina¹, D.A. Ignatov¹, D.I. Ryabkin¹, A.A. Polokhin¹, E.S.Pyankov¹, A.Yu. Gerasimenko^{1,2}

¹National Research University of Electronic Technology, Shokin Square 1, Moscow, Russia

²I.M. Sechenov First Moscow State Medical University, Bolshaya Pirogovskaya st. 2-4 Moscow, Russia

Contact: kurilova_10@mail.ru

Introduction

Nowadays a high demand for bioconstructions used for regeneration of tissue defects, including difficultly repaired osteochondral ones, is exist. One of the important factors for successful developing of them is production of three-dimensional biocompatible scaffolds that provide replacement of a damaged tissue site and maintain proliferation of the patient's cells. As a result of implantation, a healthy tissue is formed in the site of a defect, and a scaffold dissolves gradually as tissue grows.

Among current methods of scaffolds obtaining, an important place is given to methods of three-dimensional prototyping. Their advantages are unquestionable in case of preparation of scaffolds for regeneration of osteochondral defects: high resolution, the ability to get a scaffold with shape that exactly coincides with CT and MRI imaging of defect, and the possibility of controlling the internal structure of scaffold [1] However, not all materials suitable for using in 3D prototyping have required characteristics [2]. Often they are either not completely biocompatible, but also are not biodegradable, thus performing a kind of substitution and remaining a foreign material in the body.

In order to overcome the shortcomings of traditional methods, the laser device for the fabrication of nanocomposite bioconstructions by method of laser 3D prototyping was developed. In the work we created samples of 3D nanocomposite bioconstructions and carried out studies of their structural and biological properties.

Materials and Methods

Materials

Bovine serum albumin (BSA) and bovine collagen (BC) were selected as components of the protein matrix. BSA is one of the main proteins of blood performing a transport function. This protein also has the ability to be cross-linked under the action of laser radiation [3]. A lyophilized BSA purity of more than 99% was used. BC is one of the main proteins of the extracellular matrix. BC was taken in the form of suspension in water (2% wt. of pure collagen). The solvent for all components was water for cellular studies.

Single-walled carbon nanotubes (SWCNTs) of the types of 90A (length 0.5-1.5 nm, diameter ~ 1,5 nm) and 95TA (length - more than 5 microns, diameter -1-2 nm) were used for the production of nanobioconstructions. Nanotubes were in form of black paste in deionized water with a nanotube concentration of ~ 2.5% wt.

Preparation of dispersion

The first step of the dispersion preparation was the dissolution of carbon nanotubes in water. The required amount of SWCNTs in water was mixed with a magnetic stirrer for 40 minutes. Then they were sonicated in a homogenizer with amplitude of no more than 30 W for 45-60 minutes to reduce the number of aggregated CNTs. Then BSA (25%) and collagen (1%) were added to the CNTs with water, it was mixed with the stirrer and then in an ultrasonic bath until the components were completely dissolved.

Device for making solid samples

The principle of the device operation is moving the focused laser beam along a planned trajectory above a container with the water-protein dispersion of carbon nanotubes. Under the action of laser radiation, evaporation of the water part occurs while laser radiation orients the nanotubes. Thereby they form a strong, porous scaffold that promotes the regeneration of bone and cartilage tissue cells [4-6].

Configuration of the device is shown in fig. 1. The main component of the device is the source of radiation (2) - semiconductor laser with a wavelength of 810 nm, which is controlled by the power supply (1). Radiation is transferred by means of optical fiber to a lens that is fixed to moving system, based on stepper motors (4).

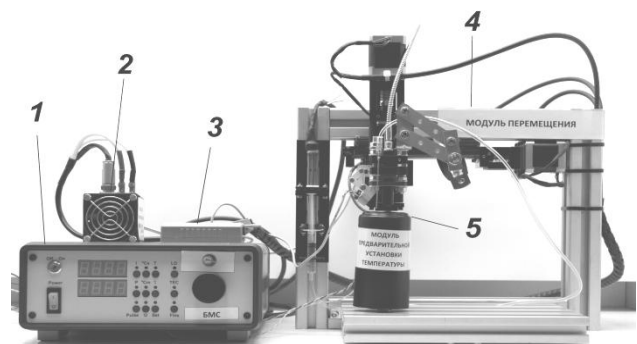


Figure 1: The device for making of samples using layer-by-layer laser prototyping method: 1 - power supply unit, 2 - semiconductor laser, 3 - thermostabilization system, 4 - moving system, 5 - container with the dispersion

The device is equipped with an IR-sensor that measures the temperature of the dispersion. The sensor is connected to the thermostabilization system (3). The main purpose of this system is to dynamically adjust the laser radiation power to maintain the established dispersion temperature.

The creation of bioconstructions takes place at a certain temperature of 40-55 °C at the bottom of the container (5) fixed on the preliminary heating table.

Focusing of laser radiation was carried out in a spot with a diameter of ~ 0.1 μm. The travel distance of the focused beam was also ~ 0.1 μm. The thin layer of water-protein dispersion of nanotubes was distributed at the bottom of the container using a syringe connected to the dosing system. Then the dispersion was irradiated by laser along a given trajectory. After the dispersion layer was cured, the amount of dispersion necessary to form the next layer was added to the container.

Analysis of samples surfaces

The surface structure of the experimental samples was studied using confocal microscopy. When scanning with this method, a focused laser beam was moved along the sample area. A laser confocal microscope Lasertech VL 2000 DX with a high numerical aperture (up to 0.95) and a short wavelength of laser radiation was used.

An atomic force microscope (AFM) was used for more detailed analysis of the morphology of the sample surface. In the PeakForce QNM mode, the power curve was taken at each point of the sample and immediately was analyzed. The study was conducted in a semi-contact mode in air. A probe with a tip diameter of 5 nm was used. The scanning was performed on an area of 10 μm² and 30 μm².

Study of the internal structure of samples

The internal volume structure of the samples was studied with the x-ray microtomograph. The maximum possible spatial resolution was selected. Using the intensity function, the voltage and current at the cathode (no more than 30 kV) were adjusted to obtain an average intensity value of 30-50%. The scan parameters were selected in accordance with the density and geometric dimensions of the sample.

Investigation of biocompatibility

To study the biocompatibility, experiments related to the proliferation of cells (osteoblasts and chondroblasts) were carried out on samples in culture plates in a CO₂ thermostat at 37 °C for 48 hours. After that, the number of cells was evaluated and their morphology was analyzed. The restoration of osteochondral defects was carried out on laboratory animals (rabbits).

Results and Discussion

Characterization of surface of samples

Samples obtained using the described method are shown in fig. 2. The power at which the dispersions solidify depended on the concentration of nanotubes and the trajectory which the laser beam moved along. Dispersions with a low concentration of nanotubes cured more slowly because of the high transparency of the layer. To form the next layers, a lower beam power was required compared to one for the first layers. Due to the varying of power and the number of passes of the trajectory to form one layer, it

is possible to achieve a structure of different hardness - from soft rubberlike to completely solid. It is successfully possible to obtain samples with grid structure that promotes cell growth on the surface by mimicking the structure of the natural extracellular matrix.



Figure 2: 3D nanocomposite bioconstructions obtained from a grid trajectory with a distance of 0.5 mm (a) and 1.5 mm (b) between parallel lines

To obtain the experimental samples, the distance to the container with dispersion was preliminarily chosen with the smallest diameter of the beam. The selected speed of the radiation source was 2.5 mm/s. The parameters of making of samples are given in tab. 1.

Table 1: Parameters of making

Sample	Type and concentration of SWCNTs	Current intensity	Number of trajectory passes
I	90A, 0,01 %	3.0-4.8	1-4
II	90A, 0,1 %	2.3-3.3	2-4
III	95TA, 0,01 %	3.3-4.8	1-4
IV	95TA, 0,1 %	2,5-3,0	1-2

Images of a top view of sample II obtained by laser confocal microscopy are shown on fig. 3. Dark and light bands correspond to the low and high areas of the sample. The average value of the band width for this sample was ~ 20 μm and it depended on the focusing of the laser beam on the sample. Each of the bands contained basically perpendicular convexes in the form of "folds", whose size was ~ 1 μm and depended on the laser radiation power.

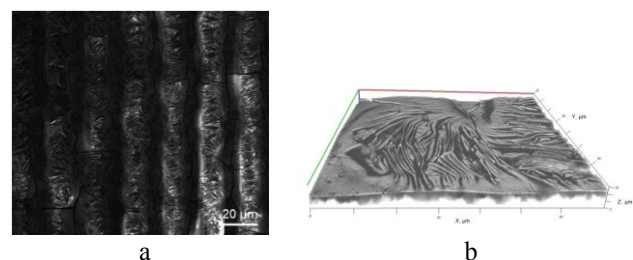


Figure 3: Surface topography of samples obtained by confocal microscopy (a - microimage, b - reconstructed image)

Figure 3 b shows the reconstructed three-dimensional image. It is clearly seen from the figure that the "folds" impart a relief surface to the sample, which subsequently establishes an interconnection between the structure of the

samples and their biological properties - an increased adhesion of the cells to the samples, because the size of the chondroblasts and osteoblasts is about 50 μm .

Analysis of surface using AFM

Fig. 4a shows the AFM topogram of sample I. It is a typical picture of the surface layer of protein material. The main characteristic of this image is the presence of pores on the surface. A network of shallow channels is visible, which apparently are fractures on the surface of the material, formed as a result of thermal effects on the protein component. The width of the channels is 30-70 nm.

Several types of pores with a diameter of 100-200 and 400-700 nm are observed on the AFM images of sample II (fig.4b). In this sample, the pores were uniformly distributed and had a small dispersion in size, in comparison with sample I. In sample II, formation of shallow cracks with a width of 200-500 nm and the absence of a network of channels were observed, as in sample I.

Sample III (fig.4c) also had a porous structure, with different pore sizes. The sample had a homogeneous structure and no large fractures on the surface of the material.

Sample IV (fig. 4d) had a large number of pores uniformly distributed over the entire surface of the sample with a diameter of 70-100 nm and 10-30 nm. In this sample there were no fractures, and there was also no network of channels.

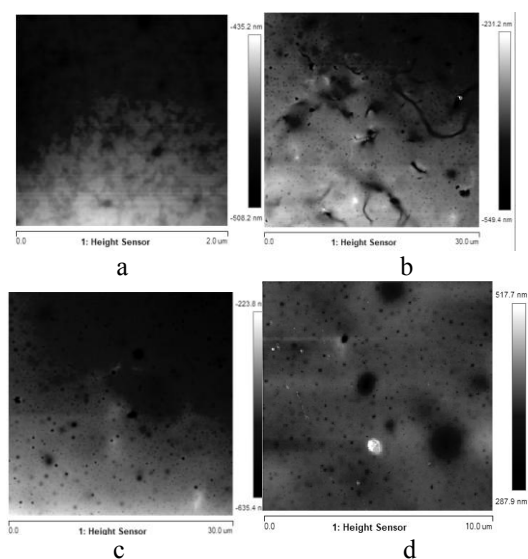


Figure 4: AFM images of the samples surface

The following was established as a result of studies of the structure of experimental samples by the AFM method. The surface of all samples is homogeneous porous material, the structure of which is typical for products based on proteins. Nanotubes on the surface could not be detected, which is due to the fact that all SWCNTs was under the layer of the protein matrix inside the material. The experimental samples had pores of various sizes. In samples I, III, IV there were large pores with a diameter of 500-5000 nm. These pores were distributed irregularly and were the result of air bubbles occurred during the formation of

samples. Because sample I had pores of smaller diameter than sample II and the pore diameter in sample III exceeded the pore diameter in sample IV, the porosity is directly dependent on the SWCNTs concentration for samples I and II based on SWCNTs 90A, and is on the inverse relationship for samples III and IV on the basis of SWCNTs 95TA. The concentration of CNTs affected the appearance of a network of shallow channels on the surface of samples I and III. When the concentration of CNTs increased from 0.01 to 0.1%, the channel network was not observed (samples III, IV). This may be due to the reinforcing effect of carbon nanotubes in the protein matrix, which prevents the formation of fractures on the surface of the material.

X-ray microtomography

The obtained images of the internal structure of large samples by the X-ray microtomography method are shown in fig. 5. Based on the results of studies of the structure of sample I, it was found that cavities occupying 50-70% of the sample area were observed in the upper and lower layers of the sample, but the central part of the sample had a homogeneous structure. In the structure of the sample there was a pore space with a radius of 0.2 mm and a crack of a size of 0.25 mm. The presence of individual large pores in the sample is due to the presence of air bubbles in the initial nanocomposite dispersion, which creates cavities in the structure of the material during laser prototyping. This problem can be solved by using additional ultrasonic treatment of the nanocomposite dispersion.

Two-dimensional visualization of sample II is shown in fig. 5b. Cavities with a diameter of 0.1-1.0 mm were observed in the structure of the sample. The number of micropores in this sample exceeds the amount of pores found in sample I, while the pores are uniformly distributed throughout the sample volume and have similar dimensions.

In sample III (fig. 5c), according to the results of microthomography, cavities with a diameter of 0.4 to 2.7 mm were found predominantly distributed around the central part of the sample. Such an inhomogeneous structure can be a consequence of some irregularity distribution of SWCNT in the volume of the initial dispersion and a large number of air bubbles and protein clots.

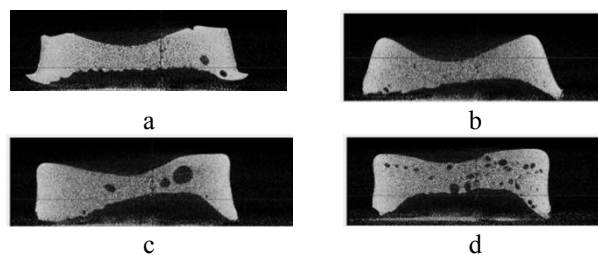


Figure 5: The internal structure of large samples, obtained with X-ray microtomography

In the case of sample IV, a series of cavities measuring from 0.2 mm to 0.9 mm were observed throughout the investigated section. The structure of the material looks more homogeneous. In general, the cavities are distributed evenly, with the exception of some sample areas. A much larger number of pores were observed than in sample III with a lower concentration of nanotubes.

The formation of a porous internal structure is most likely determined by laser heating of the nanocomposite dispersion. Carbon scaffold has high thermal conductivity, contribute to a strong heating of the areas nearby and resulting in the boiling of the water-protein solution and the formation of pores and cavities.

Biocompatibility studies

Seeding of cells on the obtained samples showed that the samples promoted the proliferation of osteoblasts and chondroblasts, maintaining a normal morphology.

Conclusions

A method for obtaining of 3D nanocomposite bioconstructions from water-protein dispersion of carbon nanotubes is described. The device for layer-by-layer laser prototyping was developed. The surface and internal structure of the created samples was characterized. The folded relief surface of the samples and the porous internal structure corresponds to the parameters of the natural extracellular matrix for supporting of cells. Bioconstructions demonstrated proliferation of cells (osteoblasts and chondroblasts). The osteochondral defects in the joints of laboratory animals were restored with the use of samples. Thus, the developed method can be used to restore defects of osteochondral joints with a various geometric shape.

References

- [1] S. M. Giannitelli. Current trends in the design of scaffolds for computer-aided tissue engineering. *Acta biomaterialia*, 10(2):580-594, 2014.
- [2] W. Y. Yeong, C. K. Chua, K. F. Leong, and M. Chandrasekaran. Rapid prototyping in tissue engineering: challenges and potential. *TRENDS in Biotechnology*, 22(12):643-652, 2004.
- [3] J. D. Pitts, P. J. Campagnola, G. A. Epling, and S. L. Goodman. Submicron multiphoton free-form fabrication of proteins and polymers: studies of reaction efficiencies and applications in sustained release. *Macromolecules*, 33(5):1514-1523, 2000.
- [4] A. Barrientos-Durán, E. M. Carpenter, N. I. Zur Nieden, T. I. Malinin, J. C. Rodríguez-Manzaneque, and L. P. Zanello. Carboxyl-modified single-wall carbon nanotubes improve bone tissue formation in vitro and repair in an in vivo rat model. *International journal of nanomedicine* 9:4277, 2014.
- [5] N. O. Chahine, N. M. Collette, C. B. Thomas, D. C. Genetos, and G. G. Loots. Nanocomposite scaffold for chondrocyte growth and cartilage tissue engineering: effects of carbon nanotube surface functionalization. *Tissue Engineering Part A*, 20(17-18):2305-2315, 2014.
- [6] A. Yu. Gerasimenko, O. E. Glukhova, G. V. Savostyanov, V. M. Podgaetsky. Laser structuring of carbon nanotubes in

the albumin matrix for the creation of composite biostructures. *Journal of Biomedical Optics*, 22(6):065003-1 - 065003-8, 2017.

Acknowledgements

This work was provided by the Ministry of Education and Science of the Russian Federation (Agreement 14.578.21.0221 RFMEFI57816X0221).

Analysis of physiological data to quantify stress and workload of surgeons with different levels of training during a laparoscopic cholecystectomy

N. Samm^{1,2}, D. Ostler¹, T. Vogel^{1,2}, N. Marahrens¹, D. Wilhelm^{1,2}, H. Feussner^{1,2}, R. Stauder³

¹Research Group MITI, Klinikum Rechts der Isar, Technical University Munich, Trogerstr. 26, 81675 Munich, Germany

²Department of Surgery, Klinikum Rechts der Isar, Technical University Munich, Ismaninger Str. 22, 81675 Munich Germany

³Computer Aided Medical Procedures (CAMP), Technical University Munich, Germany

Contact: nicole.samm@tum.de

Introduction

In a difficult and demanding environment such as the operating room, the individual effect of workload on surgeons is of particular importance. The increased stress and workload during an operation can lead to an impairment of technical skills and vigilance that causes an impact on memory and other cognitive processes. These facts can significantly influence our decisions and have an important effect on patient safety. (1)

Apart from the personal stress level of the surgeon, new technologies like robotic or robotic-assisted systems are increasingly finding the way into our operating theatres and will lead to an additional load of stress. Robots do not yet have the cognitive skills and experience of human assistants who can easily recognize, analyze and adapt to changing situations or even stress factors. For a safe human-robot interaction, and therefore a maximum of patients safety in intraoperative stress situations we must fulfill certain requirements. In order to reduce the arising workload of the human-machine interaction we should acquire knowledge of the surgical workflow. Critical situations during an operation should be identified and adapted by the robotic-assisted systems.

The first aim of this study was to examine the specific effects of intraoperative stress on the cardiovascular system at surgeons with different levels of training by measuring the respiratory rate (RR) and heart rate (HR). The second goal of our work was to examine a possible integration of our data into a workflow recognition system to recognize more complex and non-linear correlations by machine learning.

Materials and Methods

In a cross-sectional study during laparoscopic gallbladder resections (n=9) at the University Hospital Rechts der Isar, Munich, Germany the effect of intraoperative stress on autonomic balance, measured by the determination of heart rate (HR) and respiratory rate (RR) was studied.

The subject of the examination was a laparoscopic cholecystectomy performed by an experienced surgeon as well as an intern with less training on that operation. Difficult steps in this operation, that requires a high degree of concentration, are usually the preparation of the Calot triangle, the clipping of the vessels as well as the removal of the cystic duct.

The HRV was quantified by the analysis of the variation of beat-to-beat intervals in the electrocardiogram (ECG).

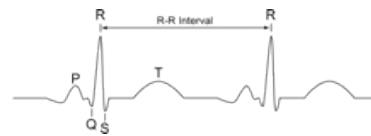


Figure 1: Standard figure of a QRS-Complex of the ECG. HRV can be calculated by the signal.

During the laparoscopic cholecystectomy we measured the respiratory rate, pulse and position of the upper body by using a specially designed chest belt with sensors that recorded the pulse rate and movement of the thorax during in- and expiration. Two experienced and three less experienced surgeons were enrolled as voluntary participants after given their written informed consent. Neither acute nor chronic illnesses within our test persons were present. Each participant was monitored over the course of a laparoscopic cholecystectomy. Data were analyzed with the statistical software SPSS Version 15.0 (SPSS, Inc., Chicago, IL, USA). Results are expressed as percent, median and total range.

Results

The median age of the participating surgeons was 39 years; the body mass index (calculated as weight in kilograms divided by height in meters squared) was in median 22.3 and all participants were in good physical conditions. The surgeons had 11.4 years of practice in middle and worked 49.2 h per week (**Table. 1**). No participant received any medication or had cardiovascular disease.

Characteristics	Median (range)
Age (years)	39 (28-62)
Height (m)	1.78 (1,73-1,85)
Weight (kg)	70.6 (58-84)
Physical activity rate	6.0 (3,0-9,0)
Years of experience (year)	11.4 (1-35)
Working hours per week (h)	49.2 (40-60)

Table 1: Characteristic of the study sample (n=5); Physical activity rate: evaluation on a scale from 0(no activity) to 10 (activity more than 8 h per week)

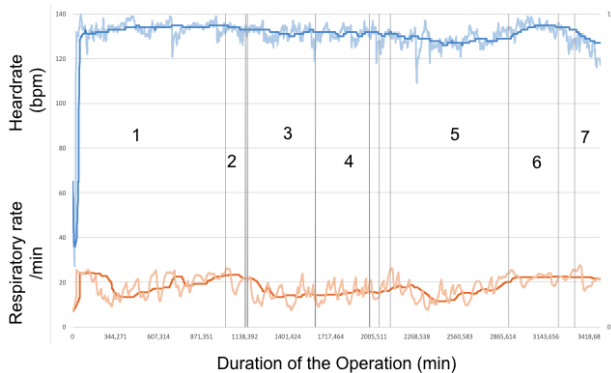


Figure 2: Median measure of the HR (dark blue line) and the respiratory rate RR (dark red line) of the experienced surgeons.

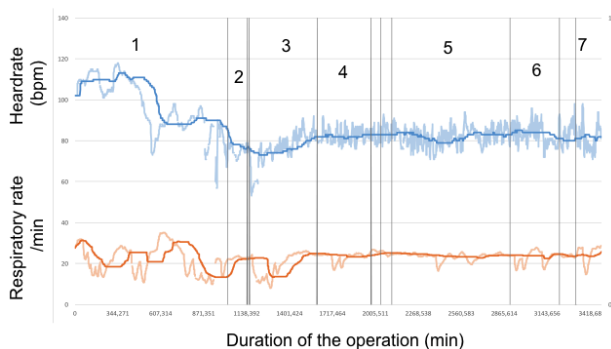


Figure 3: Median measure of the HR (dark blue line) and the respiratory rate RR (dark red line) of the non-experienced surgeons.

The two graphs above show the mean heart rate HR (dark blue line) and respiratory rate RR (dark red line) of the two experienced surgeons measured over the nine trials (**Figure 2**) and the three less experienced interns (**Figure 3**). To better display the variance in pulse and respiratory rate, the curves have been smoothed. The numbers in the graphs refer to the individual steps during the laparoscopic cholecystectomy. 1: prearrangement; 2: insertion of the individual trocars; 3: preparation of the Calot triangle; 4: clipping of the vessels and Ductus cysticus; 5: triggering the stacker; 6: gallbladder retrieval; 7: hemostasis.

The measured values of the experienced surgeons in Figure 2 show a slightly higher pulse but there is no great variance between the individual steps of the operation. Whereas the measurements on the interns with less experience (Figure 3) indicated that starting with a lower HR level, the different surgical steps produced a greater HR variance.

Discussion

In the present study we were able to show that there is an association of perceived stress at work and the cardiac autonomic control in surgeons. Regarding the outcome variables, the two groups of surgeons, divided according to their perceived stress levels, showed differences in the variation intraoperative HR and respiratory rate (RR).

Other research groups confirm to our findings that the analysis of the heart rate and the respiratory rate are very important marker of physical and mental stress as well as workload. (2,3) We postulate that the stress level, measured by HR and respiratory rate and the variation of both parameters, of a surgeon is reciprocally proportional to the level of education and training. Moreover, in general, young physicians are thought to experience more stress than veteran surgeons who are used to differ to different working conditions and follow their daily routine. (4) As we were able to show in our study, the experienced surgeons started with a bit higher HR level but the different steps of the operation with their different degrees of severity caused no big variance in HR or RR. In contrast, the less experienced surgeons showed a lower overall pulse level, but the individual surgical steps led to a greater variance in pulse (HR) and respiratory rate (RR). Therefore we claim that the analysis of the variance of HR shows a correlation on the occurrence of critical events during surgical procedure. However, this knowledge must be adapted to the surgeon's level of training. Moreover the integration of this data and knowledge into a workflow recognition system in order to recognize more complex, non-linear interrelationships by machine learning can lead to a safe human-robot interaction in intraoperative stress situations. This brings us closer to our goal of enabling robots or robotic-assisted systems to recognize problems and react to them independently.

There remain some potential biases of our study. Momentarily we have a small amount of participants in the study and just a few repetitions of the experiment. There are more different ways to gather and analyze physiological data of the participants. Beside the examined heart and respiratory rate, some groups postulate the use of biochemical indicators or eye tracking as well as EEG or EMG. Especially measuring the blink rate, the saccades, the pupil diameters and the duration of fixation with eye tracking seems to be another line leading approach. (5)

Conclusions

In our opinion the analysis of the workload of a surgeon and its effects are very important. According to the Yerkes Dodson law, performance increases with physical and mental stress, but only to a point. When the stress level become too high our performance decreases. But if we link our knowledge with technology in the future, we may be able to minimize the dangers arising from excessive workload and stress with the help of machines.



References

1. Arora S, Sevdalis N, Nestel D, Woloshynowych M, Darzi A, Kneebone R. The impact of stress on surgical performance: a systematic review of the literature. *Surgery* [Internet]. 2010 Mar;147(3):318–30, 330-6. Available from: <http://www.ncbi.nlm.nih.gov/pubmed/20004924>
2. Rieger A, Stoll R, Kreuzfeld S, Behrens K, Weippert M. Heart rate and heart rate variability as indirect markers of surgeons' intraoperative stress. *Int Arch Occup Environ Health* [Internet]. 2014 Feb;87(2):165–74. Available from: <http://www.ncbi.nlm.nih.gov/pubmed/23370764>
3. Weippert M, Behrens K, Rieger A, Stoll R, Kreuzfeld S. Heart rate variability and blood pressure during dynamic and static exercise at similar heart rate levels. *PLoS One* [Internet]. 2013;8(12):e83690. Available from: <http://www.ncbi.nlm.nih.gov/pubmed/24349546>
4. Böhm B, Rötting N, Schwenk W, Grebe S, Mansmann U. A prospective randomized trial on heart rate variability of the surgical team during laparoscopic and conventional sigmoid resection. *Arch Surg* [Internet]. 2011 Mar;136(3):305–10. Available from: <http://www.ncbi.nlm.nih.gov/pubmed/11231850>
5. Tokuda S, Obinata G, Palmer E, Chaparro A. Estimation of mental workload using saccadic eye movements in a free-viewing task. *Conf Proc. Annu Int Conf IEEE Eng Med Biol Soc IEEE Eng Med Biol Soc Annu Conf* [Internet]. 2011;2011:4523–9. Available from: <http://www.ncbi.nlm.nih.gov/pubmed/22255344>

Acknowledgements

This study was funded by DFG grant 1321.

New Geometric Method of Heart Rate Variability Estimation based on the Multiscale Correlation Analysis Representation

V.E. Antsiperov

Kotelnikov Institute of Radioengineering and Electronics of Russian Academy of Sciences,
Mokhovaya 11-7, Moscow, Russia
Contact: antsiperov@cplire.ru

Introduction

The nature and characteristics of ECG signals have been the subject of research for more than 100 years. This is because ECG signals contain a valuable diagnostic information about the functioning of the heart and, indirectly, about some other organs. Now, despite the impressive track record of the diagnostics and recommendations already developed [1], ECG signals continue to be the subject of intensive study both in the field of cardiology and biomedical engineering. Cardiologists search for new diagnostic properties of ECG signals, while engineers are interested in new approaches and methods for such signals processing and analysing. New methods imply, in particular, new techniques of noise suppression, efficient signal representation and feature extraction.

Feature extraction is an essential step in ECG processing. It consists in formation of some feature patterns – a set of descriptors most adequately describing the signal. Among these features / descriptors the most important are those with diagnostic properties. As a rule, they represent time domain parameters, though sometimes they can be defined in the frequency domain. Basing on ECG patterns, one can make some initial diagnosis [1]. For example, an “irregular” QRS complex without P wave is the hallmark of atrial fibrillation, the shape of the QRS with a left bundle branch block indicates a risk of cardiomyopathy, etc.

ECG patterns, especially P–QRS–T complexes, are also the basis for the subsequent heart rate analysis. Usually it is a more complex phase of ECG signal processing. However, now there are many methods and approaches related, for example, to the heart rate variability (HRV) analysis [2]. Quantitative evaluation of the HRV is usually based on the calculation of some indices connected with the variability of sequential NN intervals (normal-to-normal intervals between adjacent QRS complexes). Some of these indices are determined in the time domain – SDNN, CV, RMSSD, PNN50, etc. Others – in the frequency domain – VLF, LF, HF spectral power components, IC index, etc. It should be noted that, due to the complexity of the ECG signal, its fractal-like nature, the values of almost all indices can essentially diverge for different lengths of time intervals analysed, even for the same record. Therefore, the European Society of Cardiology suggests differentiating the diagnostic methodologies based on HRV indices obtained from the short-term recordings (of 2 to 5 min) and from the long-term recordings (of entire 24-h period) [3].

The above discussion is illustrated in Figure 1 by cardioin-

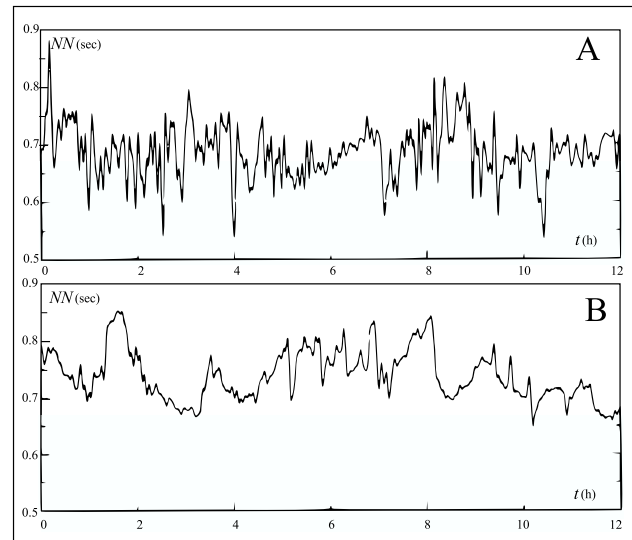


Figure 1: The interbeat interval NN after low-pass filtering for (A) a healthy subject and (B) a patient with severe cardiac disease (dilated cardiomyopathy). The healthy CIG shows more complex fluctuations compared to the more “smoother” diseased heart rate fluctuation pattern. Drawing is adapted from [4].

tervalograms (CIG, the NN interval dependences on time) for a healthy person (A) and a heart disease person (B). It is clear from the figure that both CIGs are qualitatively different. For example, at a small temporal scale, the variability (spread) of NN intervals in a healthy person is greater, which is a well known fact [5] – but on large scales the variability becomes equal in both cases. This observation suggests that the diagnosis based on HRV is adequate, but diagnostic procedures (automatic in particular) may be non-trivial. This circumstance gives high relevance to the development of new ECG processing methods based on long records – more than 10 minutes, for example, Holter.

Geometric Method of HRV Estimation

As it is mentioned above, variations in heart rate may be evaluated by a number of indices, which can be calculated by a number of methods. Perhaps the most popular and at the same time the simplest to perform are the so-called geometric methods [2], [3].

Geometric Methods

Geometrical methods include, as a rule, some geometric pattern formed by the sequence of NN intervals, such as the sample density distribution, sample density distribution of differences between adjacent intervals, Lorenz plot of NN or RR intervals, etc., and a simple formula, which judges the variability based on the geometric and/or graphic properties of the formed pattern. A number of popular geometric methods can be found in [3], [6].

The main advantage of geometric methods is their relative insensitivity to the accuracy of NN intervals measuring. The main drawback is the need for a large amount of NN intervals for constructing a geometric pattern. In practice, it takes at least 20 minutes (but preferably 24 hours) to ensure correct operation of geometric methods, that is, the measurements of not less than ~ 1500 NN intervals are necessary. In addition to the fact that this is hard routine work (which, however, with certain precautions can be assigned to a computer), it makes known geometric methods inappropriate to assess short-term changes in HRV.

MCA based Method

In order to avoid the limitations of classical geometric methods (but to inherit their attractive properties), we developed a new estimating HRV method based on the multiscale correlation analysis (MCA) representations [7]. The idea of this method springs in connection with the study of statistical characteristics of point processes and was first announced in [8].

Let's note from the beginning, that the main instrument of multiscale correlation analysis – the MCA representation (pattern) – is formed not on the basis of NN intervals, as in the classical methods, but on the basis of some special estimation of autocorrelation function (ACF) calculated directly by the ECG record. The basic definitions of MCA representations for analyzing the rhythm of the ECG in the general form can be found in [7].

Further, let's accept for ECG the special model $z(t')$ of a pulse process:

$$z(t') = \sum_{k=-\infty}^{\infty} A_k g(t' - t'_k) \quad (1)$$

where sequence $-\infty < \dots < t_0 < t < t_1 < \dots < \infty$ is the random time moments of pulse occurrences, specially numbered with respect to some fixed time t (the point of the current analysis), \dots, A_0, A_0, \dots are the random amplitudes of the pulses, which we assume to be a stationary sequence of independent random variables with mean \bar{A} , and $g(t')$ is a non-random waveform, like the P-QRS-T complex, the same for all pulses. The statistics of the sequence $\{t_k\}$ is given by some point process (PP), whose model is specified below.

Within the model (1) framework, the general definition of MCA representation [7] takes the following special form:

$$\widehat{R}(t, \tau) = \frac{1}{\tau} \sum_{k=-\infty}^0 \sum_{k'=1}^{\infty} A_k A_{k'} \int_{-\infty}^{\infty} |G(f)|^2 \times \exp\{2\pi i f \tau\} \exp\{2\pi i f (t_k - t_{k'})\} df \quad (2)$$

where τ is the scale parameter of MCA representation and $G(f)$ is the Fourier spectrum of $g(t')$. The equation (2) expresses the MCA representation in terms of random variables $\{t_k\}$, $\{A_k\}$ and thereby fully determines the $\widehat{R}(t, \tau)$ as a random value. However, even with the simplifications made (independence of the amplitudes and pulse intervals, stationarity, etc.), it is completely unrealistic to obtain a complete statistical description of $\widehat{R}(t, \tau)$ in the form, for example, of its probability distribution. Therefore, it is necessary to confine the description of MCA representation to some simple characteristics, namely, to mathematical expectation of MCA $\langle \widehat{R}(t, \tau) \rangle$, without taking into account possible random fluctuations around it. The corresponding formula for the mean MCA representation can be obtained by averaging (2) (over all random variables and under all assumptions made) and has the form announced in [8]:

$$\langle \widehat{R}(t, \tau) \rangle = \frac{\bar{A}^2}{\tau} \int_{-\infty}^{\infty} |G(f)|^2 \exp\{2\pi i f \tau\} \times \left(\sum_{k=-\infty}^0 \sum_{k'=1}^{\infty} \langle \exp\{2\pi i f (t_k - t_{k'})\} \rangle \right) df \quad (3)$$

Model Specification

As follows from (3), in order to obtain the final, suitable for analysis mean MCA representation, it is necessary to know the averages $\chi_{k'k}(f) = \langle \exp\{-2\pi i f s_{k'k}\} \rangle$, where $s_{k'k} = (t_{k'} - t_k)$ are the intervals between ECG pulses (P-QRS-T complexes) occurring in $t_{k'}$ and t_k . Let us note in this connection that $\chi_{k'k}(f)$ also represents the characteristic function of $s_{k'k}$, which, in turn, is the sum $s_{k'k} = s_k + \dots + s_{k-1}$, where $s_j = (t_{j+1} - t_j)$ are the intervals between consecutive time moments. So, recalling that the characteristic function of the sum of independent random variables is the product of the characteristic functions of the terms, we arrive at the idea of choosing the cyclic renewal process – point process with independent intervals [9] – as associated with (1) PP.

As the concept of cyclic renewal process does not have widespread usage let's give here its exact definition with reference to [9]. Namely, consider a stochastic process $y(t')$ that cycles in some time moments $0 = t_0 < \dots < t_j < \dots < \infty$ through states $0 \rightarrow 1 \rightarrow \dots \rightarrow K-1 \rightarrow 0 \rightarrow \dots$ in that order, again and again. The time intervals $s_j = (t_{j+1} - t_j)$ with which the process remains in the states j are called sojourn times of these states. If all these sojourn times are independent, distributed with their own probability densities $\rho_j(s)$, then $y(t')$ is called the cyclic renewal process. It is clear that the process obtained by decimating $y(t')$ in such a way that the result contains only the moments of the

state 0 arrivals, then the resulting process will be the usual renewal process.

If we re-index the process time moments $\{t_j\}$ with respect to the current analysis time moment t in the same way as in the definition (1), then, it can be shown, that when t unlim- itedly increases, any set of intervals $s_k, \dots, s_{k'-1}$ becomes stationary, it is a well-known fact in the theory of (usual) re- newal processes. Moreover, in this asymptotically station- ary case the probability distribution density of the intervals is greatly simplified and its explicit expression becomes the following:

$$\rho(s_k, \dots, s_{k'-1}) = \sum_{l=0}^{K-1} P_l \prod_{j=k}^{k'-1} \rho_{(l+j) \bmod(K)}(s_j)$$

$$k \leq 0 < k', \quad P_l = \bar{s}_l / \bar{S}, \quad \bar{S} = \bar{s}_0 + \dots + \bar{s}_{K-1} \quad (4)$$

where \bar{s}_l are the mean values of sojourn time intervals in the states l , i.e. mathematical expectations of $\rho_l(s)$. In this context \bar{S} is the duration of the mean overall cycle or the mean period of the cyclic renewal process considered.

It follows from (4) that stationary joint distribution of in- tervals $s_k, \dots, s_{k'-1}$ does not decompose into a product of individual interval distributions. So, formally, stationary cyclic process ceases to be a renewal process (except for the case $K = 1$). At the same time, since (4) can be considered as a formula of total probability for alterna- tives $l = 0, 1, \dots, K - 1$, conditional (provided that s_0 is dis- tributed in accordance with the distribution $\rho_l(s)$ of the l 'th alternative) distributions of intervals will continue to be represented by products. Thus, a process considered would be more correctly treated as a conditionally renewal cycli- cal process. Incidentally, we note that the probabilities of the alternatives P_l are determined by the relative sojourn times in the consequent states l .

Having a complete statistical description (4) of any set of intervals $s_k, \dots, s_{k'-1}$, it is possible, in the frames of the model accepted, to find all necessary for calculating (3) characteristic functions $\chi_{k'k}(f) = \langle \exp\{-2\pi i f s_{k'k}\} \rangle$:

$$\chi_{k'k}(f) = \langle \exp\{-2\pi i f \sum_{j=k}^{k'-1} s_j\} \rangle =$$

$$= \sum_{l=0}^{K-1} P_l \prod_{j=k}^{k'-1} \chi_{(l+j) \bmod(K)}(f) \quad (5)$$

where $\chi_j(f) = \langle \exp\{-2\pi i f s_j\} \rangle$ are the characteristic func- tions of sojourn time interval distributions in the states j – distribution densities $\rho_j(s)$.

For one important case, which is implied in the cardiac NN intervals modeling, expression (5) can be essentially simplified. This is the case of a narrow enough densities $\rho_j(s)$, where the narrowness is understood as the small $Q_j = \sigma_j / \bar{s}_j$ values – standard deviation to the mean value ratios. Since in this case $\chi_j(f) = \langle \exp\{-2\pi i f s_j\} \rangle$ are well approximated by Gaussian characteristic functions

$$\chi_j(f) \simeq \exp\{-2\pi i f s_j\} \exp\{-\frac{1}{2}(2\pi f \sigma_j)^2\},$$

then formula (5) can be approximated by the expression:

$$\chi_{k'k}(f) =$$

$$= \sum_{l=0}^{K-1} P_l \exp\{-2\pi i f \bar{S}_{l+k}^{l+k'-1}\} \exp\{-\frac{1}{2} (2\pi f \Sigma_{l+k}^{l+k'-1})^2\} \quad (6)$$

where:

$$\bar{S}_{l+k}^{l+k'-1} = \sum_{j=k}^{k'-1} \bar{s}_{(l+j) \bmod(K)}$$

$$\Sigma_{l+k}^{l+k'-1} = \sqrt{\sum_{j=k}^{k'-1} \sigma_{(l+j) \bmod(K)}^2} \quad (7)$$

Geometric Pattern of mean MCA representation

To obtain the main instrument of the geometric method based on MCA, it only remains for us to substitute ex- pression (6) in mean MCA representation (3), calculate the sums of internal series and take the corresponding integral. The series in (3) can be calculated exactly:

$$\sum_{k=-\infty}^0 \sum_{k'=1}^{\infty} \langle \exp\{2\pi i f (t_k - t_{k'})\} \rangle = \sum_{n=1}^{\infty} H_n(f) \quad (8)$$

where:

$$H_n(f) = \frac{1}{\bar{S}} \sum_{l=0}^{K-1} \bar{S}_l^{l+n-1} \times$$

$$\times \exp\{-2\pi i f \bar{S}_l^{l+n-1}\} \exp\{-\frac{1}{2} (2\pi f \Sigma_l^{l+n-1})^2\} \quad (9)$$

The integral in (3) can not be calculated exactly, since we do not know the exact form of the spectrum $|G(f)|^2$. Nev- ertheless, it can be found approximately if we take into account the characteristic properties of ECG signals, that are prototypes of model (1) process. As HRV manifests itself in a noticeable change of NN intervals duration, the width of the distributions $\rho_l(s)$ is greater than the duration of the characteristic fragments of P–QRS–T complex. But this implies that in the frequency domain, on the contrary, $H_n(f)$ is much narrower than the spectrum $|G(f)|^2$. There- fore, taking $|G(f)|^2$ from the integral (3) as the constant $|G(0)|^2$ and calculating the remaining Gaussian integrals, we finally obtain:

$$\langle \widehat{R}(t, \tau) \rangle = \frac{\bar{A}^2 |G(0)|^2}{\bar{S}} \sum_{n=1}^{\infty} \sum_{l=0}^{K-1} \frac{\exp\left\{-\frac{(\tau - \bar{S}_l^{l+n-1})^2}{2(\Sigma_l^{l+n-1})^2}\right\}}{\sqrt{2\pi} (\Sigma_l^{l+n-1})^2} \quad (10)$$

With regard to formula (10), let us make an almost obvious observation – although in the left-hand site of the MCA representation denotation there remains a formal depen- dence on t , it is absent on the right-hand side. This is a natural consequence of the assumption of model stationar- ity.

Illustrations

In order to illustrate the important characteristics of a synthesized instrument that can be used in ECG diagnostics, we calculated the mean MCA representation $\langle \widehat{R}(t, \tau) \rangle$ (10) for the model case in which the sojourn time intervals are given by a simple sinusoidal formula:

$$\bar{s}_l = \frac{\bar{S}}{K} (1 + \delta \sin(2\pi l/K)), \quad 0 \leq l < K \quad (11)$$

where the value \bar{S}/K determines the average level of all sojourn time intervals \bar{s}_l , and the dimensionless "modulation index" δ determines the degree of their variability. Figure 2 shows two graphs of $\langle \widehat{R}(t, \tau) \rangle$ (10) – one (A) for the considerable variability index $\delta = 0.3$ and the other (B) for its small value $\delta = 0.03$. It is not difficult to see that in the first case (A) the noticeable "beats" of the $\langle \widehat{R}(t, \tau) \rangle$ oscillations are clearly manifested, but in the second case (B) the dependence on τ of the mean representation envelope is practically monotonic. Thus, extracting the envelope of the mean representation and estimating its oscillations, one can detect the presence of rhythm variability, and even find the related to it parameters, for example, the process cycle.

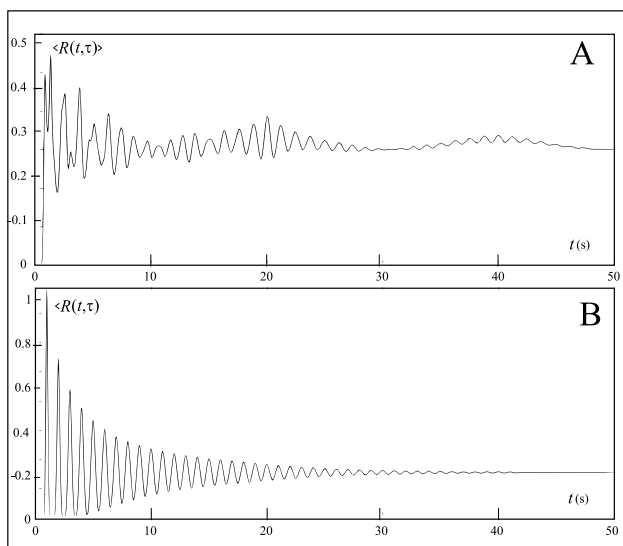


Figure 2: The graphics of mean MCA representation $\langle \widehat{R}(t, \tau) \rangle$ (10) with the same parameters $\bar{S}/K = 1$, $\bar{A}|G(0)|/\bar{S} = 1$, but different heart variability parameter δ (A) $\delta = 0.3$ and (B) $\delta = 0.03$.

To illustrate how the discussed features of the synthesized instrument manifest themselves in the processing of real data, Figure 3 shows two graphs of the $\langle \widehat{R}(t, \tau) \rangle$ (10) calculated and averaged over the ECG records from the Physionet portal databases NSRDB and SHAREE [10]. In both cases, with a time step $\Delta = 2$ sec a set of $N = 1000$ ACFs $\widehat{R}(t, \tau)$ (2) were calculated along each record and resulting representation $\langle \widehat{R}(t, \tau) \rangle$ was obtained as their arithmetic mean.

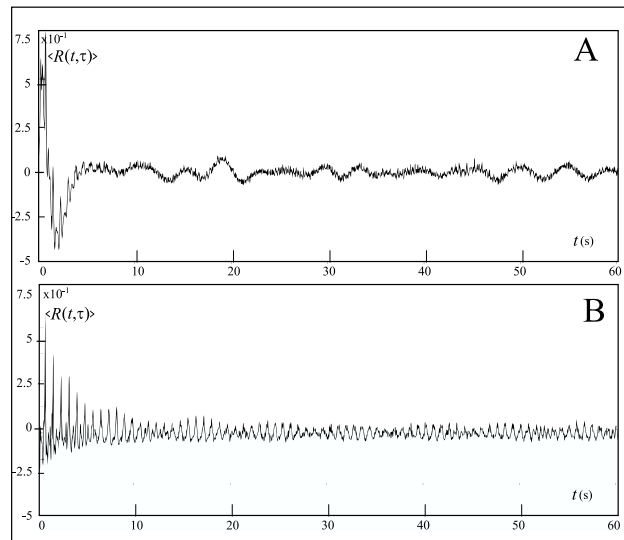


Figure 3: The graphics of mean MCA representation calculated and averaged over the real ECG records: (A) record of a healthy subject from NSRDB and (B) record of a patient with myocardial infarction from SHAREE [10].

The first graph (A) in Figure 3 is obtained from NSRDB ECG record and corresponds to the healthy person case. The second (B) is formed with the help of SHAREE data and shows the features of the disease person (myocardial infarction) representation. With the naked eye, we can see that the features of representations noted above for the model case also occur in the processing of real data. In particular, the shape of the envelope of representations allows us to accurately discriminate the case of a healthy patient from a patient with severe cardiac disease.

Conclusions

The synthesized instrument (10) showed very promising results on real records processed. Two types of ECG records from NSRDB and SHAREE databases [10] of a PhysioBank – the largest and growing archive of well-characterized digital recordings of physiologic signals were used. The proposed method made it possible to reliably discriminate the records from NSRDB, where no significant arrhythmias or any other HR disturbances were found from SHAREE records of hypertensive subjects at higher risk to develop vascular events.

Although there is still a lot of work to bring the method to the status of a useful and reliable tool for the analysis and diagnosis of heart disease, the first encouraging results suggest the optimistic prospects associated with it.

Acknowledgement

The author is grateful for the financial support of the work by Russian Science Foundation (grant 18-29-02108 mk).



References

- [1] J.S. Coviello. *ECG interpretation made incredibly easy!* Philadelphia: Wolters Kluwer, 3 edition, 2017.
- [2] R.M. Baevsky and A.G. Chernikova. Heart rate variability analysis: physiological foundations and main methods. *Cardiometry*, (10):66–76, 2017.
- [3] Task Force of the European Society of Cardiology, the North American Society of Pacing, and Electrophysiology. Heart rate variability. standards of measurement, physiological interpretation, and clinical use. *Eur Heart J*, 7(3):354–381, 1996.
- [4] A.L. Goldberger and H.E. Stanley et al. Long-range anticorrelations and non-gaussian behavior of the heartbeat. *Phys Rev Letters*, 70(9):1343–1346, 1996.
- [5] S.S. Yamamoto J.F. Thayer and J.F. Brosschot. The relationship of autonomic imbalance, heart rate variability and cardiovascular disease risk factors. *Phys Rev Letters*, 141(2):122–131, 2010.
- [6] M. Malik. Geometrical methods for heart rate variability assessment. In M. Malik and A. Camm, editors, *Heart Rate Variability*, pages 47–61. Armonk, Futura Publishing Company -New York, 1995.
- [7] V.E. Antsiperov and I.V. ZabrosaeV. New results for the pvc / spb detection using based on the mca heart rhythm estimation method. In *Proceedings of the 12th Russian-German Conference on Biomedical Engineering*, pages 182–186. Vladimir State University, jul 2016.
- [8] V.E. Antsiperov. Syclic renewal point processes for heart rate variability modeling. In *Extended abstracts of the second Russian Conference with international participation "Physics for Life Sciences"*, page 61. Ioffe Institute science-tech information department, sen 2017.
- [9] R. Serfozo. *Basics of Applied Stochastic Processes*. Springer, -Berlin, -Heidelberg, 2009.
- [10] L.A.N. Amaral A.L. Goldberger and et al. P.h. Ivanov. Physiobank, physiotoolkit, and physionet: Components of a new research resource for complex physiologic signals. *Circulation*, 101(23):e215–e220, 2000.

Tactile information analysis for forearm prosthesis feedback implementation

V.Y. Bukin¹, A.N. Briko¹

¹BMSTU, Baumanskaya 2-ya, 5, Moscow, Russia

Contact: vladislav_bukin@mail.ru

Introduction

To date, the problem of bionic hand prostheses control is connected with the complexity of using such devices with small and fragile objects. One of the important element for precise control of prostheses is the feedback, which is either absent in the such devices on the market or does not transmit information to the user.

The lack of feedback in prosthetic devices creates inconvenience, similar to tactile sensitivity violations [1]. With such disorders people have difficulties in many types of daily activities due to a lack of information about the mechanical states of contact during various objects manipulation [2].

In this paper, aspects are considered to solve the problem of missing tactile information replenishment in bioelectrical prosthesis using. Kinematical and mathematical models of the prosthesis for feedback input parameters calculation is presented. Also, the realization of the unit for effort registration, which is developed by the prosthesis.

The task of feedback implementation

Using the reception for feedback

Contact events between the fingers and objects provide sensorimotor control points for the motion phase controller. Behavioral studies show that this information is important for accuracy of motion commands controlling [2].

In addition, the perception of the object shape and relief is carried out by touch, in which the skin and motor analyzers participate [3]. On the basis of these features of touch as feedback parameters, it is necessary for the user to transmit precisely the amount of fingers pressure and their position.

Various kinds of stimulation are used for transmitting information to the patient and creating feedback: electro-tactile sensory stimulation, vibration-tactile sensory stimulation, and information transfer using acoustic signals perceived by hearing [4].

The most common practice is vibration-tactile stimulation, which is realized by pressure and vibration on the patient's skin. This type of feedback is compatible with a one-time electromyogram recording (in contrast to electro-tactile stimulation) and does not depend on the background sound.

Biophysical feedback model

To ensure the feedback system functioning it is necessary to consider the following patterns [5]:

$$S = a \cdot \log(I) + b \quad (3)$$

(3): S - the amount of sensation; I - intensity of stimulation; a and b - constants that are different for stimulus modalities.

According to this formula, the sensation increases in proportion to the logarithm of the stimulus intensity. For different sensory systems, this ratio is different. For skin mechanoreception is characteristic [5]:

$$\frac{\Delta I}{I} = m \quad (4)$$

(4): ΔI - the change in intensity of stimulation recognized by a person; m - the ratio of the change in the intensity of stimulation recognized by a person to the intensity of stimulation;

For the informative nature of the system, each of the following impacts should look like this:

$$I = I_0(m + 1) \quad (5)$$

(5): m - the ratio of the change in the intensity of stimulation recognized by a person to the intensity of stimulation; I_0 - initial intensity of stimulation.

It follows that the informative effects are multiples of m values of the minimum perceived value. Consequently:

$$I = I_{min}(m + 1)^n \quad (6)$$

(6): I_{min} - the minimum noticeable intensity of stimulation; n - the number of the difference threshold.

$$n = \log_{m+1} \frac{I}{I_{min}} \quad (7)$$

In fact, n is the number of distinguished exposure levels within the dynamic range. Providing the greatest value of n means distinguishing effort with the greatest accuracy within the dynamic range of impact. This result can be achieved by varying the area and amplitude of the effect on the skin.

The finger position registration and force detection unit has a minimum resolution, which is taken as the minimally different exposure threshold $I_{\min b}$. Then the number of the difference threshold n_b :

$$n_b = \log_{m_b+1} \frac{I_b}{I_{\min b}} \quad (8)$$

(8): n_b - the number of the difference threshold; I_{\min} - the minimum block resolution; I_b - the current value of the signal; m_b - the ratio of the change in the intensity of stimulation recognized by a person to the intensity of stimulation.

The numbers of the difference thresholds in the feedback signal recording unit and in the tactile stimulation unit must coincide:

$$n_b = n \quad (9)$$

From equations 7 and 8:

$$\log_{m+1} \frac{I}{I_{\min}} = \log_{m_b+1} \frac{I_b}{I_{\min b}} \quad (9)$$

Materials and methods

Measurement of the parameters of the opening width and the resulting effort for the feedback system in prosthetic tasks is preferably done indirectly by the signals from sensors inside the kinematic scheme. It is also preferable not to place pressure sensors directly on the tip of the finger, since the sensors themselves have a limited area, and points are located on the surface of the finger, the mechanical pressure of which will not be recorded by the sensor. For indirect force measurements at the tip of the finger, it is necessary to take into account the transfer functions of the mechanism parts. This will eliminate the misinterpretation of the received data, since the function may not be linear.



Figure 1: Prosthesis with an external power source manufactured by "Metallist"

The special stand was assembled to implement feedback in upper limb prostheses, thanks to which the test signals for feedback realization were recorded. In stand a functional-cosmetic prosthesis manufactured by "Metallist" was used (Fig. 1). The actuator is built into the mechanism of the

prosthesis and drives the prosthesis fingers and is movable relative to the body of the brush. One point of fixing the actuator is on the body of the brush, the second point is on the lever, which is the extension of the thumb. This fixing is used to save space inside the prosthesis and the weight of the product.

In the proposed prosthesis design, the position of the fingers is determined by counting the revolutions at the output of the prosthesis drive gear reducer using a digital monopolar Hall sensor. The measurement of the grasping motion developed by the prosthesis is carried out inside the kinematic chain (Figure 2), using a piezoelectric sensor built into the drive connection with moving parts of the prosthesis, and similarly recalculated at the fingertip through the transfer function.

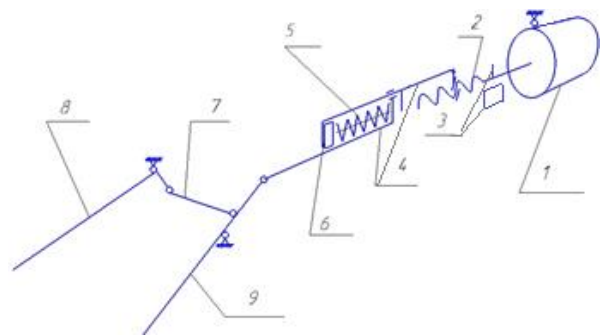


Figure 2: Kinematic scheme of the prosthesis: 1 - Prosthesis motor, 2 - Screw-nut transmission, 3 - Hall sensor and magnet on shaft, 4 - Sensor body, 5 - Spring, 6 - Silicon-sensitive resistor FSR400, 7 - Lever, 8 - II-V Fingers, 9 - I Finger

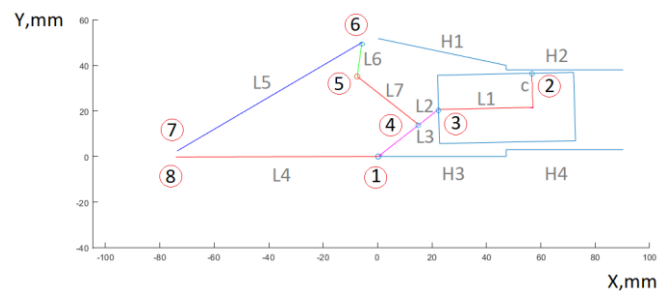


Figure 3: Mathematical model of prosthesis

For the proposed construction of the prosthesis in the Matlab a mathematical model of the kinematics of movement of the prosthesis mechanism details in the process of grasping-opening was created. In the model (Figure 3), the articulated connections are numbered with numbers, under the letter L the lengths of the arms are indicated, H - the dimensions of the prosthesis body for which the parts should not protrude, L5 and L4 - the prosthesis fingers, L1 - the current length of the actuator, c - the distance from the point hinged connection of the actuator with the body to the axis of the translational

motion of the actuator, L2, L6, L7 - the lever mechanism of the prosthesis which is transmitting the movement Δl_1 from the actuator of the prosthesis to the fingers. Points 1, 2, 6 - cylindrical joints of parts with the body of the prosthesis, points 3,4,5 - hinged cylindrical connections of the details of the linkage, and points 7 and 8 - the distance between the tips of the fingers. The blue rectangles indicate the dimensions of the actuator.

In the model, the distance between the fingertips (points 7 and 8), designated h , is calculated, which depends on the position of the actuator Δl_1 , and the force acting on the sensor F_d , also depending on the position of the actuator Δl_1 and the force at the tip finger F .

$$h = f_1(\Delta l_1)$$

$$F_d = f_2(F, \Delta l_1)$$

Both functions are nonlinear. It is noteworthy that the sensitivity of the sensor to the force at the tip of the finger F increases due to its conversion by the function f_2 . The results of the simulation are shown in Figure 4.

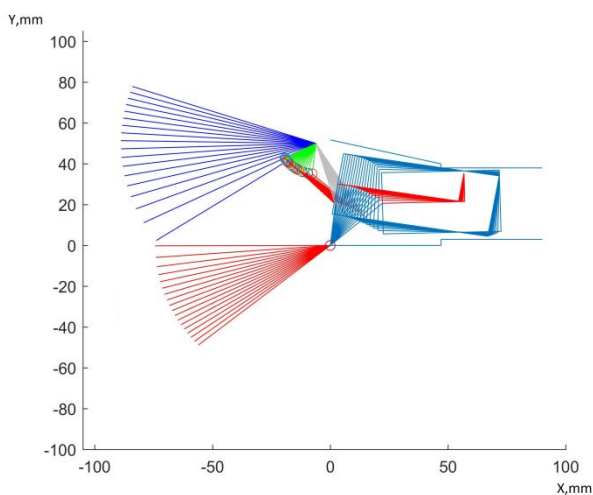


Figure 4: The motion of details of the prosthesis mechanism during the movement of the actuator with a step of 1 mm to the maximum extended

The design of transmission of traction from the drive to the fingers is spring-loaded - this is a necessary element of feedback. Upon contact with a solid surface, the force of interaction between the prosthesis fingers grows not spasmodically, but gradually, allowing the user to realize the touch and have time to react to it before the prosthesis develops maximum force.

To determine the position of the fingers, the speed at the output of the gear reducer of the prosthesis drive is calculated using a digital monopolar Hall sensor (Figure 5). To eliminate high-frequency noise after the Hall sensor, a passive low-pass filter was used.

Experimental part

Force signal at the end of the finger registration

As an example of a test signal, a signal was recorded in the process of chicken egg crushing by prosthesis. The chicken egg is fragile enough, so it is well suited to illustrate the operation of the feedback system. In the course of the experiment, the egg and prosthesis were placed on special supports.

The values of the voltage drop across the strain gage were calibrated using a set of laboratory weights of 20 g, 100 g, 200 g and 500 g, which made it possible to translate the values of the ADC readings into the values of the acting force. The data were recorded with a sampling frequency of 1000 Hz. To remove high-frequency noise, digital signal filtering was performed.

During the egg compression experiments, four series of measurements were made, resulting in a plot of the average strength of the egg shell destruction resistance with standard deviation (Figure 6). The signals recorded for each series of measurements were synchronized at the moment of breakage of the shell (at maximum force).

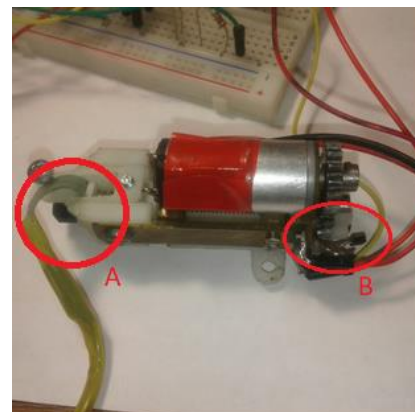


Figure 5: Location of the force-sensitive sensor (A) and the Hall sensor (B)

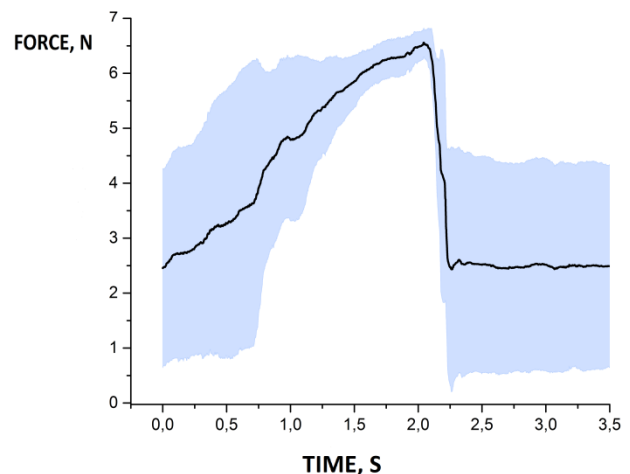


Figure 6: Average signal of chicken eggs breaking

Registration of the fingers opening width

The data were obtained using a Hall sensor that registered the speed of the output shaft of the actuator reducer when passing a magnet attached to the shaft next to the sensor. A passive filter was used to filter the Hall sensor signal. The obtained signal can be used by digital devices for calculating the speed and calculating the width of the prosthesis opening. In the current version of the model with a single Hall sensor, it was possible to achieve the accuracy of determining finger position of 5 mm.

Conclusions

In this paper, we considered aspects of the realization of unit of signal recording for tactile feedback system. We also proposed a location option for the sensors in the structure of prosthesis, which increases the area of the recording surface. A mathematical model for the correct interpretation of the information from the sensors is compiled. The main features of biophysical reception processes, that formulate requirements for the tactile stimulation unit, are considered, and the relationship of the output parameters of the tactile stimulation unit and the input parameters of the sensors of the tactile signal recording unit is described. The developed model of the prosthesis with the blocks of registration of the position of the fingers and of the effort allows for further experiments on the use of various tactile stimulation options.

References

- [1] Biomechanics and the Physiology of Motion / Bershtein NA edited by Zinchenko V.P. Moscow-Voronezh 1997, 43 p.
- [2] Roland S. Johansson, J. Randall Flanagan "Coding and use of tactile signals from the fingertips in object manipulation tasks" Nature on May 2009.
- [3] Gluhanyuk, N.S. General psychology: Course of lectures: / NS. Glukhanyuk S.L. Semenova, A.A. Pecherkina - Mn.: BSU, 2004. -290 p.
- [4] C. Antfolk, M. D'Alonzo, B. Rosén, G. Lundborg, F. Sebelius, C. Cipriani "Sensory feedback in the upper limb prosthetic" Taylor & Francis in Expert Reviews of Medical Devices on January, 2013
- [5] R. Schmidt and D. Dudel, Fundamentals of Sensory Physiology, Moscow, 1984, 287 p.
- [6] Fundamentals of Neuromechanics Francisco J. Valero-Cuevas. - Springer. -2015.- 204p.

Intraoperative Sterile Molding of Patient Specific Templates for Minimally Invasive Cochlear Implant Surgery

S. Müller, C. Janka, L. A. Kahrs, T. Ortmaier

Leibniz Universität Hannover, Institute of Mechatronic Systems, Appelstrasse 11a, Hannover, Germany
Contact: samuel.mueller@imes.uni-hannover.de

Introduction

Cochlear Implant (CI) surgery is an established treatment to restore severe hearing loss and deafness caused by inner ear dysfunction. To gain access to the cochlea for insertion of the implants electrode carrier mastoidectomy (partial removal of the cranial bone) is performed. This process is sophisticated and time consuming. Minimally invasive CI surgery has the potential to reduce operating time, trauma, hospitalization time, amount of needed anesthetics and costs and additionally improve ergonomics for the surgeon. The concept of this approach is to replace the mastoidectomy by a single drill hole from the surface of the skull to the cochlea. The complexity of this lies in the accuracy requirements resulting from the vicinity of the drill trajectory to the facial nerve. The drill (typical diameter 1.8 mm) has to pass through the approximately 2.5 mm wide facial recess in a depth of about 3 cm. Marker based navigation can not be effectively applied for this intervention. One method to achieve the required accuracy is by using a patient specific template to hold a linear guide for a drill.

The first clinical results of this approach are presented with the microtable system [1]. Beside the risk of physical damaging the facial nerve or thermal necrosis from heat induced by the drilling process [2] (both not further discussed in this paper) manufacturing of the template is still an issue. Operation planning is done in reference to the frame mounted on the patients skull at the beginning of the surgery. Since this reference can only be determined after fixation, the manufacturing of the template has to be done intraoperative. Manufacturing of the microtable is done none sterile by CNC machining a ULTEM (polyetherimide, PEI) block. In a shortened autoclaving process the finished template is sterilized and then cooled down. The shortened autoclaving of the microtable is neither certified in Europe nor in Russia. The RoboJig system (Figure 1), relying on the same working principle, was developed with a sterile manufacturing system to solve this problem. This paper is centered around the manufacturing unit of the RoboJig.

For sterile manufacturing of the jig different approaches have been developed. The technical requirements include, that the process can be done fast enough to avoid surgical downtime during anesthesia of the patient. This is the reason why 3D printing is currently not an option. Further it has to be guaranteed, that the chain of errors does not lead

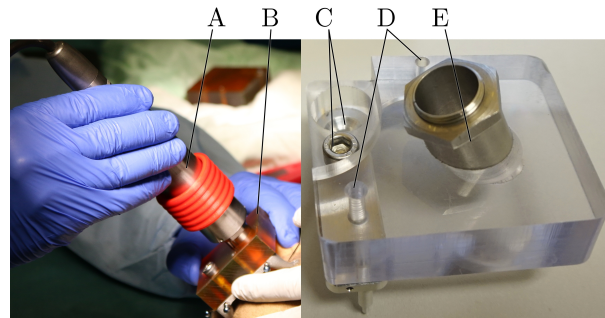


Figure 1: Left: linear guided surgical drill (A) connected to an intraoperativ milled jig (B) during initial cadaver experiment. Right: CNC milled jig prototype with connector holes (C-E).

to deviations larger than 0.5 mm in 30 mm depth during the drilling process. The jig should not hide the view of the situs for the surgeon.

template milling

In the current research setup the template is pre-formed and sterilized ahead of the surgery. The customization is done with a passive hexapod (Schick X1 med 3D, Schick-Dental GmbH, Germany) which positions the template relative to the axis of a drill unit on a linear guide. The struds of the hexapod are based on micrometer screws and adjusted manually. Their length is calculated based on the planned trajectory, which is transformed into the frame coordinates. The adapter on the hexapod platform uses a dowel pin connection dimensional similar to the one on the frame in Figure 1. Based on the planning data a stepped hole is drilled as interface for the surgical drill guide (Figure 1 part A and E). The forces generated during this customization process, as well as the angle of impact of the drill, raise the need for a stiff and highly accurate linear guide. Also a preformed and sterile template is needed for every surgery. Setup of the system and milling took 15 min in an initial cadaver trial. No deviation between drillhole and plan was visible in a postoperative CBCT scan (resolution 0.3 mm). The milling system of the RoboJig was described recently [3].

bone cement fixation

To reduce process forces and complexity an alternative manufacturing approach was developed. Its concept is to adjust a linear guide with the hexapod similar to the template milling approach. After orientation the guide is fixed to a mounting adapter using bone cement [4, 5]. This has

the advantage of low hardware costs and lower effort for certification.

polymer molding

In this paper a novel intraoperative manufacturing approach is presented. Our hypothesis is that a molding process results in lower process forces than in the template milling and therefor leads to a higher manufacturing accuracy and lower manufacturing time at lower costs. Injection molding is well established for processing thermoplastics. The melted material is extruded under high pressure into the mold. This typically leads to sterile parts depending on the environment [6]. For this process a mold has to be created for every new part. This is not feasible for the RoboJig since the part is different for every patient. An adjustable mold is not possible for injection molding because it has to be closed and leakproof. We experimentally investigated two low pressure process with an open mold. Pre sterilized granular material was used in combination with the inductively heated mold as well as a photopolymer cured under UV light.

Materials and Methods

The design of the jig is shown in Figure 1. It contains two holes for the dowel pin connection (Figure 1 part D) on the titanium frame of the system, two holes for the connection screws (Figure 1 part C) and one guiding hole for attaching a surgical drill unit (Figure 1 part A) through a locking ring (Figure 1 part E). Critical structures regarding accuracy, are the dowel pin connectors, the guiding hole and the lower surface of the jig attaching to the frame. The shown manufacturing concept is based on the adjustment of the guiding hole by a sterile hexapod. The endeffector of this hexapod is a 14 mm pin that is held in place in the fluid polymer during curing to create the guiding surface (not applied in initial tests). The shape of the jig is defined by the open mold shown in Figure 3.

material choice

In the current template milling approach ULTEM 1000 (PEI) is used as material. Its benefits lie in its high young's modulus and medical certification. Due to its high transition temperature it is not suitable for the molding approach. For an alternative material a low transition temperature is favorable to reduce risk and cooling time. Still the material should withstand the autoclaving process without losing form stability. A high melt flow rate (low viscosity) ensures that small structures in the mold get modeled. This is important for building the dowel pin connection. The chosen material should not inhibit medical certification of the system. Table 1 summarizes the properties of alternative materials. For an initial selection material probes were heated and cured in a miniature mold. The resulting probes are shown in Figure 2. From this initial experiment CALIBRE and TOPAS were chosen for further work because

of their material properties, melting behavior (little to no blistering) and transparency (enables view on the situs).



Figure 2: Materials after initial mold test in which the granulate was heated to its transition temperature

Table 1: comparison of material properties of suitable polymers from corresponding material data-sheets

	ULTEM 1000	CALIBRE 2081	LEXAN HP1REU
Material type	poly-etherimid	poly-carbonate	poly-carbonate
Young's modulus [MPa]	3500	2400	2400
Density [$\frac{kg}{m^3}$]	1270	1200	1200
Transition temperature [$^{\circ}C$]	195	142	126
Mold shrinkage [%]	0.5 - 0.7	-	0.7
Melt flow rate [$\frac{^{\circ}C}{kg}$]	9 [$\frac{337^{\circ}C}{6.6kg}$]	22 [$\frac{330^{\circ}C}{1.2kg}$]	35 [$\frac{300^{\circ}C}{1.2kg}$]
Melt volume flow rate [$\frac{^{\circ}C}{kg}$]	13 [$\frac{360^{\circ}C}{5kg}$]	-	33 [$\frac{300^{\circ}C}{1.2kg}$]
ISO 10993-1	yes	yes	yes

	Emerge 9500CR	VALOX HX312C	TOPAS 8007
Material type	poly-carbonate	polybutylene terephthalate	cycloolefin-copolymere
Young's modulus [MPa]	2270	2500	2600
Density [$\frac{kg}{m^3}$]	1290	1310	1020
Transition temperature [$^{\circ}C$]	109	54	75
Mold shrinkage [%]	-	1.6	0.1 - 0.5
Melt flow rate [$\frac{^{\circ}C}{kg}$]	10 [$\frac{260^{\circ}C}{5kg}$]	35 [$\frac{250^{\circ}C}{1.2kg}$]	-
Melt volume flow rate [$\frac{^{\circ}C}{kg}$]	-	31 [$\frac{250^{\circ}C}{1.2kg}$]	32 [$\frac{360^{\circ}C}{2.16kg}$]
ISO 10993-1	yes	yes	yes

mold design

Main task of the mold is providing an accurate negative volume for the jig. Figure 3 shows the design concept. The mold is build from three detachable parts for releasing the final jig. All structures relevant for the system accuracy (pins for the connection interface of the later part) are on a single part to avoid inaccuracy resulting from assembly.

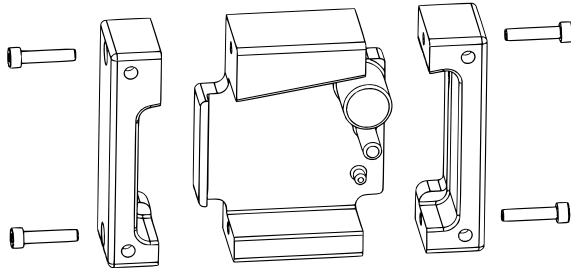


Figure 3: Design of the mold

system setup

The sterile hexapod uses magnetic ball joints to attach on a grid of base points on both connecting platforms. Since the micrometer screws allow for an adjustment in six degrees of freedom this coupling options leads to redundancy for most endeffector positions. This redundancy enables optimization regarding the systems accuracy. More information about the used hexapod can be found in [7, 8]. For a clinical implementation of either the granular melting or the photopolymer approach a lid has to be added to shield the system from its environment.

melt on and curing

To melt on the granular polymer it has to be heated to its transition temperature. The heating process should be fast and uniform while avoiding overheating and thus carbonisation of the melt. The system should be reasonably small to fit in the OR environment and pose a minimal risk to the clinicians. Inductive heating of the mold was chosen as compromise of those requirements.

experimental evaluation

To evaluate the feasibility of the manufacturing process two experiments were conducted. Aim was the production of an accurate jig comparable to a milled version. The pin for the guiding hole was not used in both initial experiments. In the first experiment the mold was filled with granular CALIBRE or TOPAS and then inductively heated until uniformly melted (Figure 5). After curing the jig was removed and measured with a coordinate measuring arm (FARO GAGE, Faro Technologies Inc., Lake Mary, FL, USA). Four specimen were produced for CALIBRE and ten from TOPAS (showed better initial results regarding accuracy). In a second experiment the medical photopolymer Med610 (Stratasys, Minnesota, USA) was used and cured

under UV light exposure. Typically this polymer is used for printing of patient specific templates for dental surgery.

Results

The described melt on process was successfully applied. Figure 4 shows two finished templates. The standard deviation of the measured distances of the dowel pin holes was 0,058 mm (n=10) for the TOPAS and 0,149 (n=4) for the CALIBRE specimen. The photopolymer approach was discarded due to blistering of the material (Figure 6C).

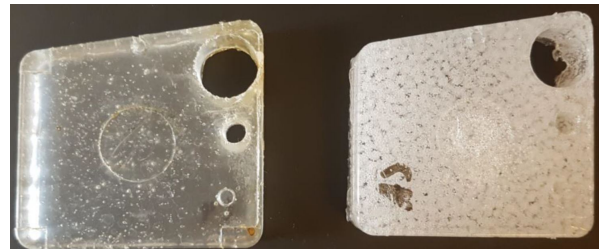


Figure 4: Cured jig made from TOPAS granulate (left) and CALIBRE granulate (right)

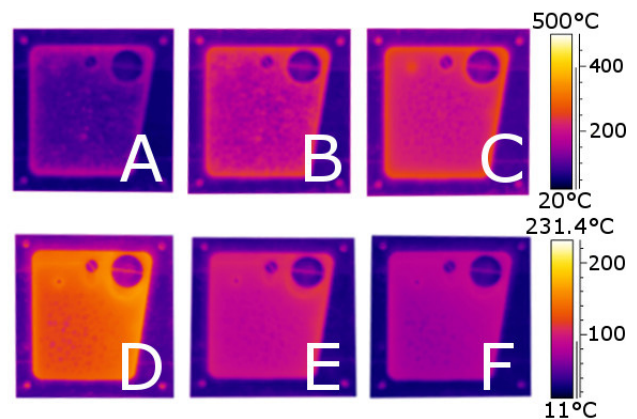


Figure 5: Exemplary heating and curing process taken from an infrared camera. A - C show the temperature distribution of the melt after 5 min, 25 min and 45 min respectively. D - F show the cooling process after 5 min, 15 min and 25 min. Please note the different color scale for A - C and D - F.

Discussion

The complete process currently takes 70 min plus the time for the system setup (5 - 10 min). Increasing the power output of the induction heater is not an option because it leads to carbonization of the edges of the jig while the inner parts are still granular (Figure 6A). The heating process can be started before surgery to avoid a bottleneck during the intervention. Curing can be speed up by emerging the mold in sterile water, however this has not been tested yet. An overview over the planned workflow is shown in Figure 7. The top surface of the jig might become uneven due to

shrinkage in the curing process (Figure 6B). This is not relevant for the system accuracy. Only the guiding holes (Figure 1 parts D and E) and the bottom surface (Figure 4) are relevant reference structures. UV curing did not meet the requirements. During the process gas development leads to hollow volumes. Blistering is avoidable by successively adding layers of < 1 mm thickness but this increases the process time and therefore eliminates its advantages over conventional 3D printing.

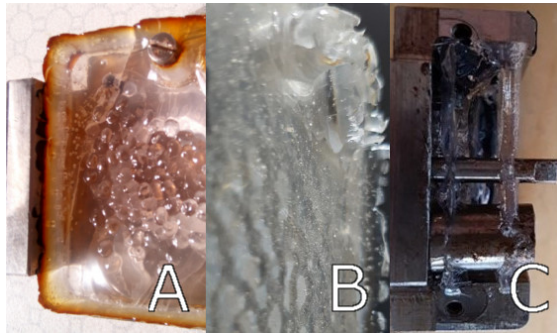


Figure 6: Three failure modes during molding. Uneven and fast heating (A), uneven surface from uneven heating and melt shrinkage during curing (B) and gas formation when UV curing thick layers of Med610 (C).

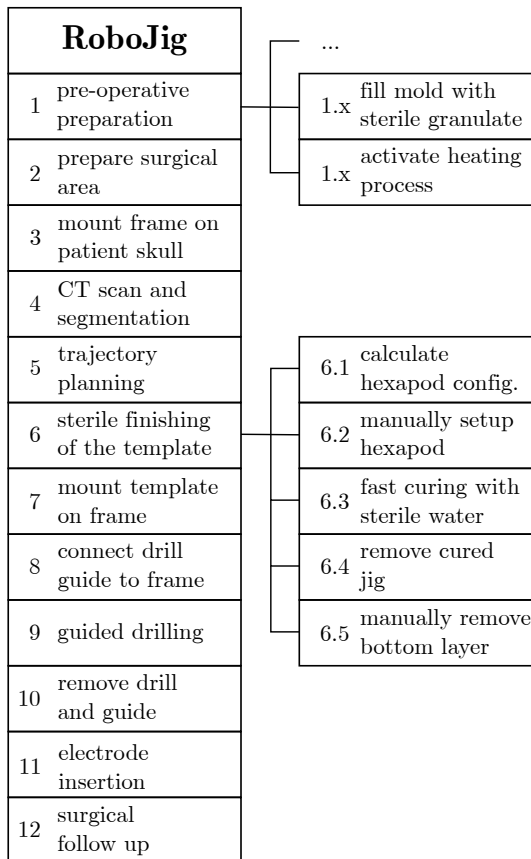


Figure 7: Proposed surgical workflow for the RoboJig system.

Conclusions

The concept of low pressure molding granular thermoplastics was successfully proven. Relevant structures were reproduced sufficiently accurate in the initial experiments. Still the surface quality can be improved by parameter optimization. For a clinical implementation further work is needed. Accuracy has to be evaluated in a next step by using multiple molded jigs to drill into artificial bone. Also the system needs to be optimized regarding usability, safety and process time. Currently the milling approach is beneficial due to shorter processing time. Implementing the workflow shown in Figure 7 could change this.

References

- [1] R. F. Labadie, R. Balachandran, J. H. Noble, G. S. Blachon, J. E. Mitchell, F.A. Reda, B. M. Dawant, and J. M. Fitzpatrick. Minimally invasive image-guided cochlear implantation surgery: First report of clinical implementation. *The Laryngoscope*, 124 (8):1915–19, 2014.
- [2] A. Feldmann, J. Anso, B. Bell, T. Williamson, K. Gavaghan, N. Gerber, H. Rohrbach, S. Weber, and P. Zysset. Temperature prediction model for bone drilling based on density distribution and in vivo experiments for minimally invasive robotic cochlear implantation. *Annals of Biomedical Engineering*, 44(5):1576–1586, 2016.
- [3] M. Kluge, G. J. Lexow, T. Lenarz, O. Majdani, and T. S. Rau. Untersuchungen zur Genauigkeit des intraoperativen Fertigungssystems für den RoboJig. *Tagungsband der 16. Jahrestagung der Deutschen Gesellschaft für Computer- und Roboterassistierte Chirurgie, CURAC 2017*, pages 262–265, 2017.
- [4] B. Vollmann, S. Müller, D. Kundrat, T. Ortmaier, and L. A. Kahrs. Methods for intraoperative, sterile pose-setting of patient-specific microstereotactic frames. *Proc. of SPIE*, 94150M:9415, 2015.
- [5] T. S. Rau, G. J. Lexow, D. Blume, M. Kluge, T. Lenarz, and O. Majdani. Micro-stereotactic frame utilizing bone cement for individual fabrication: an initial investigation of its accuracy. *Proc. SPIE*, 10135:101350, 2017.
- [6] M. Schönberger. *Autosterilität: Grundlagen und experimentelle Betrachtung der Kunststoff-Prozessechnik*. dissertation, Technische Universität München, 2014.
- [7] J. P. Kobler, J. Kotlarski G. J. Lexow, T. S. Rau, O. Majdani, and Tobias Ortmaier. Design optimization of a bone-attached, redundant and reconfigurable parallel kinematic device for skull surgery. *IEEE International Conference on Robotics and Automation (ICRA)*, page 2364–2371, 2014.
- [8] J. P. Kobler, K. Nülle, G. J. Lexow, T. S. Rau, O. Majdani, L. A. Kahrs, J. Kotlarski, and Tobias Ortmaier. Configuration optimization and experimental accuracy evaluation of a bone-attached, parallel robot for skull surgery. *Int J CARS*, 11(3):421–436, 2016.

Acknowledgments

The authors acknowledge the financial support by the Federal Ministry of Education and Research of Germany (BMBF project number 13GW0019C).